AD-A115 398 MISSION RESEARCH CORP SANTA BARBARA CA F/G 4/1
TECHNIQUES FOR REMOTE SENSING OF IONOSPHERIC ELECTRON DENSITY F--ETC(U)
AUG 81 J A BALL, G J FULKS, T E OLD F19628-80-C-0169
UNCLASSIFIED MRC-R-668 AFGL-TR-81-0331 NL

1 of 2
AD A
115398

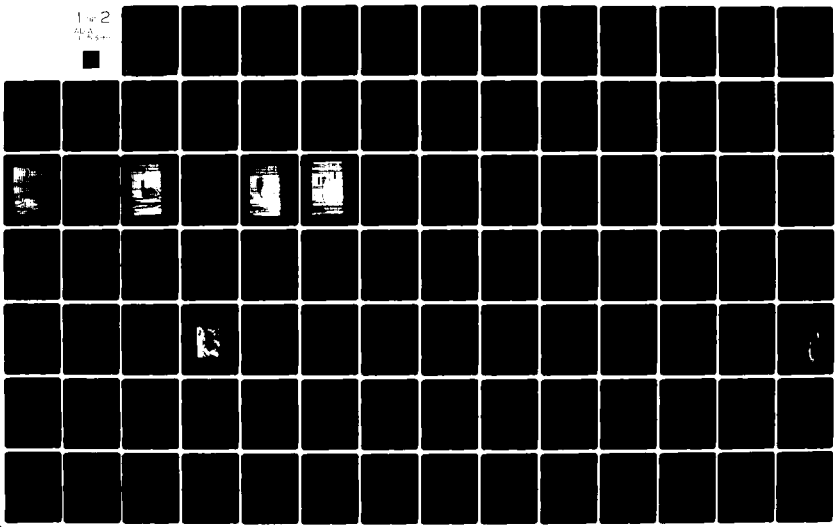

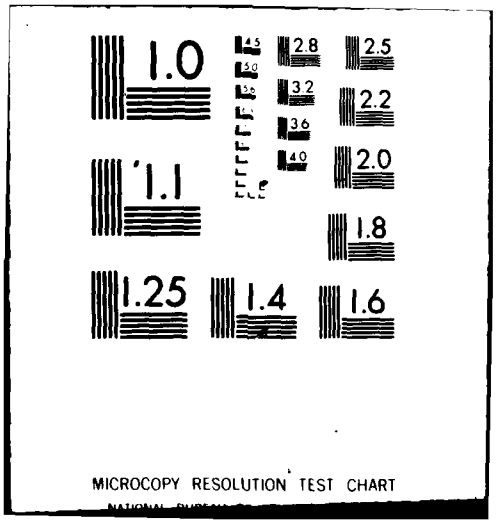
1.0
2.8
2.5
3.2
2.2
3.6
4.0
2.0
1.1
1.8
1.25
1.4
1.6
MICROCOPY RESOLUTION TEST CHART

AD A115398

(12)

AFGL-TR-81-0331

TECHNIQUES FOR REMOTE SENSING OF IONOSPHERIC ELECTRON DENSITY FROM A SPACECRAFT

Joseph A. Ball
Gordon J. Fulks
Thomas E. Old
William R. Wortman

Mission Research Corporation
735 State Street
P.O. Drawer 719
Santa Barbara, California 93102

Final Report
5 September 1980 through 5 August 1981

5 August 1981

Approved for public release; distribution unlimited

AIR FORCE GEOPHYSICS LABORATORY
AIR FORCE SYSTEMS COMMAND
UNITED STATES AIR FORCE
HANSCOM AFB, MASSACHUSETTS 01731

DTIC
ELECTE
JUN 1 0 1982
S D
A

DTIC FILE COPY

82 06 10 047

UNCLASSIFIED

SECURITY CLASSIFICATION OF THIS PAGE (When Data Entered)

REPORT DOCUMENTATION PAGE		READ INSTRUCTIONS BEFORE COMPLETING FORM
1. REPORT NUMBER AFGL-TR-81-0331	2. GOVT ACCESSION NO. AD-A115	3. RECIPIENT'S CATALOG NUMBER 398
4. TITLE (and Subtitle) TECHNIQUES FOR REMOTE SENSING OF IONOSPHERIC ELECTRON DENSITY FROM A SPACECRAFT		5. TYPE OF REPORT & PERIOD COVERED Final Report 5 Sep 80 - 5 Aug 81
		6. PERFORMING ORG. REPORT NUMBER MRC-R-668
7. AUTHOR(S) Joseph A. Ball Gordon J. Fulks Thomas E. Old William R. Wortman		8. CONTRACT OR GRANT NUMBER(S) F19628-80-C-0169
9. PERFORMING ORGANIZATION NAME AND ADDRESS MISSION RESEARCH CORPORATION 735 State Street, P.O. Drawer 719 Santa Barbara, California 93102		10. PROGRAM ELEMENT, PROJECT, TASK AREA & WORK UNIT NUMBERS 61102F 2310G6AA
11. CONTROLLING OFFICE NAME AND ADDRESS Air Force Geophysics Laboratory (PHI) Hanscom AFB, Massachusetts 01731 Monitor/Milton Klein/PHI		12. REPORT DATE 5 August 1981
		13. NUMBER OF PAGES 142
14. MONITORING AGENCY NAME & ADDRESS (if different from Controlling Office)		15. SECURITY CLASS (of this report) Unclassified
		15a. DECLASSIFICATION/DOWNGRADING SCHEDULE

16. DISTRIBUTION STATEMENT (of this Report)

Approved for public release; distribution unlimited.

17. DISTRIBUTION STATEMENT (of the abstract entered in Block 20, if different from Report)

18. SUPPLEMENTARY NOTES

19. KEY WORDS (Continue on reverse side if necessary and identify by block number)

Ionosphere	Topside Sounder	Chemiluminescence
Electron Density	Lidar	In Situ Measurements
Satellite Detector	Thomson Scatter Radar	Bremsstrahlung
Remote Sensing	Faraday Rotation	Hybrid Techniques

20. ABSTRACT (Continue on reverse side if necessary and identify by block number)

This paper examines a variety of techniques for the remote sensing of ionospheric electron density from a satellite platform. Most of the current satellite techniques are limited to determining ionospheric characteristics along the satellite track or directly beneath the satellite. This study considers techniques by which a more general areal survey can be made so that the electron density in three dimensions can be determined. Existing techniques are reexamined for additional potential, and the feasibility of new

DD FORM 1 JAN 73 1473 EDITION OF 1 NOV 65 IS OBSOLETE

UNCLASSIFIED

SECURITY CLASSIFICATION OF THIS PAGE (When Data Entered)

20. ABSTRACT (Continued)

techniques is considered.

Topside sounders currently offer the best areal survey capability with the ISIS satellites. A spacecraft version of the "Digisonde" sounder offers enhanced measurements.

Laser radars or lidars have substantial potential for ionospheric measurements but have not yet been developed for spacecraft use or for operation in the vacuum ultraviolet region of the spectrum where ionic species such as O^+ must be detected. It is anticipated that such developments are likely.

Thomson scatter radars are useful in ground-based installations but would be cumbersome on a satellite. They are huge and require high power to operate effectively.

Various Faraday and phase methods have been used over the years but yield only the column electron density and generally require a co-operating ground station. They are useful in conjuction with other measurements but probably not alone.

Numerous optical or chemiluminescent methods are possible. They often use relatively simple equipment and, hence, would be easy to include with other detectors on a satellite system.

In situ methods offer no possiblity of an areal survey but can be useful where detailed composition and high accuracy are important.

Bremsstrahlung is an indirect method potentially useful in the high latitude regions only. Be measuring the bremsstrahlung x-ray flux associated with a diffuse aurora it may be possible to determine the flux of precipitating electrons. This can, in turn, be related to the ionospheric electron density in regions where the precipitating flux provides the dominant ionization.

Because no single method offers a complete picture of the ionosphere, a hybrid method involving more than one technique is clearly preferable.

TABLE OF CONTENTS

Section		Page
	LIST OF ILLUSTRATIONS	2
	LIST OF TABLES	4
1	SUMMARY AND CONCLUSIONS	5
2	INTRODUCTION	11
3	TOPSIDE SOUNDERS	15
4	LASER RADARS (LIDARS)	39
5	THOMSON SCATTER RADARS	57
6	FARADAY AND PHASE METHODS	75
7	CHEMILUMINESCENT METHODS	89
8	IN SITU METHODS	115
9	BREMSSTRAHLUNG METHODS	117
	REFERENCES	136

Accession For
NTIS GRA&I ☑
DTIC TAB ☐
Unannounced ☐
Justification
By
Distribution/
Availability Codes
Avail and/or
Dist Special
A

DTIC COPY INSPECTED 3

LIST OF ILLUSTRATIONS

Figure		Page
1	Block diagram of Sounder System	22
2	ISIS II 1978 Day 210 1858:52 Z 0635 LT (24°N, 174°E, 1433 km high). Smooth daytime ionogram	25
3	ISIS II 1977 Day 236 0946:24 Z 2034 LT (21°N, 162°E, 1392 km high). Multiple echoes and some conjugate echoes	27
4	ISIS II 1977 Day 229 1058 Z 2106 LT (4°N, 152°E, 1415 km high). Exploded trace showing spread layer well above (and perhaps below) the smooth trace	29
5	ISIS II 1977 Day 228 1021 Z 2109 LT (6°N, 162°E, 1415 km high). Exploded trace and remote spread	30
6	Digisonde system diagram	36
7	Illustration of a lidar observing the ionosphere	40
8	Typical ion profiles for the midlatitude ionosphere at sunspot minimum during the day and night	43
9	Proposed lidar instrument for the Space Shuttle	52
10	A lidar instrument integrated into the Space Shuttle	52
11	Vertical and horizontal resolution tradeoffs (assuming a ±10% density measurement error) for the proposed NASA Mg^+ lidar experiment	54
12	Arecibo Ionospheric Observatory	58
13	Anticipated noise power versus frequency for a Thomson scatter radar in orbit and pointing either toward or away from the earth	64
14	Similar to Figure 13, except showing relative signal-to-noise ratio instead of noise power	65

Figure		Page
15	Power-aperture product required in a typical case	66
16	Hypothetical radar antenna unfurled from the Space Shuttle	68
17	Expected altitude change as a function of antenna diameter and time for an inital altitude of 270 km	69
18	Signal-to-noise ratio as a function of range and pulse width for the radar parameters shown	70
19	Anticipated signal return for a radar looking toward the earth	72
20	Major neutral species densities at F-region altitudes for exospheric temperatures of 800 and 700°K	92
21	Energy level diagram for atomic oxygen. Transitions which have been identified in the aurora or airglow are shown with thicker lines	95
22	Volume emission rates of several OI lines from dissociative recombination (DR), radiative recombination (RR), and ion-ion recombination (I-I) for typical F-region parameters given in Table 13	100
23	Atmospheric Explorer--E data	116
24	Simultaneous DMSP observations of bremsstrahlung x-rays, auroral arcs, and precipitating electrons	118
25	Kernel of bremsstrahlung production	121
26	Comparison of test electron flux, s(T) with electron flux s'(T) deduced by maximum entropy from two measurements of bremsstrahlung x-ray flux at 50 and 200 keV.	134

LIST OF TABLES

Table		Page
1	Summary of techniques for measuring ionospheric electron density from a spacecraft	6
2	Summary of ISIS II spacecraft characteristics	17
3	ISIS II topside sounder characteristics	20
4	Summary of other experiments on ISIS II	23
5	Digisonde measurement techniques	33
6	Programmable ionogram parameters	35
7	O^+ allowed transitions (partial list)	44
8	Cross sections at 83.3 nm	47
9	Attenuation coefficients	48
10	Partial list of lidar experiments that NASA considers feasible for the Space Shuttle	51
11	NASA specifications for a Nd:YAG-Dye laser system to be flown on the Space Shuttle to measure Mg^+ in the ionosphere	53
12	Ionic reactions important in nighttime F-region	93
13	Partial rate coefficients for $O^+(^4S^\circ)$ radiative recombination yielding emission in transition listed	96
14	Fraction of $O^+ + O^- \rightarrow O + O$ reactions which lead to emissions listed.	97
15	Sample nighttime species densities	98

SECTION 1
SUMMARY AND CONCLUSIONS

A variety of techniques for the remote sensing of ionospheric electron density from a satellite platform have been studied. Because most current satellite techniques are limited to determining ionospheric characteristics along the satellite track or directly beneath the satellite, this study considered techniques by which a more general areal survey can be made so that the electron density in three dimensions can be determined. Table 1 provides a concise summary of the results.

Topside sounders offer the best areal survey capability at the present time. Both of the ISIS spacecraft, launched into polar orbits over ten years ago, examine most of the topside of the earth's ionosphere twice each day. But they only observe during a small interval of local time and without the sophisticated sounding techniques now possible. Use of a spacecraft version of the "Digisonde" sounder on several polar orbiting satellites would considerably enhance topside sounding. This instrument is capable of extracting most of the information available in the radio wave reflected from the ionosphere. Phase measurements increase the group height resolution from 15 km for ISIS to 0.1 km for the Digisonde. Doppler measurements permit determination of the motion of individual ionospheric layers.

Laser radars (lidars) have considerable potential for ionospheric studies but have not been developed to the point where they could be deployed on a satellite in the immediate future. These instruments are not limited to viewing the subsatellite track beneath the spacecraft, and, hence, come the closest to providing true areal coverage. To be successful

Table 1. Summary of techniques for measuring ionospheric electron density from a spacecraft.

Method	Technique	Electron Density	Availability	Areal Survey Capability	Resolution	Comment
Active Sensing	1) Topside Sounding a) ISIS	V	C	F	G	Best Current Technique
	b) Digisonde	V	NF	G	VG	
	2) Laser Radar (Lidar)	V	FU	E	E	Best Future Technique
	3) Thomson Scatter Radar	V	FU	VG	F	Cumber-some
	4) Faraday and Phase Methods	CL (V)	C	F	VG	Needs Ground Station
Passive Sensing	5) Chemiluminescent Methods	CL (V)	C	E	VG	Many Possi-bilities
	6) In Situ Methods	V	C	P	E	
	7) Bremsstrahlung	V	NF	G	F	Indirect Method
	8) Hybrid Methods	V/CL	FU	E	E	Many Possi-bilities

Codes:
V = Volume
CL = Column
(V) = Some Volume Information
C = Current Technology
NF = Near Future
FU = Future

E = Excellent
VG = Very Good
G = Good
F = Fair
P = Poor

in measuring F-region electron density, lidars would have to detect O^+, because this is the dominant ionic species in the F-region. It would be necessary to use O^+ resonant or ground state transitions which occur in the vacuum ultraviolet. Because a tunable lidar does not yet exist in this region, space-borne lidars for the study of the F-region are hypothetical. However, a recent NASA study suggests that space-borne lidars operating near the VUV region are practical. If lidars operating in the VUV are developed with similar capabilities to those envisioned by NASA, then significant O^+ measurements can be made. With sufficient output power, lidars have an extremely good inherent range resolution of about 5 m, and horizontal resolution of about 60 m. Less output power or greater range gives less resolution. (The NASA instrument has a range resolution of 1 km and a horizontal resolution of 10 km in a typical case.) To observe other ionospheric layers would require a lidar capable of detecting such molecular ion species as O_2^+ and NO^+. This would probably require a second or third laser transmitter but would utilize the same telescope receiver.

Thomson scatter radars have substantial capabilities for observing the ionosphere from the ground but would be cumbersome in space. Because the modified Thomson scattering cross section is small, both a high power transmitter and a large antenna are required. While it is within current technology to achieve both the high power and large size on spacecraft such as the Space Shuttle, a space-borne Thomson scatter radar would still be limited by ground and auroral clutter problems and not have a particularly good resolution.

Faraday and phase methods have been used on spacecraft in various ways for two decades. These methods normally require a cooperating ground station or second satellite and thus lack flexibility. The methods generally yield the column electron density, although it is possible to extract the peak density of the F-region under some circumstances. Faraday and phase methods would be useful as part of a larger ionospheric observatory, but probably not as a stand-alone technique.

Many passive optical or chemiluminescent methods are possible with current technology and relatively simple sensors. For instance, a downward looking sensor sampling emissions at the 1356 Å and 6300 Å lines of atomic oxygen can be used to provide the height and electron density of the F-region peak. To convert the column emission rates that the sensor measures to electron density requires a knowledge of chemistry rate coefficients, neutral densities, and the shape of the electron density profile. A limb scanning method looking for the same emissions can provide the shape of the profile as well as the electron density along a strip several hundred kilometers wide centered on the orbital plane of the satellite. The limb scanning photometer measures the column emission rate but, by a series of overlapping measurements, it is possible to extract the volume emission rate from which the electron density can be calculated. Use of this technique in conjunction with a topside sounder reduces some of the uncertainty inherent in the calculations.

In situ methods will clearly provide the most detailed measurements of the ionosphere. However, by definition, they have little areal survey capability without a great many spacecraft. Therefore, such techniques have been essentially ignored here.

Bremsstrahlung is an indirect method for determining ionospheric electron density which is potentially useful in high-latitude regions only. By measuring the bremsstrahlung x-ray flux associated with a diffuse aurora, it may be possible to determine the flux of precipitating electrons. This flux can, in turn, be related to the ionospheric electron density in regions where the precipitating flux provides the dominant ionization. Because various spectra of precipitating electrons will produce the same bremsstrahlung, it is necessary to select a most probable spectra based on a given set of bremsstrahlung data. An approach based on a maximum entropy formalism seems the most tractable. The lack of a unique spectrum may not cause overly great difficulty as long as most of

the possible spectra produce nearly the same ionization. This work is still in progress.

Hybrid methods, incorporating two or more of the above techniques, would clearly be superior to any of the methods alone because of the complimentary nature of the various techniques. In several cases, one method, such as topside sounding, provides the calibrations necessary for another method, such as a scanning photometer looking for atomic oxygen. The scanning photometer then provides the electron density in the region adjacent to the subsatellite track, which cannot be seen by the sounder. Similarly, a laser radar would benefit from cross calibration with a topside sounder and would then be able to accurately survey a far larger area than could the sounder. The same argument applies to a topside sounder working with a Thomson scatter radar, a Faraday and phase technique, or a bremsstrahlung method.

A space-borne ionospheric observatory consisting of a topside sounder such as the Digisonde and a laser radar would have substantial capability for performing an areal survey, a capability far beyond any currently available. For little more effort, complexity, or cost, one could include a scanning photometer and bremsstrahlung x-ray detector. This would provide considerable redundancy enabling substantial cross calibration. Not only would such an instrument provide an excellent areal survey of ionospheric electron density over most of the globe day or night, but also additional information useful in ionospheric studies.

Specific recommendations for the future include:

1) Continued pursuit of laser radars.

2) Continued pursuit of bremsstrahlung techniques.

3) Design of a hybrid spacecraft.

SECTION 2
INTRODUCTION

Although the earth's ionosphere has been studied in many different ways for over fifty years, it is still pursued for scientific as well as operational reasons. The gross structure of the ionosphere is well understood, while the detailed structure and the evolution of the structure with time are only partially understood. In addition, the incoming electromagnetic and particulate radiations which influence and maintain the ionosphere are variable and incompletely known. As a consequence, predictions of ionospheric behavior for such applications as HF radio propagation are possible but subject to error. Hence, the ionosphere remains a subject of substantial interest.

This paper concentrates on techniques for directly or indirectly measuring ionospheric electron density from a satellite platform. Direct measurements of electron density are important to those concerned with radio propagation as well as to those building or verifying models. Indirect measurements of electron density such as measurements of incoming radiation can be used to calculate the electron density using large computer codes which incorporate the basic physics of the ionosphere.

Satellite measurements are emphasized by this study so that large or remote regions of the ionosphere can be observed. Because currently existing satellites can only measure electron density over a very limited region of the ionosphere during any given orbit, this investigation looks for methods by which a more general areal survey can be made. Satellite instruments have a large areal coverage but are necessarily limited by space, weight, power, and repair considerations to less

PRECEDING PAGE BLANK-NOT FILMED

elaborate or tempermental instruments. Most of the techniques discussed here involve self-contained satellite instruments but a few require a cooperating ground station.

Of the many ionospheric parameters which can be and have been measured, electron density is the most fundamental in scientific studies and the most important to those attempting to use the ionosphere for communications. Other ionospheric parameters such as positive and negative ion species and concentrations, neutral species and concentrations, and ion and electron temperatures are important but not of primary interest here.

Because it is difficult to measure all aspects of ionospheric electron density simultaneously, particular aspects of this density are emphasized at a given time depending on the particular application. For instance, electron density is pertinent to HF propagation, while integrated electron density (column electron density or total electron content) is useful to satellite communications. Similarly, small scale electron density structure is interesting in some contexts, while large scale structure is important in others. Sometimes, three dimensional spatial variation of electron density is wanted, while under other circumstances time development in one region is important. If one technique could be developed to measure all of these aspects at once, the problem would be solved. Unfortunately, no such technique exists or is likely to exist. Some techniques can measure more than one aspect of electron density but are not good for others. For instance, the ISIS satellites have the best existing capability for measuring ionospheric electron density. The topside sounders on these satellites measure electron density along the sub-satellite track. They obtain the electron density in two dimensions but not three. They see only the topside and not the bottomside. They measure the spatial variation of electron density in a north-south plane but not an east-west plane. They do not remain long enough in any region

to watch the time evolution of the electron density. Despite these shortcomings, the ISIS topside sounders have collected vast quantities of highly useful data. Some of the shortcomings of various instruments can be overcome by using two or more instruments with complimentary capabilities. Although a technique without shortcomings would be preferred, it is productive to consider any technique which may yield a different aspect of electron density.

This paper considers a broad range of techniques from those that have been tried and proven to those that are more speculative. Old techniques have been reexamined to look for additional potential, while several new techniques have been investigated to the point where their current potential can be evaluated. Active methods which probe the ionosphere with radio waves or light are discussed first, while passive methods which use emissions from the ionosphere are discussed last. Several of the active techniques directly yield electron density while most of the passive techniques yield the less useful column electron density.

Heading the list of satellite techniques is topside sounding, because this technique is the best one in current use for measuring electron density over wide areas. It is the technique against which others must be measured. Although topside sounding has been used for nearly twenty years, it has additional potential which is discussed. Two new techniques, laser radars and Thompson scatter radars, offer the possibility of improved area coverage and improved electron density measurements. Various Faraday and phase techniques are discussed. These have limited potential because they require a cooperating ground station or second satellite and still yield only column electron density. Many chemiluminescent methods are possible, some of which have considerable potential. In situ measurements have the virtue of high resolution but the drawback of very limited areal coverage. Ionospheric electron density in the polar regions is indirectly related to bremsstrahlung x-rays from precipitating

electrons. Measurements of this radiation can provide information on an important source of ionization in the polar ionosphere. To derive electron density from such measurements requires considerable calculation.

SECTION 3
TOPSIDE SOUNDERS

The satellite sensing technique currently offering by far the best areal survey of ionospheric electron density is topside sounding.[1] The two ISIS satellites[2] built by the Communications Research Centre in Ottawa, Ontario, Canada have topside sounders that have been operating in polar orbits for more than ten years. Although these instruments do an excellent job of sounding, advances in technology over the last decade now permit considerably more sophisticated measurements. An instrument called the "Digisonde"[3,4,5] built by the University of Lowell in Lowell, Massachusetts, incorporates the new technology and could rather easily be modified for spacecraft applications.

Topside sounding in its simplest form is analogous to the sonar technique used by ships to probe the ocean. The topside sounder broadcasts a short radio wave pulse at a frequency anywhere from about .1 MHz up to 10 or 20 MHz and listens for a return. The pulse reflects off of the ionosphere below the satellite when the pulse encounters an electron density with a plasma frequency equal to the radio wave frequency. This electron density is given by the well known relationship

$$N = 1.24 \times 10^4 f_p^2 \qquad (3\text{-}1)$$

where N is the electron density in electrons/cm^3 and f_p is the plasma frequency in MHz. By measuring the time it takes for the pulse to return to the satellite, the virtual distance from the satellite to a particular

electron density in the ionosphere can be found. If a succession of radio wave pulses are used starting near 0.1 MHz and proceeding in steps up to 10 or 20 MHz, the vertical profile of the topside ionosphere below the satellite can be obtained.

The satellite does not, however, see all of the ionosphere beneath it. The bottomside cannot be seen with this technique because pulses with a sufficiently high frequency to penetrate through the topside are not reflected by the lower electron densities existing below the peak of the F-layer. Hence, the bottomside F2, the F1, E, and D layers go undetected by this method. Also, the topside sounder normally receives the reflected echo from directly beneath the satellite even though the sounder transmitting antenna is essentially isotropic. This occurs because the smooth ionosphere reflects radio waves as a mirror reflects light. Because of the curvature of the earth and the corresponding curvature of the ionosphere, only the radio wave reflection occurring beneath the satellite returns a signal to the satellite. This means that topside sounders can, in general, only scan the topside ionosphere along the sub-satellite track. As the satellite moves in its orbit around the earth, it obtains an excellent two-dimensional view of the topside but misses three dimensional characteristics, misses the bottomside, and misses any variation with time. Time variations and three-dimensional characteristics can, to some extent, be pieced together using statistical studies of many passes.

The two ISIS spacecraft accomplish topside sounding and eight to ten other measurements of the ionospheric parameters. They are moderate size, moderate weight instruments, consume only 125 watts in full operation, and are highly reliable. After more than ten years of operation, most of the major spacecraft systems in both satellites are still functioning (including the sounders). Table 2 summarizes the characteristics of ISIS II. These characteristics are similar to those of ISIS I.

Table 2. Summary of ISIS II spacecraft characteristics (adapted from Reference 2).

SPACECRAFT SIZE

Shape	approximates an oblate spheroid
Height	1.19 m
Diameter	1.27 m
Weight	261 kg

ORBIT

Approximately 1400 km circular

Inclination 88.7° prograde

STABILIZATION

Spin stabilized

ALTITUDE SENSING

Six-probe flux-gate magnetometer

Digital solar aspect sensor

SPIN AND ATTITUDE CONTROL SYSTEM

Normal spin rate is near 3 rpm with a capability for changing the spin axis into either of two configurations

a. Spin axis in the orbit plane

b. Spin axis in cartwheel configuration

POWER SYSTEM

11,008 solar cells

3 nickel-cadmium batteries

5 main dc to dc converters

125 watts for 4 hours/day operation in 70 percent sunlight

2 consecutive pole-to-pole passes

Table 2 (continued). Summary of ISIS II spacecraft characteristics (adapted from Reference 2).

COMMAND SYSTEM

Multiple digital tone AM system

2 command receivers connected redundantly

216 command capability

TELEMETRY SYSTEM

Transmitter #1	
Frequency	136.080 MHz with 100 kHz bandwidth
Power	4 watts
Modulation	FM/PAM/PDM (housekeeping data)
	FM/PCM (Auroral photometer)
Transmitter #2	
Frequency	136.59 MHz with 50 kHz bandwidth
Power	2 watts
Modulation	PM/PCM (experiments and housekeeping)
Transmitter #3	
Frequency	401.75 MHz with 300 kHz bandwidth
Power	4 watts
Modulation	FM and PCM

The sounders on board these spacecraft can be operated in either a swept frequency or fixed frequency mode. They have a transmitter pulse power of 400 watts at a pulse repetition frequency of 45 pps and a pulse width of 100 μsec. This pulse width determines the inherent vertical resolution of 15 km. The inherent horizontal resolution is determined by the size of the first Fresnel zone of the reflecting surface beneath the satellite. This is typically 5 km but depends on the range of reflecting surface from the satellite and the sounding frequency. Irregularities with a smaller scale size than 5 km are observable under some special circumstances. One example is given below. The sounder transmitter feeds the sounder antennas via a passive network which provides cross-over coupling as a function of frequency between the long (73 m) and short (19 m) dipole antennas. The analog receiver uses the same antenna system and operates on one of several different broad bands. Table 3 summarizes the characteristics of the ISIS II sounder while Figure 1 provides a block diagram of the sounder system. For completeness, Table 4 is included to summarize the other ionospheric sensors on ISIS II. Again, ISIS I is very similar to ISIS II.

In reality, topside sounding is considerably more complex than it may seem. Figure 2 shows perhaps the simplest of the topside ionograms obtained by ISIS. This particular ionogram comes from ISIS II and was obtained in 1978 on Kwajalein Atoll.[6] It shows various sounder traces plotted as a function of sounding frequency and apparent range from the satellite. The apparent range has been computed from the measured time delay by multiplying by the speed of light and dividing by two. The width of the X and O traces show the 15 km inherent vertical resolution defined by the transmitted pulse width. Separate X, O, and Z traces occur because the ionosphere is imbedded in the earth's magnetic field. All of these traces can be explained by the Appleton-Hartree formalism.[7] The various resonance spikes occur because the satellite is within the ionosphere.

Table 3. ISIS II topside sounder characteristics (adapted from Reference 2).

SWEPT FREQUENCY SOUNDER

Power output	400 watts at PRF 45 pps
Pulse width	100 μsec
Antennas	Two crossed dipoles 73 m and 19 m at tip to tip

Frequency range

Normal sweep to 0.1 to 10 Mhz in 10 sec.

Extended sweep 0.1 to 20 MHz in 20 sec.

Frequency range	Sweep rate
0.1 to 2.0 MHz	0.375 MHz/sec.
2.0 to 5.0 MHz	1.125 MHz/sec.
5.0 to 20.0 MHz	1.5 MHz/sec.

Frequency markers

0.1, 0.25, 0.5, 0.75, 1.0, 1.25, 1.5, 1.75, 2.0, 3.0, 4.0, 5.0, 6.0, 7.0, 8.0, 9.0, 10.0, 12.0, 14.0, 16.0, 18.0, 20.0

Frequency resolution between markers is ± 8 kHz.

Range marker

11.11 msec after zero range mark (not on ISIS I)

Sounder receiver bands

(a) 0.1 - 1.0 MHz
(b) 1.0 - 2.0 MHz
(c) 2.0 - 3.0 MHz
(d) 3.0 - 5.0 Mhz
(e) 5.0 - 8.0 MHz
(f) 8.0 - 13.0 MHz
(g) 13.0 - 20.0 MHz

Table 3 (continued). ISIS II topside sounder characteristics (adapted from Reference 2).

FIXED FREQUENCY SOUNDER

6 fixed frequencies are available by command:

(0.12, 0.48, 1.0, 1.95, 4.0, and 9.303 MHz)

These occur either during the flyback period of the sounder sweep or for a full sounder frame period on alternate frames.

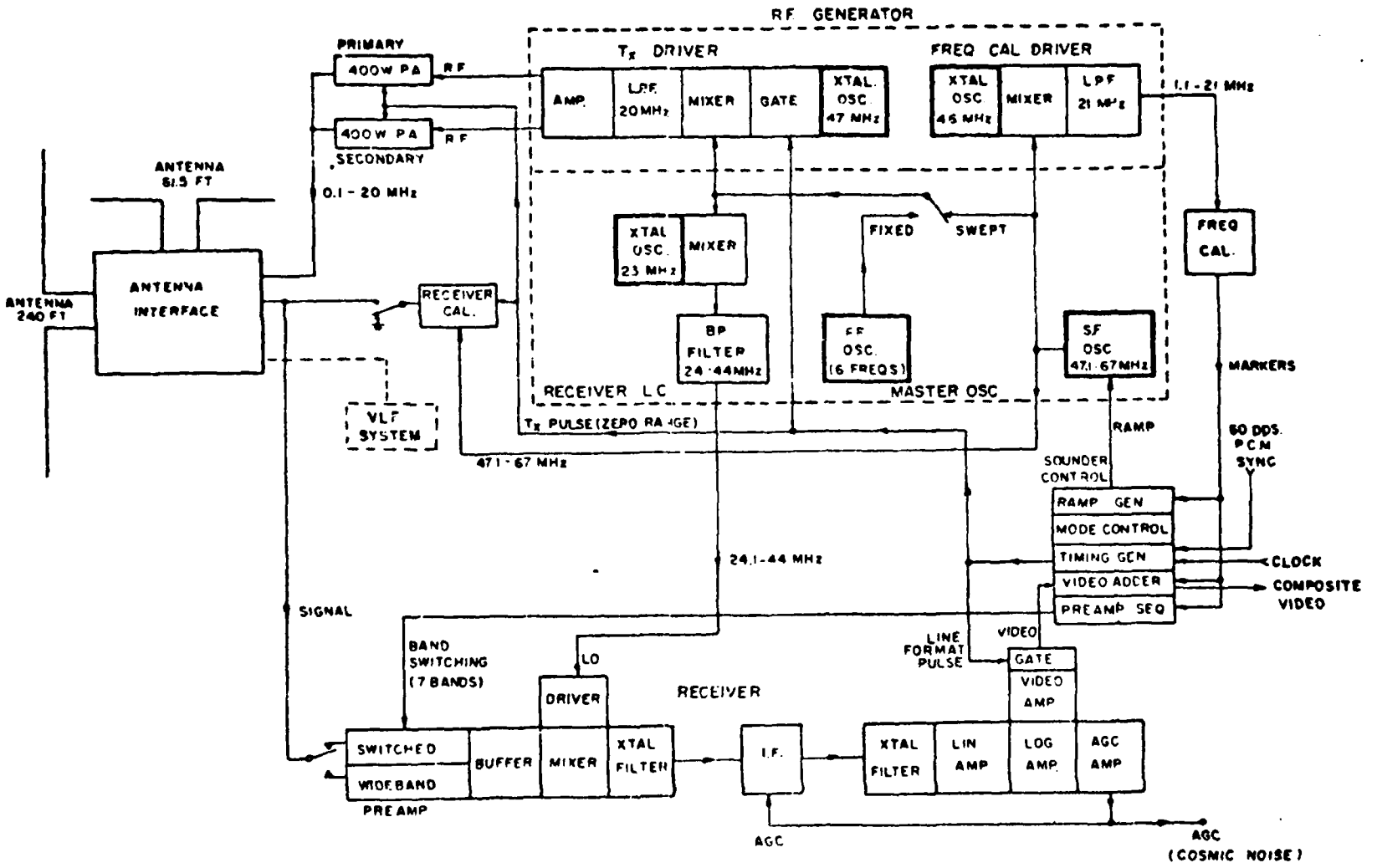

Figure 1. Block diagram of Sounder System (from Reference 2).

Table 4. Summary of other experiments on ISIS II (adapted from Reference 2).

VLF EXPERIMENT

Receiver for radio noise studies (.05 to 30 Khz)

Optical onboard receiver for ion resonance studies

ENERGETIC PARTICLE DETECTORS

Detectors to measure electron and proton intensity, angular distributions, and energy spectra

SOFT PARTICLE SPECTROMETER

Electrostatic analyzer to measure directional intensity and energy spectra of protons and electrons from 10 eV to 10 keV

ION MASS SPECTROMETER

Magnetic spectrometer to measure positive ion mass (1-64 amu)

LANGMUIR PROBE

Two cylindrical electrostatic probes at opposite ends of the spacecraft to mesure electron density and temperature

RETARDING POTENTIAL ANALYZER

Direct measurement of electron temperature, ion temperature, ion composition, and charged particle density

BEACON

Two 100 mW beacons to investigate ionospheric irregularities (136.410 and 137.950 MHz)

Table 4 (continued). Summary of other experiments on ISIS II (adapted from Reference 2).

COSMIC NOISE

Monitors background radio noise levels due to galactic, solar, and ionospheric sources using AGC of sounder receiver (0.1 to 16 MHz)

ATOMIC OXYGEN RED LINE PHOTOMETER (NOT ON ISIS I)

Maps global distribution in the intensity of the 6300 Å emission from atomic energy

AURORAL SCANNER (NOT ON ISIS I)

Maps the distribution of auroral emissions at 5577 and 3914 Å on the dark side of the earth

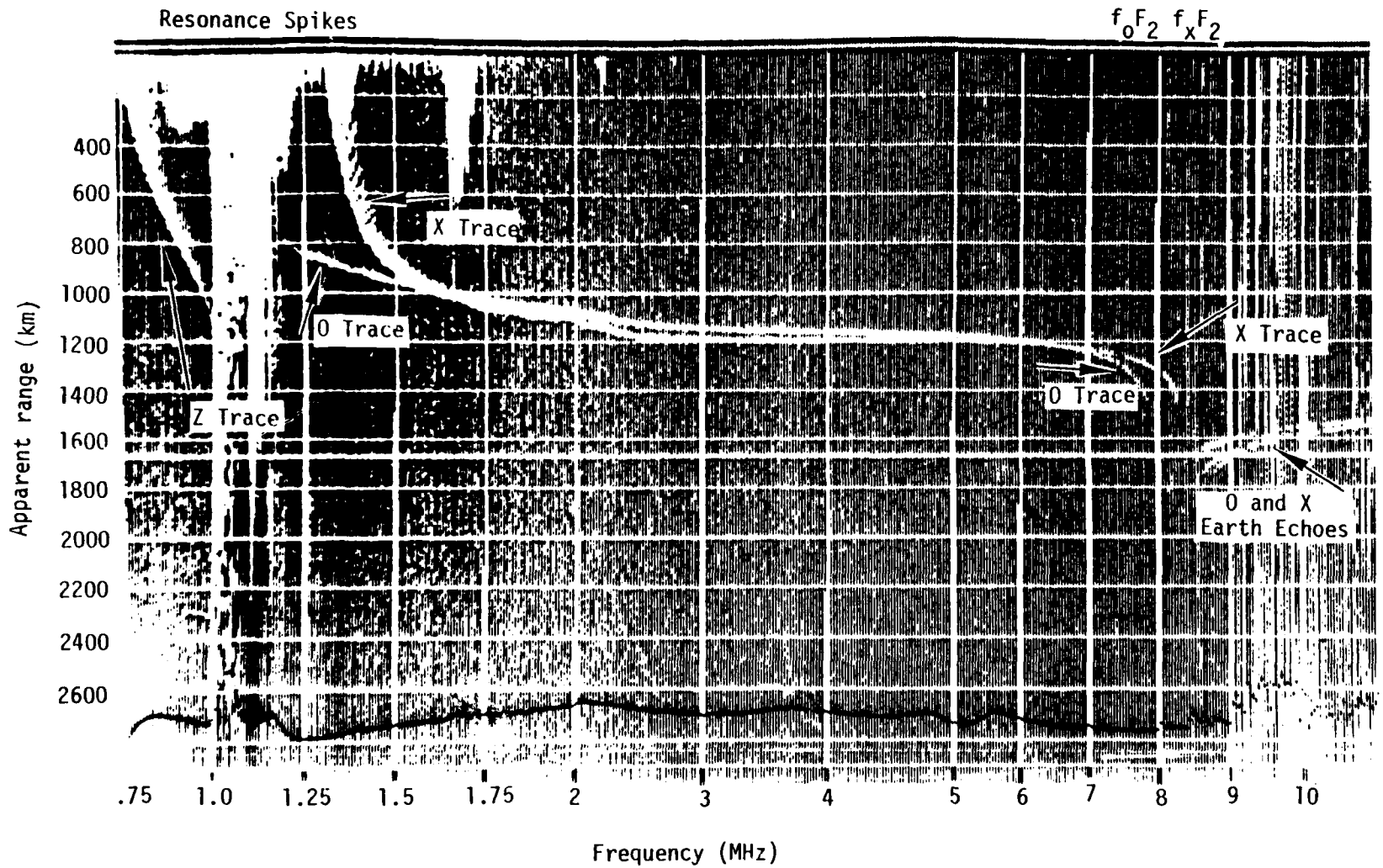

Figure 2. ISIS II 1978 Day 210 1858:52 Z 0635 LT (24°N, 174°E, 1433 km high). Smooth daytime ionogram[6].

Even though some of the resonance spikes extend to a large apparent range, they only represent resonances occurring in the immediate vicinity of the satellite. Similarly, the apparent ranges of the X, O, and Z traces are not equal to their real ranges, although the traces do represent reflections from below the satellite. For these traces, the apparent range is always greater than the real range because the sounder pulse always sustains some retardation in phase velocity just before reflection. Such retardation is well understood, so that topside ionograms can be rather easily reduced to true height profiles.[8]

Not all, or even most, ionograms are as simple or as readily understood as the one in Figure 2. For instance, Figure 3 shows an ionogram with a succession of traces at progressively greater ranges. In keeping with their appearance, they are labeled "Multiple Echoes." The strong multiple echo at greatest range is called a "Conjugate Echo" for reasons explained below. The departure of Figure 3 from the simple form of Figure 1 occurs because the ionosphere is not smooth. Returns in Figure 2 are coming from both the sub-satellite track as well as from other locations relatively far removed from directly beneath the satellite. In this case, the satellite has a far reaching view. It turns out that these multiple echoes are ducted echoes.[9,10] They are evidence that magnetic field aligned tubes of slightly depleted electron density, perhaps 1 km in diameter, exist below the satellite and extend for hundreds or thousands of kilometers along the field. They differ from the surrounding electron density by a few percent and have widths of a few kilometers. The conjugate echo is a special ducted echo where the satellite is actually inside the duct. Radio waves trapped within this duct can echo back and forth from one magnetic conjugate region to the other many times giving a strong return each time they pass the satellite.

The ionogram shown in Figure 4 illustrates another basic type of disturbed ionosphere seen by ISIS. This is one version of the classic

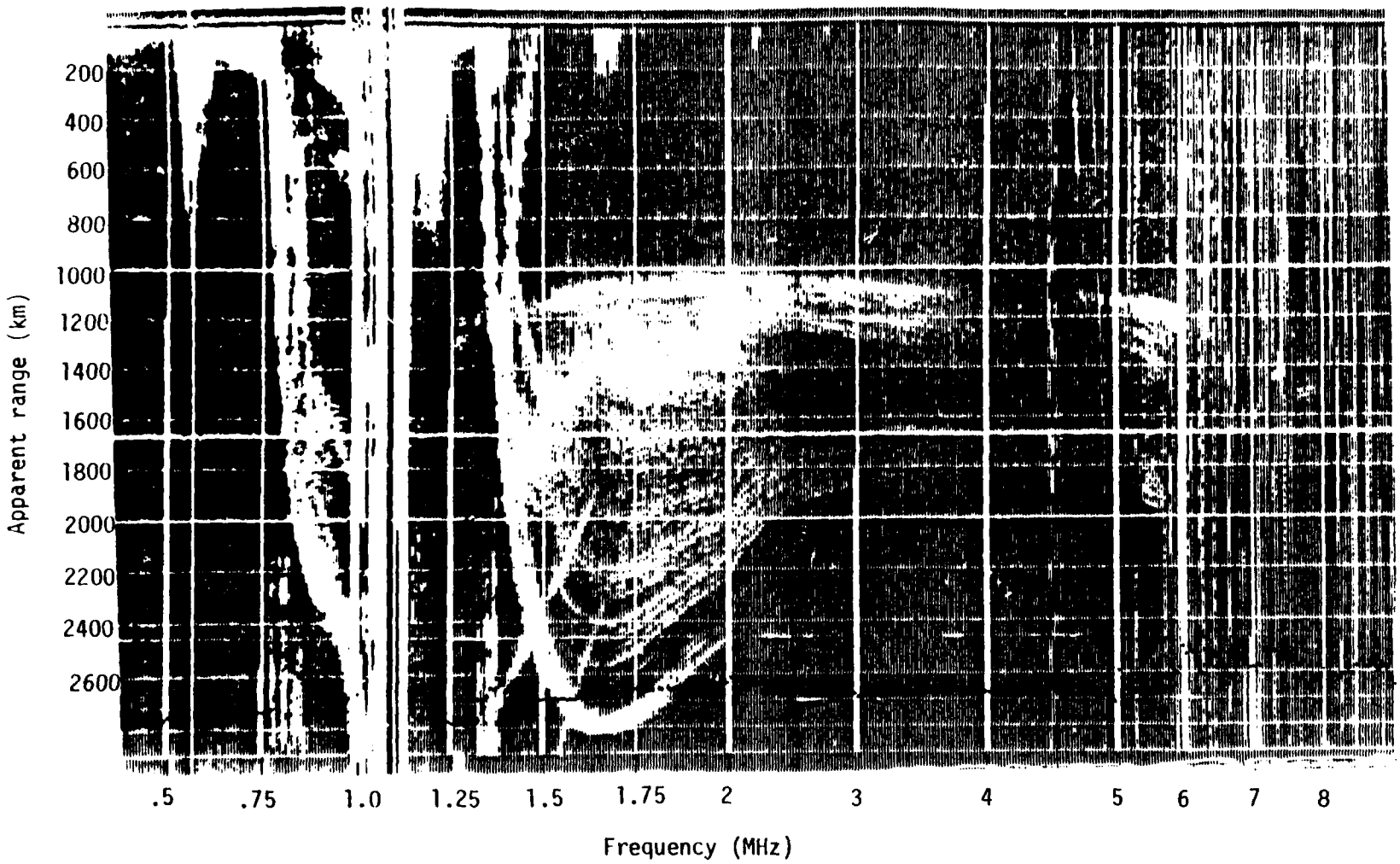

Figure 3. ISIS II 1977 Day 236 0946:24 Z 2034 LT (21°N, 162°E, 1392 km high). Multiple echoes and some conjugate echoes[6].

"spread-F" often seen on ionograms. It is evidence of a great deal of small scale structure below the satellite. Spread-F comes in several forms. This particular one, known as an "exploded trace," occurs only in the equatorial ionosphere and, in fact, only within the equatorial anomaly region from 15°N to 15°S magnetic latitude. Recently, such traces have been correlated with radar backscatter plumes and severe satellite signal scintillations.[6] They are probably caused by the equatorial bubbles under intensive investigation for the last few years.[11]

As with many complex topside ionograms, some controversy exists as to whether the spread returns in Figure 4 represent overdense or underdense reflections. Reference 12 views exploded traces as an overdense layer of irregularities above the otherwise smooth ionosphere. This layer has a limited east-west but long north-south extent. The irregularities supposedly produce overdense reflections but are sufficiently sparse that some of the sounder signal can penetrate to the ionosphere below. In contrast, Reference 13 views the irregularities as underdense, producing partial radio wave reflections because their cross sections are small compared to the wavelengths of the sounder radio waves. The irregularities then need not differ greatly in density from the surrounding plasma. They can be either slight enhancements or depletions. For various reasons, underdense reflection appears the more logical choice.[6]

Although topside ionograms normally provide only a two-dimensional view of the topside ionosphere, sometimes a three-dimensional view is obtained. Figure 5 shows two exploded traces. One trace is attached to the smooth primary trace and thus represents a plume beneath the satellite while the other represents a separate plume displaced to the east or west of the satellite. From successive ionograms, it is clear that these plumes are indeed separated east-west and have a very long north-south extent. Aspect sensitive underdense reflection of the radio waves from the irregularities permits the east-west extent of the irregularities to be seen in a given ionogram while suppressing the north-south extent.

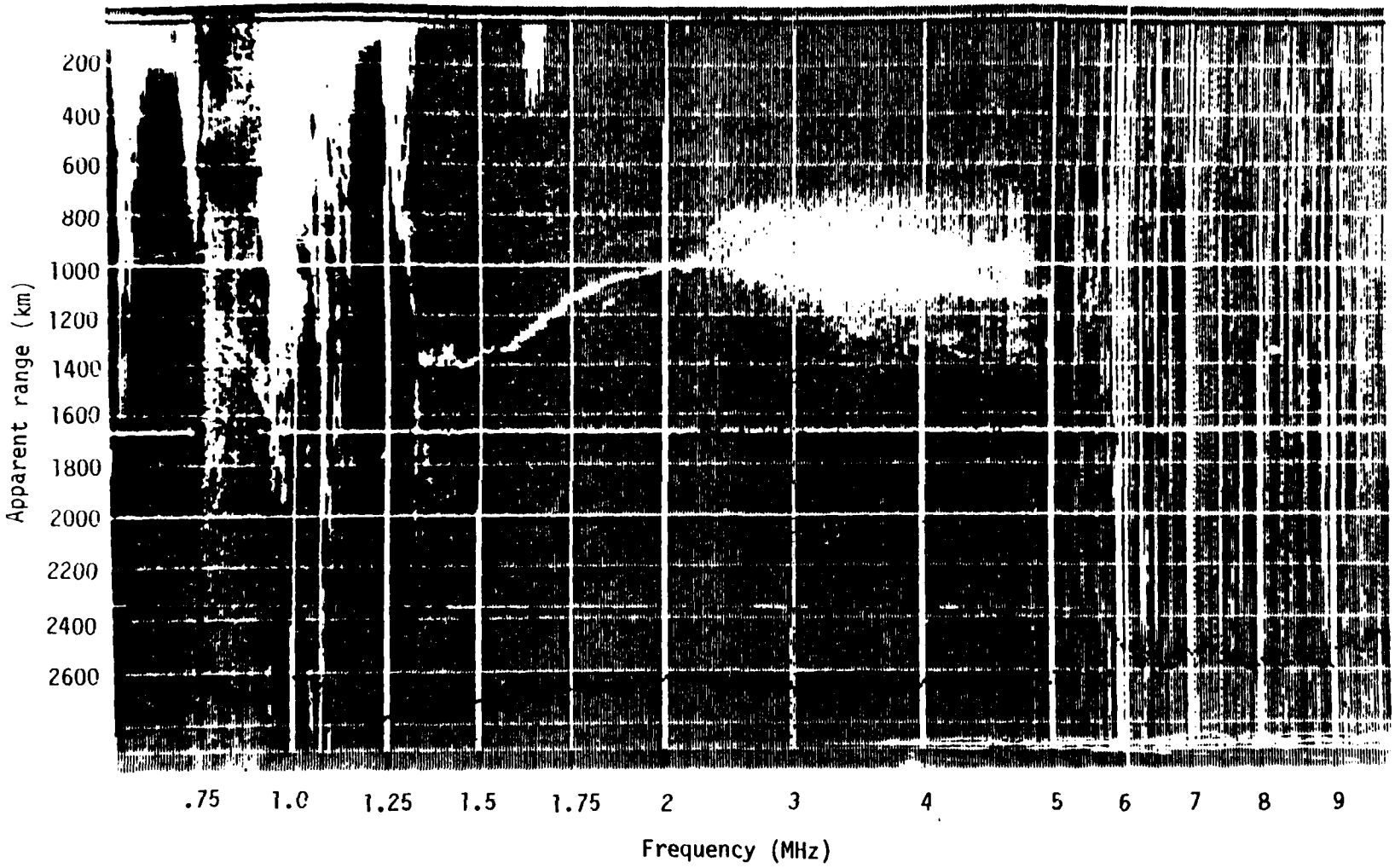

Figure 4. ISIS II 1977 Day 229 1058 Z 2106 LT (4°N, 152°E, 1415 km high). Exploded trace showing spread layer well above (and perhaps below) the smooth trace)[6].

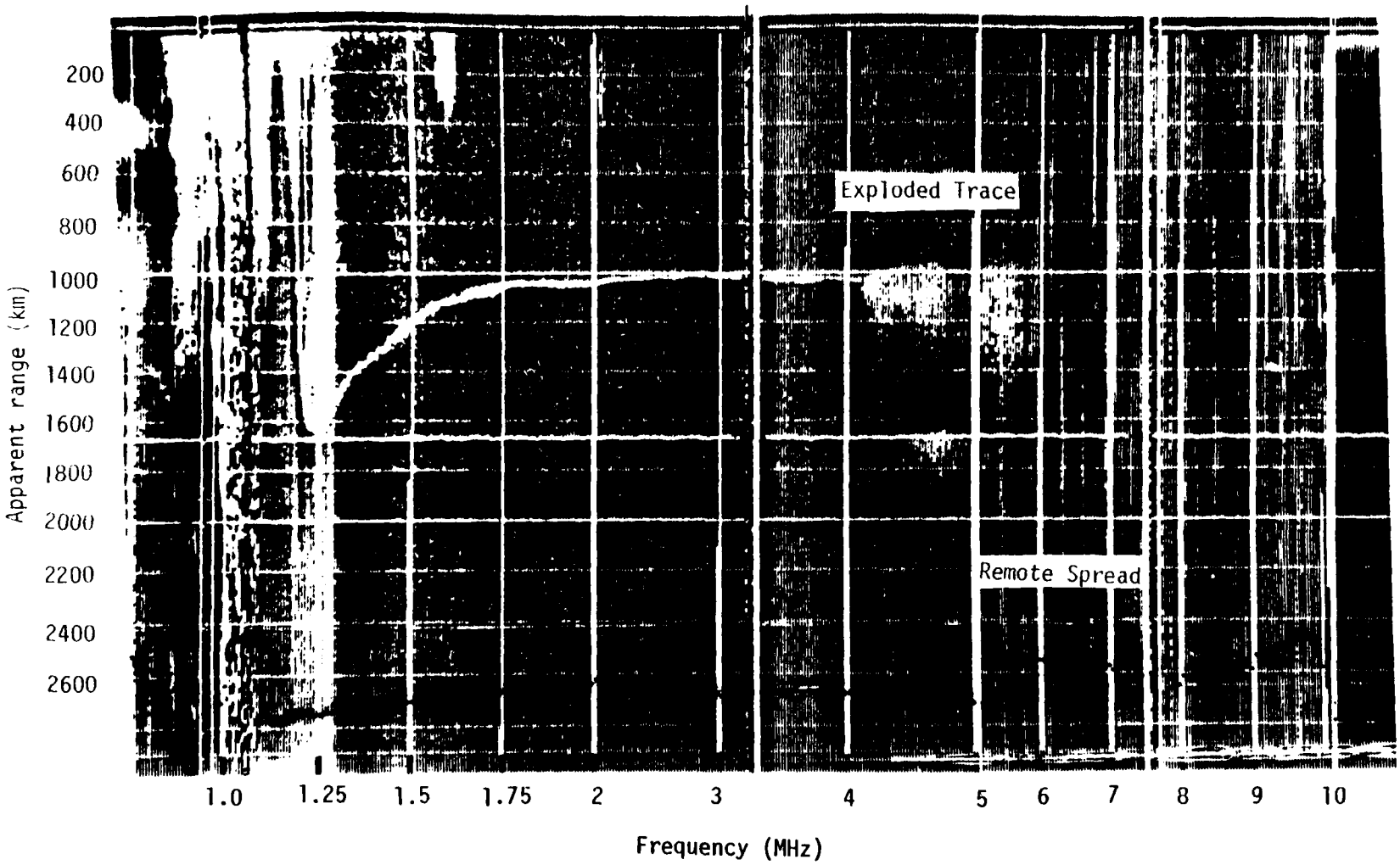

Figure 5. ISIS II 1977 Day 228 1021 Z 2109 LT (6°N, 162°E, 1415 km high). Exploded trace and remote spread[6].

As the satellite travels to the north, successive ionograms provide the three dimensional picture.

This three-dimensional picture has definite ambiguities. For instance, there is no way to tell whether the remote echo is coming from the east or from the west. Also, it would be interesting to know if the irregularities are stationary or are rising as equatorial bubbles are thought to rise. The ISIS topside sounders are unable to answer these questions even though the information could be obtained from the reflected sounder pulses.

A new instrument called the "Digisonde" developed over the last decade at the University of Lowell attempts to use all of the information available from the reflected wave and thereby eliminate some ambiguities that have previously existed with sounding techniques. The parameters that can be determined from the reflected wave are:

1. Range (group travel time)
2. Amplitude
3. Phase
4. Doppler offset from transmitted frequency
5. Angle of arrival
6. Wave polarization (O or X)
7. Curvature of wave front.

The ISIS sounders can only measure the first parameter in a quantitative fashion, while the Digisonde can measure the first six quantitatively. The last three parameters require an antenna array which is more practical for a bottomside sounder than for a topside sounder.

Digital techniques are the key to the Digisonde's success. Such techniques have become feasible in the last decade with the advent of

microprocessors and associated digital integrated circuits. The techniques used by the Digisonde to measure the parameters listed are summarized in Table 5.

Although it is possible to monitor simultaneously the entire five-dimensional complex amplitude space (range, frequency, Doppler, azimuth, and zenith angle), this is neither feasible nor desirable. The quantity of raw data would be excessive. On the other hand, it is important to record as much raw data as possible and not immediately process it into desired results. The Digisonde avoids this dilemma by digitally preprocessing the data to reduce redundancies and to flag each data point with a parameter identification. It also operates in one of two modes: ionogram or drift mode. These modes are complimentary because together they contain all the relevant information of the five-dimensional space. In the ionogram mode, all frequencies and range bins are sampled with full amplitude resolution but with limited information on incidence angles and Doppler frequencies. The drift mode examines only a few frequencies and range bins but obtains full amplitude, incidence angle, and Doppler information. In practice, the ionogram mode is only used occasionally to establish the best frequencies and range bins for the Doppler mode. The Doppler mode then provides all of the data that is normally required. The multiplexed output data still retains its "raw" character but has been reduced to manageable proportions.

The Digisonde is able to reduce significantly the effects of noise interference by phase coding of the transmitted signal. When used as a bottomside sounder, this feature greatly improves the quality of the data which would otherwise be poor due to excessive man-made noise. On the topside of the ionosphere, man-made noise is much less of a problem because the bottomside reflects most of it. However, on some occasions, especially with a highly disturbed ionosphere, man-made noise can be a problem on the topside also. Under these circumstances, the Digisonde would perform better than ISIS.

Table 5. Digisonde measurement techniques (adapted from Reference 3).

WAVE PARAMETER	MEASUREMENT TECHNIQUE
(1) Range	Timing of interval between transmitted and received pulse
(2) Amplitude	Coherent integration of 16 to 256 quadrature samples, log compression of signal, and digitization in 1/2 dB steps
(3) Phase	Ratio of integrated quadrature samples. Synchronization of IF and sampling time
(4) Doppler	Discrete complex Fourier transform
(5) Angle of Arrival	Receiving antenna array and antenna switch
(6) Wave Polarization	Polarized receiving antennas and antenna switch

The Digisonde is a versatile instrument with a wide range of programmable features. Table 6 details these while Figure 6 provides a block diagram of the equipment as it is configured for bottomside sounding.

Table 6 shows that the basic vertical and horizontal resolution of the Digisonde should be similar to that of the ISIS sounders. Indeed the pulse widths of 50, 100, or 150 μsec are close to those of ISIS implying an inherent resolution of 7.5 to 22.5 km. However, the use of phase measurements increases the group height resolution significantly. This group height is given by

$$h' = \frac{c \ \Delta\phi}{4\pi \ \Delta f} \tag{3-2}$$

where c is the speed of light and $\Delta\phi$ is the change in phase with a change in frequency, Δf. Item number 3 in Table 6 shows that a dual step size for frequency can be selected. This is for use with phase measurements. The large frequency step provides high resolution while the small step resolves 2π ambiguities in the phase. For the case of 10 and 90 kHz dual frequency increments, the resolution in virtual height would be

$$\delta h' \approx 100 \text{ m} \tag{3-3}$$

which is two orders of magnitude better than ISIS.

The horizontal resolution and field of view of the Digisonde remain similar to ISIS. However, the Digisonde transmits a 10 kilowatt pulse in comparison to 400 watts for ISIS. This 14 dB greater power output is highly desirable, because ISIS often looses large portions of the topside X and O traces due to inadequate power. The continuous power required by the Digisonde is typically 200 watts, which is certainly within the realm of current spacecraft capabilities.

Table 6. Programmable ionogram parameters (adapted from Reference 4).

#	Function	Dimension	Value
1	Begin frequency	MHz	0, 1, 2, ..., 39
2	End frequency	MHz	1, 2, ..., 40
3	Frequency increments	kHz	5, 10, 25, 50, 100, 200 5 & 20, 10 & 40, 10 & 90, 20 & 180
4	Range increments	km	0.5, 1.0, 1.5, 2.0, 3.0, 4.5, 5.0, 6.0, 10.5
5	Range samples		128, 256
6	Doppler resolution	Hz	0.2, 0.4, 0.8, 1.6, 3.2, 6.3, 12.5, 25.0*
7	Number of Doppler lines		1, 2, 4, 8, 16, 64, 128
8	Amplitude resolution	dB	0.5, 1.0
9	Phase	deg	22.5
10	Pulse repetition rate	Hz	50, 100, 200, 400
11	Pulse width	μs	50, 100, 150
12	Samples per frequency		16, 32, 64, 128, 256
13	Azimuth resolution	deg	30, 60, 90, 120, 180, none
14	Wave polarization		ordinary, extraordinary, ordinary and extraordinary
15	Range start	km	7.5, 37.5, 60.0, 82.5, 112.5, 172.5, 232.5, 352.5, 832.5, 712.5
16	Range window	Pulse period	-4, -3, -2, -1, no ident., +1, +2, +3, +4, +5
17	Receiver gain adj.	dB	0, 6, 12, 18, 24, 30, 36, 42
18	Ionogram rate	hr^{-1}	1 to 120

*Divide by number of antenna configurations used.

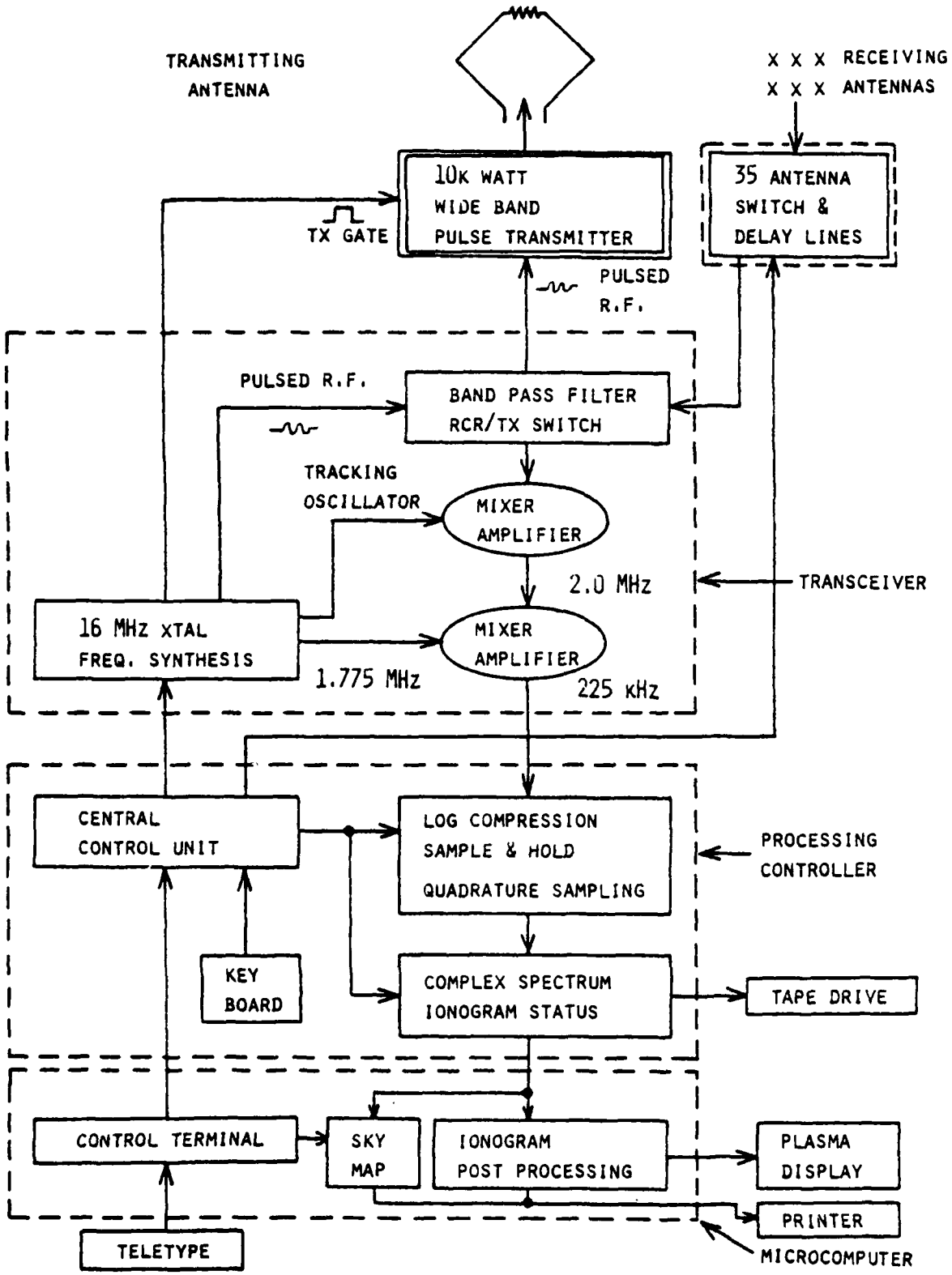

Figure 6. Digisonde system diagram (from Reference 4).

In terms of readily available technology that could be adapted to spacecraft use and would provide a significant improvement in our capability to monitor ionospheric electron density, the Digisonde is a clear first choice. It is our understanding that plans are proceeding to put several Digisonde-like instruments into polar orbits by the end of this decade.

SECTION 4
LASER RADAR (LIDARS)

Laser radars or "lidars" appear to have the greatest long-term potential for high-quality observations of the ionosphere from a satellite. Some lidar observations of the ionosphere have been made with ground based instruments[14-21], but these have been limited to measurements of neutral metal atoms in the lower ionosphere. While these measurements are interesting in their own right, they do not relate directly to ionospheric electron density. It is necessary to measure the concentrations of the major ionic constituents (especially O^+) to obtain electron density. Such measurements require a tunable lidar operating in the vacuum ultraviolet (VUV) near 80 nm (for O^+) instead of 589 nm (for Na). Currently, no tunable lidar exists with a wavelength below 100 nm, but they are certainly possible. If one were developed, it would be ideally suited to a spacecraft instead of a ground-based application, because the lower atmosphere is opaque in the VUV.

A laser radar operates in much the same way as any other radar. It emits a short pulse of radiation (in this case, light) and waits for the pulse to be scattered back by the medium being probed. By measuring the intensity of the returning signal as a function of the time it takes to return, it is possible to determine the density of the scattering medium as a function of distance from the lidar.

Figure 7 illustrates in more detail how the lidar technique would be applied from a spacecraft. The short high-power pulse of light

PRECEDING PAGE BLANK-NOT FILMED

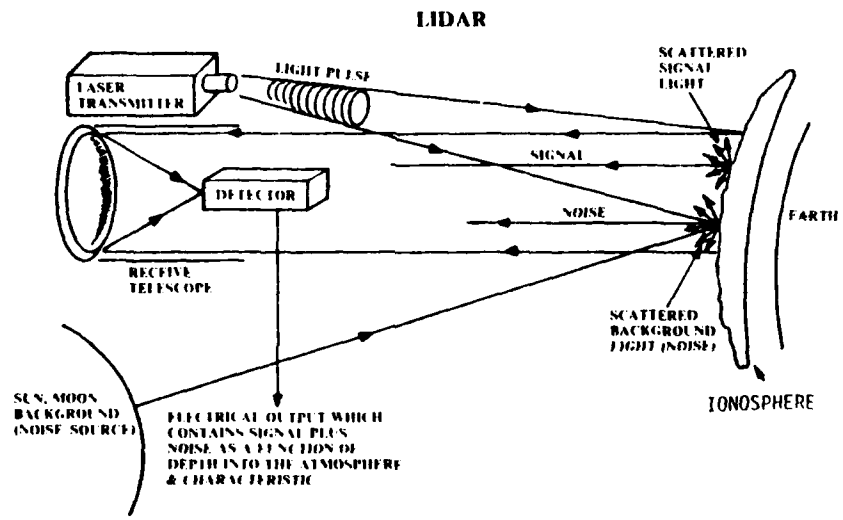

Figure 7. Illustration of a lidar observing the ionosphere (adapted from Reference 22).

from the laser transmitter is directed at the earth's ionosphere. This pulse of light has the appropriate wavelength to be scattered by the ionospheric constituent of interest. A telescope coupled to a photomultiplier tube detector receives scattered light from the laser as well as scattered light (noise) from other sources such as the sun. This light is converted to electrical pulses by a photomultiplier tube (or photodiode) and subsequently processed by on-board electronics.

Lidars offer the possibility of extremely good spatial resolution. Because the typical lidar pulse length is only 30 ns, a range resolution of less than 5 m is possible. This compares with the inherent range resolution of 15 km for the ISIS topside sounders. The horizontal resolution of a lidar is also high. The typical divergence of a laser pulse is 1 mrad which produces a spread of only 300 m at a range of 300 km. By restricting the field of view of the receiving telescope to .2 mrad, a horizontal resolution of 60 m is possible. These resolutions presuppose a sufficiently intense laser pulse to overcome any noise problems. In many current systems, it is necessary to add several range bins or average several pulses together to achieve an adequate signal-to-noise ratio. This decreases the resolution proportionately.

Lidars can, in principle, measure ionospheric density at any location in view of the satellite. They are not limited to viewing the subsatellite track, or just the topside of the ionosphere, as are topside sounders. They have the potential of providing a three-dimensional view of the ionosphere over a large portion of the earth's surface. However, the lidar system would have to operate at more than one wavelength to compensate for the different ionic composition in the various layers of the ionosphere. This could require two or more separate laser transmitters (but the same receiving telescope) if the operating wavelengths are far different. Furthermore, it may be difficult to see, for example, the lower side of the F-layer if that layer is sufficiently

dense to appear nearly opaque to the lidar pulse. Higher lidar pulse power or the use of a different ionic transition and lidar wavelength may mitigate the problem.

Lidars also have significant advantages over passive detection systems. Passive systems normally cannot provide electron density as a function of range but can give only the integrated or column electron density along the line of sight. Passive systems also must rely on some ambient excitation mechanism which may be variable or limited to certain times of the day. Lidars provide a constant excitation pulse and can, under some circumstances, operate night or day with perhaps some degradation in signal-to-noise ratio and resolution during the daytime.

In dealing with lidars observing the ionosphere, it is first necessary to determine the ionic species to be observed and the appropriate transition for that species. Figure 8 shows that O^+ is the predominant species in the F-layer during both day and night. Any lidar instrument must, at least, be able to measure this species if it is to provide F-layer electron density. Other species, notably NO^+ and O_2^+, predominate in the lower regions of the ionosphere and must also be measured. But O^+ is both crucial and difficult to detect. Thus, it has been considered to the exclusion of other species.

The only transitions of O^+ appropriate for a lidar system are the resonant or ground state transitions because these transitions are strong and rapid. Strong transitions are necessary so that a measurable portion of the lidar pulse is scattered back to the detector. Rapid transitions are necessary if the lidar is to obtain range information. Table 7 shows a partial list of O^+ allowed transitions with the longest wavelength resonant transitions circled. As previously mentioned, these all occur in the far ultraviolet region known as the vacuum ultraviolet (VUV).

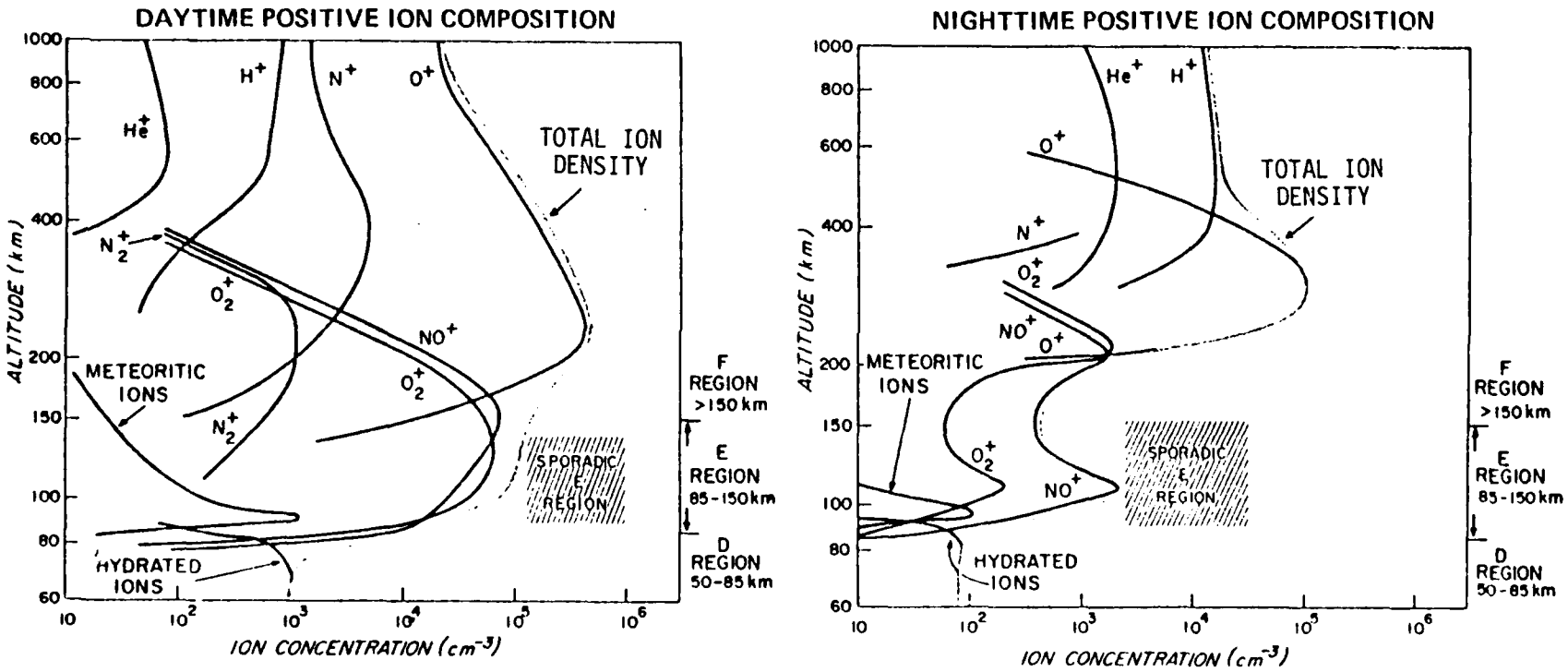

Figure 8. Typical ion profiles for the midlatitude ionosphere at sunspot minimum during the day and night (from Reference 23).

Table 7. O^+ allowed transitions (partial list) (from Reference 24).

No.	Transition Array	Multiplet	λ(Å)	E_i(cm^{-1})	E_k(cm^{-1})	g_i	g_k	A_{ki}(10^8 sec^{-1})	f_{ik}	S(at.u.)	log gf	Accuracy
1	$2s^22p^3 - 2s2p^4$	$^4S^\circ - {}^4P$ (1 uv)	*833.80*	0.0	*119933*	4	12	14	0.43	4.7	0.23	E
			834.462	0.0	119838	4	6	13	0.21	2.3	−0.08	E
			833.326	0.0	120001	4	4	14	0.15	1.6	−0.23	E
			832.754	0.0	120084	4	2	14	0.07	0.77	−0.55	E
2		$^2D^\circ - {}^2D$ (4 uv)	*718.54*	*26817*	*165991*	10	10	32	0.25	5.9	0.40	E
			718.484	26808	165988	6	6	30	0.23	3.3	0.14	E
			718.562	26829	165996	4	4	29	0.22	2.1	−0.05	E
			718.484	26808	165996	6	4	3.1	0.016	0.23	−1.01	E
			718.562	26829	165988	4	6	2.1	0.024	0.23	−1.01	E
3		$^2P^\circ - {}^2D$ (11 uv)	796.661	*40467*	*165991*	6	10	4.4	0.070	1.1	−0.38	E
4		$^2P^\circ - {}^2S$ (13 uv)	644.148	*40467*	195710	6	2	72	0.15	1.9	−0.05	E
5	$2p^3 - 2p^2(^3P)3s$	$^4S^\circ - {}^4P$ (2 uv)	*539.37*	0.0	*185402*	4	12	8.6	0.11	0.80	−0.35	E
			539.086	0.0	185499	4	6	8.6	0.056	0.40	−0.65	E
			539.547	0.0	185341	4	4	8.6	0.037	0.27	−0.82	E
			539.853	0.0	185235	4	2	8.6	0.019	0.13	−1.13	E
6		$^2D^\circ - {}^2P$ (5 uv)	*616.56*	*26817*	*189008*	10	6	18	0.061	1.2	−0.21	E
			616.291	26808	189068	6	4	16	0.061	0.74	−0.44	E
			617.051	26829	188888	4	2	18	0.051	0.41	−0.69	E
			616.363	26829	189068	4	4	1.8	0.010	0.083	−1.39	E

To evaluate the potential of a lidar technique operating in the VUV at 83.3 nm, it is necessary to consider the scattering strength of the O^+ resonant transition relative to competing effects such as total absorption by O, O_2, or N_2. (It turns out that Rayleigh and Mie scattering are not competitive in the ionosphere.) From standard spectral theory[25], it can be shown that the atomic scattering coefficient near an absorption line, σ_ν, is given by

$$\sigma_\nu = \frac{\pi e^2}{mc} f_{abs} \frac{\gamma}{4\pi^2} \frac{N}{(\nu-\nu_0)^2+(\gamma/4\pi)^2} \tag{4-1}$$

where γ is the damping constant, f_{abs} is the absorption oscillator strength, ν_0 is the frequency of the absorption line, and N is the density of the atoms. The integrated scattering coefficient near this line is

$$\int \sigma_\nu d\nu = \frac{\pi e^2}{mc} f_{abs} N \quad . \tag{4-2}$$

Equation 4-1 specifies an extremely narrow line with a width based solely on the lifetime of the upper state. In a real situation, such as the ionosphere, thermal motions of the atoms create considerable Doppler broadening of spectral lines. The Doppler line shape is basically Gaussian and, when combined with the natural line shape given in Equation 4-1, yields the Voigt function. This is a difficult function to handle and unnecessary for our purposes. A Gaussian shape is adequate near the line center where a lidar system would operate. In this case, the scattering coefficient can be written

$$\sigma_\nu = \sqrt{\pi} \frac{e^2}{mc^2} \frac{\lambda_0^2 N f}{\Delta\lambda_D} \exp\{-(\Delta\lambda/\Delta\lambda_D)^2\} \tag{4-3}$$

which maintains the normalization given in Equation 4-2. The Doppler wavelength, $\Delta\lambda_D$, is given by

$$\Delta\lambda_D = \lambda_o\left(\frac{2kT}{Mc^2}\right)^{1/2} \tag{4-4}$$

where M is the mass of the ion, and T is the absolute temperature.

For O^+ at the resonant transition of 83.3 nm and for a typical ionospheric temperature of 1000°K,

$$\begin{aligned}\Delta\lambda_D &= 2.83 \times 10^{-11}\ \text{cm} \\ &= .28\ \text{pm}\end{aligned} \tag{4-5}$$

Consequently,

$$\frac{\sigma_\nu}{N} = 1.23 \times 10^{-12}\ \text{cm}^2/\text{ion} \quad . \tag{4-6}$$

This is a very large cross section compared to various total absorption cross sections at the same wavelength for prominent neutral species in the F-region (see Table 8). O_2 has the largest of the absorption cross sections because 83.3 nm is close to the first ionization edge. In contrast, the first ionization potential of N_2 is only excited by a shorter wavelength photon.

Table 9 shows how the resonant scattering and absorption processes compete at various altitudes from 300 km (peak of the F-layer) to 200 km (bottom side of the F-layer) to 100 km (E-layer). At 300 km the resonant attenuation coefficient is far stronger than any of the absorption coefficients. These absorption coefficients are sufficiently small so that they can be ignored here. At 200 km, the resonant scattering is weaker and the absorption stronger, but the resonant scattering is still predominant. Below 200 km, the O^+ density drops rapidly so that resonant

Table 8. Cross sections at 83.3 nm.

Resonant Scattering:

O^+ $\quad \frac{\sigma_\nu}{N} = 1.23 \times 10^{-12}$ cm^2/ion

Total Absorption:

O $\quad \frac{\sigma_a}{N} = 2.6 \times 10^{-18}$ cm^2/atom

O_2 $\quad \frac{\sigma_a}{N} = 1.5 \times 10^{-17}$ cm^2/molecule

N_2 $\quad \frac{\sigma_a}{N} = 2.3 \times 10^{-18}$ cm^2/molecule

Table 9. Attenuation coefficients.

At 300 km:

$O^+ \approx 10^6/cm^3$	$\sigma_\nu = 1.23 \times 10^{-6}\ cm^{-1}$
$O = 7.5 \times 10^8$	$\sigma_a = 1.95 \times 10^{-9}$
$O_2 = 4.4 \times 10^6$	$\sigma_a = 6.53 \times 10^{-11}$
$N_2 = 8.6 \times 10^7$	$\sigma_a = 1.99 \times 10^{-10}$

At 200 km:

$O^+ \approx 10^5/cm^3$	$\sigma_\nu = 1.23 \times 10^{-7}\ cm^{-1}$
$O = 5.5 \times 10^9$	$\sigma_a = 1.44 \times 10^{-8}$
$O_2 = 2.1 \times 10^8$	$\sigma_a = 3.14 \times 10^{-9}$
$N_2 = 2.6 \times 10^9$	$\sigma_a = 5.98 \times 10^{-9}$

At 100 km:

$O^+ \approx 0/cm^3$	$\sigma_\nu \approx 0\ cm^{-1}$
$O = 4.1 \times 10^{11}$	$\sigma_a = 1.08 \times 10^{-6}$
$O_2 = 2.0 \times 10^{12}$	$\sigma_a = 2.99 \times 10^{-5}$
$N_2 = 8.7 \times 10^{12}$	$\sigma_a = 2.00 \times 10^{-5}$

scattering disappears at 83.3 nm. In about the same region, absorption by the neutral species increases rapidly so that most photons are absorbed. At 100 km the photon intensity drops by 1/e in .5 km. Hence, the atmosphere appears black to 83.3 photons at 100 km.

This absorption at 100 km is useful because it strongly limits background problems and because it eliminates any radiation hazard to people. At night, the background near 83 nm should be almost non-existent except perhaps in auroral regions. During the day, the background for a downward looking satellite sensor should come from resonant scattering of sunlight by O^+. The flux of sunlight at 83 nm is about 7.4×10^8 photons/cm^2-sec-nm. A lidar of modest capabilities can compete with this background enabling daytime as well as nighttime measurements. Some high power laser systems that could be put on a satellite pose potential eye hazards if pointed at the earth. But strong atmospheric absorption at 83 nm affords more than ample protection against such hazards for the lidar discussed here.

When the O^+ density is near or above $10^6/cm^3$, a lidar looking at the O^+ line will have difficulty seeing past the peak of the F-layer. Table 9 shows that $1/\sigma_2$ = 8 km for $[O^+] = 10^6/cm^3$. This means that the peak of the F-layer can become optically thick to the lidar pulses and block the view of the bottom side. This problem would be most pronounced where the F-region is strongest (during solar maximum in the daytime near the equator) and less pronounced to non-existent where the F-region is weak (during solar minimum at night away from the equator). Additional lidar pulse power can compensate, to some extent, for this problem.

Because no current tunable lidar system works in VUV at 83 nm and because no lidar has been flown on a spacecraft, there is a substantial question of the practicality of this technique. Current ground based lidars are large and heavy, require substantial average power, and are tempermental. However, lidar technology is rapidly evolving so that it is

reasonable to believe that a practical lidar system similar to the one discussed here will be available within the near future.

NASA has long recognized the potential of space-borne lidars for many types of atmospheric observations and now feels that the technology has advanced sufficiently to propose an ambitious lidar research program for the Space Shuttle. Table 10 shows a partial list of lidar experiments that NASA hopes to pursue. Those identified with arrows are particularly pertinent to the ionosphere. It is worth noting that the shortest wavelength under consideration is about 200 nm, which is at the boundary of the VUV, not far from the 80 nm necessary to work with O^+.

Figures 9 and 10 show drawings of a lidar instrument and integration of that instrument into the Space Shuttle. Although the lidar equipment shown is large, it is comparable to other equipment NASA intends to fly. The lidar power requirements, however, take a disproportionate share of that available to all experiments.

One of the more interesting lidar experiments planned for the Space Shuttle involves looking for Mg^+ in the E region using an Mg^+ resonant transition. Table 11 presents lidar parameters which NASA expects to achieve and which would yield meaningful data. Most of these parameters are typical of lidars in operation today. The factor limiting performance is the pulse energy of .002 joules. Even with this limitation, Figure 11 shows that adequate resolution is possible under a variety of conditions.

A lidar looking for Mg^+ at 279 nm has much the same problem as a lidar looking for O^+ at 83 nm. The resonant scattering cross section for O^+ (1.23×10^{-12} cm^2/ion) is a little smaller than for Mg^+ (4.27×10^{-12} cm^2/ion), but the density of O^+ is usually several orders of magnitude higher than Mg^+. Furthermore, the daytime solar background near the O^+ line is more than an order of magnitude smaller than near the Mg^+ line.

Table 10. Partial list of lidar experiments that NASA considers feasible for the Space Shuttle. Arrows indicate those of interest to ionospheric studies (adapted from Reference 22).

EXPERIMENT CLASS	WAVELENGTH - NM	LASER HARDWARE	DETECTOR	SYSTEM CONSIDERATIONS
CLOUD TOP HEIGHTS & SURFACE ALBEDO TROPOSPHERIC AEROSOL PROFILES NOCT CLOUD & CIRCUMPOLAR PART LAYER PROFILE STRAT. AEROSOL BACKSCAT. PROFILE	1060 (S)	Nd YAG FREQUENCY DOUBLED	DOUBLE PMT (ONE COOLED NEAR IR)	• [illegible] METER RECEIVER • ORBIT ADJUSTABLE SECONDARY • [illegible] RANGE • [illegible] REPETITION
ALKALI ATOM PROFILES	589.0 (Na) 769.9 (K) 670.7 (Li)	NARROW BAND TUNABLE DYE LASER PUMPED WITH Nd YAG DOUBLED	SINGLE PMT	
IONOSPHERIC METAL IONS	279.6 (Mg)	NARROW BAND TUNABLE DYE DOUBLE PUMPED WITH Nd YAG DOUBLED	SINGLE PMT	
CHEMICAL RELEASE DIAGNOSTICS	589 (Na)	NARROW BAND TUNABLE DYE LASER PUMPED WITH Nd YAG DOUBLED	SINGLE PMT	
	493.4 (Ba)	NARROW BAND TUNABLE DYE LASER PUMPED WITH Nd YAG TRIPLED	SINGLE PMT	
STRATOSPHERIC OZONE PROFILES	280-300	NARROW BAND TUNABLE DYE LASER DOUBLED PUMPED WITH Nd YAG DOUBLED	SINGLE PMT	
MESOPHERIC OH PROFILE	300		SINGLE PMT	
THERMOSPHERIC NO PROFILE	215		SINGLE PMT	
TROPOSPHERIC H_2O PROFILE	720 (2) 940 (2)	TWO NARROW BAND TUNABLE DYE LASERS PUMPED WITH Nd YAG DOUBLED	SINGLE PMT	ORBIT ADJUSTABLE LASER MOUNT NEAR SIMULTANEOUS LASER PULSES
SURFACE AND CLOUD TOP PRESSURE TROPOSPHERIC PRESSURE PROFILE TROPOSPHERIC TEMPERATURE PROFILE	760 (2) 760 (2) 760 (2)		SINGLE PMT SINGLE PMT SINGLE PMT	
TROPOSPHERIC NO_2 PROFILE	442.2 AND 448.0		DOUBLE PMT	
COLUMN CONTENT AND ROUGH PROFILES OF FOLLOWING SPECIES O_3 (9.6 μM), NH_3 (10.6 μM), CFM's (10.7 μM), C_2H_4, CCl_4, C_2H_5Cl, H_2O, ETC STRATOSPHERIC SPECIES MEASUREMENT AT TANGENT ALTITUDE O_3, NH_3, CFM's, HNO_3, ClO, H_2H_4, CCl_4, $ClONO_2$, ETC (TWO SATELLITE TECH.)	TWO IN 9-11 μM REGION	CW CO_2 DISCRETELY TUNABLE WITH HETERODYNE DETECTION TWO WAVELENGTHS	CRYOGENIC INTEGRATED WITH LASER (TWO DETECTORS)	SWING AWAY FOLDING MIRROR OR LASER TRANSMIT RECEIVE THROUGH DETECTOR PORT
		PULSED CO_2 DISCRETELY TUNABLE HETERODYNE DETECTION TWO WAVELENGTHS		SWING AWAY FOLDING MIRROR
ALTITUDE DISTRIBUTION OF ATMOSPHERIC CONSTITUENTS				
STRATOSPHERIC AEROSOL COMPOSITION	MULTIPLE IN 9-11 μM REGION			
CIRRUS ICE/WATER DISC	532	Nd YAG DOUBLED - POLARIZED	DOUBLE PMT WITH POLARIZATION SEPARATION	
THERMOSPHERIC Mg, Mg^+ and MgO PROFILE	279.6, 285.2 and 500	THREE NARROW BAND TUNABLE DYE LASERS TWO DOUBLED AND PUMPED WITH Nd YAG TRIPLED AND ONE PUMPED WITH Nd YAG DOUBLED	TRIPLE PMT	
SODIUM TEMPERATURE AND WINDS	589	NARROW BAND TUNABLE DYE LASER PUMPED WITH Nd YAG DOUBLED	FABRY PEROT INT. WITH MULTIPLE RING DETECTOR	
CLOUD TOP WINDS PROOF OF PRINCIPLE	530	SPECIAL VISIBLE LASER LONG PULSE >3 μs VERY NARROW BAND		
TROPOSPHERIC AEROSOL WINDS PROOF OF PRINCIPLE	530			
VERTICAL PROFILE OF ATOMIC OXYGEN	225 (TRANSMIT)	SPECIAL LASER MODE LOCKED	SINGLE PMT	

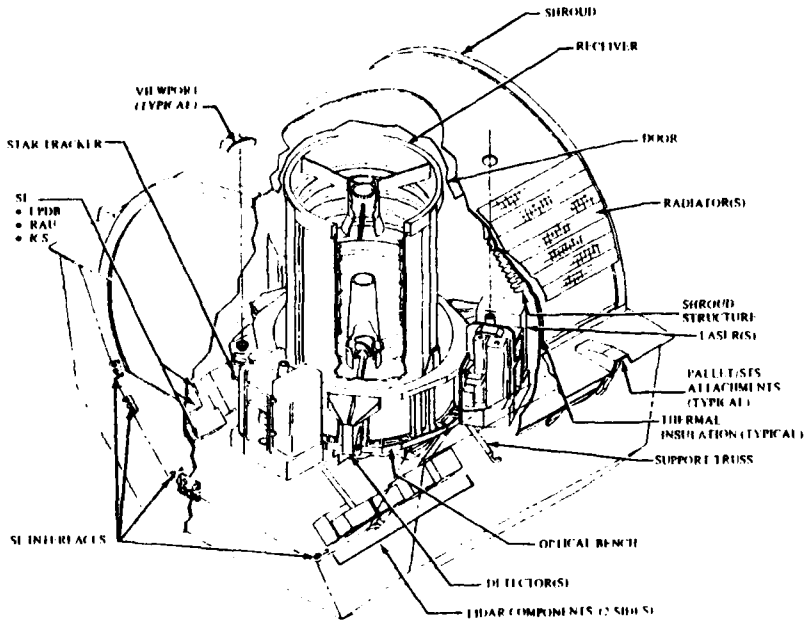

Figure 9. Proposed lidar instrument for the Space Shuttle (adapted from Reference 22).

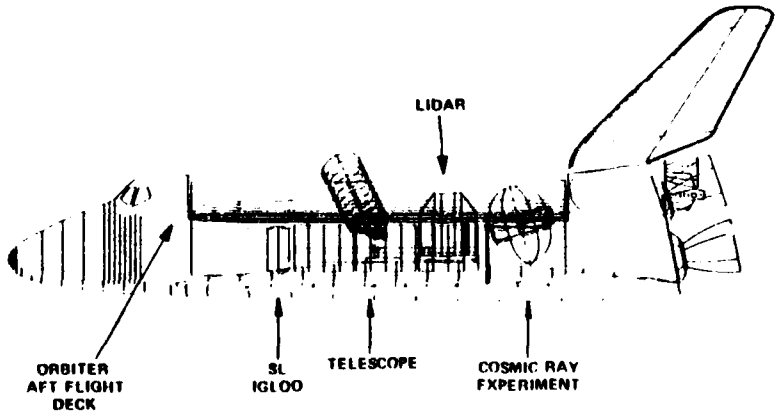

Figure 10. A lidar instrument integrated into the Space Shuttle (adapted from Reference 22).

Table 11. **NASA specifications for a Nd:YAG-Dye laser system to be flown on the Space Shuttle to measure Mg^+ in the ionosphere. (Adapted from Reference 26).**

Wavelength	=	279.6 nm
Laser Line Width	=	.6 pm
Pulse Energy	=	.002 J {Limiting Factor}
Pulse Rate	=	30 Hz
Power Consumption	=	2 kW
Receiver Area	=	10^4 cm^2
Receiver Bandpass	=	1.5 nm
Detection Efficiency	=	.02
Receiver FOV	=	.2 mrad
Shuttle Altitude	=	270 km
Mg^+ Backscatter Strength	=	3.4×10^{-13} cm^2 ion^{-1} sr^{-1}
Daytime Background	=	3×10^9 photons nm^{-1} sr^{-1} s^{-1} cm^{-2}

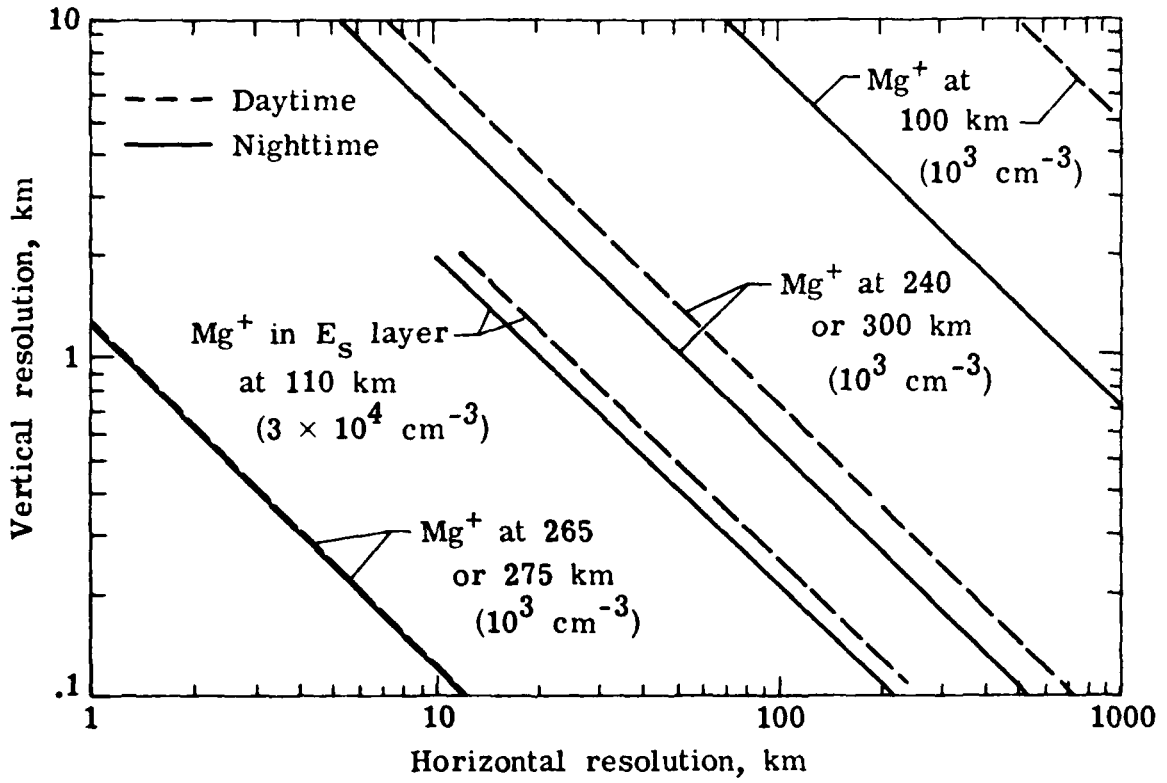

Figure 11. Vertical and horizontal resolution tradeoffs (assuming a ±10% density measurement error) for the proposed NASA Mg^+ lidar experiment (from Reference 26).

Hence, a lidar operating at 83 nm with parameters similar to those of the proposed NASA lidar will produce as good or better O^+ measurements than the Mg^+ measurements anticipated for the NASA instrument.

SECTION 5
THOMSON SCATTER RADARS

Thomson or incoherent scatter radars are very useful for determining electron density as well as other ionospheric parameters. However, this type of radar has only been used for ground based observations and never on a satellite because of the need for high power and large antennas. Figure 12 shows one ground-based facility. With the advent of the Space Shuttle and, consequently, the ability to deploy large, heavy, and complex instrumentation in space, such a space-borne radar becomes more practical. Power is still a problem but may be solved by the deployment of a small nuclear reactor. Los Alamos National Laboratory is reportedly designing such a reactor for space application, and the Soviet Union is known to have deployed a reactor to power a satellite-borne surveillance radar. (The nuclear powered satellite, Cosmos 954, re-entered the earth's atmosphere over northern Canada on the morning of January 24, 1978).

Conventional ionospheric sounding discussed in Section 3 depends on the reflection of radio waves by an electron gas. The reflection process uses the collective behavior of the electrons in a magnetic field and is described by the Appleton-Hartee equation. This is the usual overdense reflection which occurs when the radio frequency equals the plasma frequency, f_p, given by Equation 3-1. At frequencies above the plasma frequency, the radio waves will penetrate through the plasma essentially unimpeded unless they encounter irregularities in plasma density, especially with sharp gradients. In this case, some underdense scattering will occur. Underdense echoes can sometimes be seen by topside sounders but are usually weaker than overdense reflections. For example, if the plasma

PRECEDING PAGE BLANK-NOT FILMED

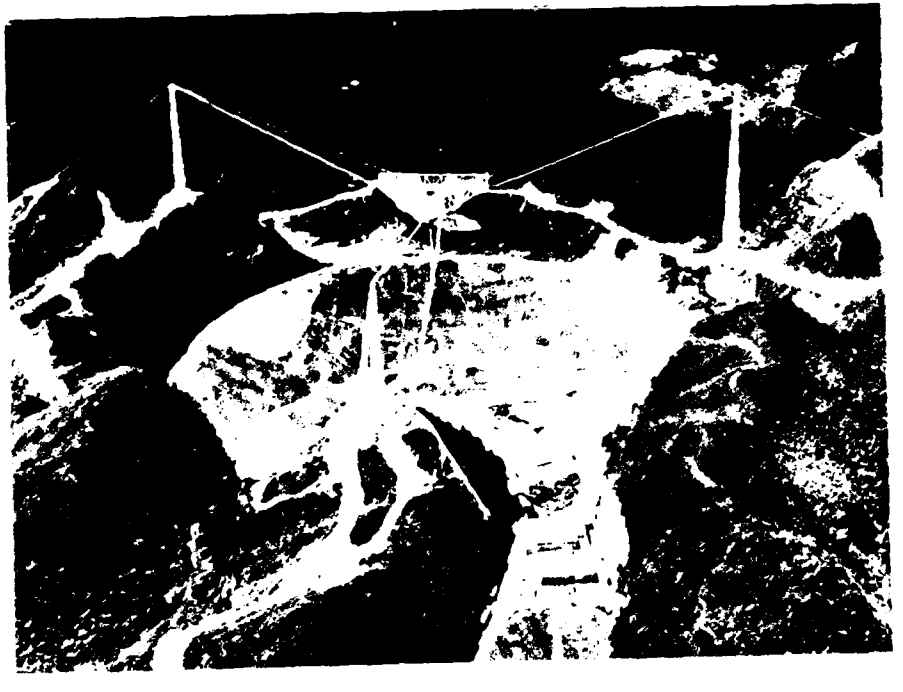

Figure 12. Arecibo Ionospheric Observatory which is often used as a Thomson scatter radar to probe the ionosphere.

contains density irregularities, $\Delta N/N$, that are assumed to be spherically symmetric and given by a Gaussian autocorrelation function with scale length L, then it can be shown that the radar scattering cross section per unit volume is given by[27,28]

$$\delta = \frac{4\pi^3}{C^4} \overline{\left|\frac{\Delta N}{N}\right|^2} f_p^4 \, (2\pi)^{3/2} L^3 \exp\left[-8\pi\left(\frac{L}{\lambda}\right)^2\right] \quad . \qquad (5\text{-}1)$$

This cross section depends strongly on the value of L/λ appearing in the exponential term and will become very small for $\lambda \ll L$. Typical ionospheric irregularities associated with spread-F may have $\Delta N/N \approx .01$ with L of the order of 10 m. In this case, underdense reflections will virtually disappear for $\lambda \lesssim 1$ m unless still smaller density fluctuations exist. Because of the random thermal motions of the electrons and ions, these smaller fluctuations do exist. The scattering caused by these fluctuations is usually referred to as "Thomson" or "incoherent" scatter. Both of these terms are in common use but both are technically incorrect because of the collective effects that occur.

After J. J. Thomson discovered the electron, he showed that a radio wave falling on a free electron will cause it to oscillate and thereby to radiate a scattered wave in all directions.[29] The power reradiated in this way is equal to the power falling on an area given by

$$\sigma_T = \frac{8\pi}{3} \left(\frac{e^2}{mc^2}\right)^2 = \frac{8\pi}{3} r_0^2 \qquad (5\text{-}2)$$

where $r_0 = e^2/mc^2 = 2.82 \times 10^{-13}$ cm and is known as the classical radius of the electron. σ_T is the total isotropic scattering cross section

of a single electron and is called the Thomson cross section. The differential scattering cross section can be written as

$$\sigma_e = 4\pi(r_o \sin \psi)^2 \tag{5-3}$$

where ψ is the angle between the direction of the incident electric field and the observing direction ($\psi = \pi/2$ for backscatter). Note that both Equations 5-2 and 5-3 are independent of frequency.

Because the electrons in any volume, V, have random thermal motions, they will scatter radio waves in a random fashion imparting a random phase to them. This gives rise to the term "incoherent" scatter. A receiver looking for these scattered waves will receive a signal power, P_R, representing the sum of signals with random phases and, therefore, proportional to the density of electrons in the volume illuminated. If this volume is at a range, r, from a transmitter with pulse power, P_T, the power returned per unit area is given by the familiar radar equation

$$P_R = P_T \sigma_e NV/(4\pi r^2)^2 \quad . \tag{5-4}$$

Hence, by measuring the returned power, the electron density N may be determined. The volume, V, must be determined from the geometry of the experiment. The Thomson scattering cross section of an electron, σ, is very small ($\approx 10^{-24}$ cm^2) so that the power returned from the ionosphere is also very small.

The electrons that scatter incident radio waves move with velocities which depend on their temperature causing a Doppler shift in the scattered wave. The Doppler shift appears as a substantial frequency broadening in the returned pulse. The scattered spectrum would be

expected to have a Gaussian shape with a full width at half maximum of 1.42 Δf_e where Δf_e is defined as the Doppler shift of an electron approaching the receiver at a mean thermal speed. This is given by

$$\Delta f_e = \frac{1}{\lambda} (8kT_e/m_e)^{1/2} \quad \text{(Hz)} \tag{5-5}$$

where k is the Boltzmann constant, and T_e is the absolute electron temperature.

W. E. Gordon was the first to demonstrate that this Thomson scattering might be observed by radar techniques and suggested the use of a wavelength of $\lambda = 1.5$ m.[30] When $T_e \approx 1600°K$, 1.42 $\Delta f_e \approx 500$ kHz. Fortunately, this very large bandwidth did not materialize when actual experiments were conducted. K. L. Bowles observed a scattering similar to Thomson scattering, but confined to a much narrower bandwidth. This was correctly attributed to an electrostatic coupling between the electrons and ions.

When the incident wavelength is much larger than the Debye screening distance given by[27]

$$D = (\varepsilon_0 kT_e/4\pi Ne^2)^{1/2} \tag{5-6}$$

where ε_0 is the permittivity of free space, and e is the charge on the electron, the electrons show a collective behavior, and the scattering becomes partially coherent. Because of the coupling of the electrons to the ions and the much slower thermal velocity of the ions, the scattering bandwidth is much smaller than originally predicted by Reference 30. The Debye distance is typically 1 cm or less in the ionosphere compared with a typical radar wavelength near 1 m. Hence, partially coherent scattering should occur.

Pure incoherent Thomson scattering is still possible when $\lambda < D$, but it is exceedingly impractical because of the broad scattering bandwidth that results. Such scattering has been observed in laboratory experiments using a laser instead of a radar. Use of a laser for Thomson scattering is possible with the ionosphere but, probably, impractical. Unlike the lidar system proposed in Section 4, this technique would have the virtue of yielding a direct measurement of electron density, not just ion density.

In the usual case where $\lambda \gg D$, the collective behavior of the electrons and the coupling of electrons to ions offers the possibility of obtaining additional information from the scattered signal. Not only can electron density be determined, but also ion composition if the ratio of electron to ion temperature is known. Conversely, if only a single ion species is present, the ratio of electron to ion temperature can be determined.[32,33] Also, it is possible to use the Faraday rotation of the scattered signal to determine the column electron density. (This latter technique is discussed in a different context in the next section.)

When $\lambda > D$, the scattering cross section given by Equation 5-3 must be modified to give,[34]

$$\sigma_e = \frac{4\pi(r_o \sin\psi)^2}{(1+\alpha^2)(1+T_e/T_i+\alpha^2)} \tag{5-7}$$

where

$$\alpha = 4\pi\ D/\lambda < 1 \quad . \tag{5-8}$$

For typical ionospheric parameters, the denominator of Equation 5-7 is about 3. This means that the scattering cross section in this case is

smaller than the Thomson cross section by about a factor of 3. Because of the much narrower bandwidth of the scattered signal, however, the scattering represented by Equation 5-7 is far easier to detect than pure Thomson scattering. But the detection of any return is still difficult because of the very small cross section involved (typically 3×10^{-25} cm^2).

Figure 13, taken from a study of Thomson scatter radars for the Space Shuttle,[34] shows anticipated noise power as a function of frequency, pulse width, and whether the antenna is pointing toward or away from the earth. This figure shows that frequencies of several hundred MHz exhibit the lowest noise power for an antenna pointed away from the earth. For an antenna pointed toward the earth, the best choice would be frequencies below 100 MHz. Figure 14 is similar to Figure 13 and shows anticipated signal-to-noise ratio versus frequency. The conclusion as to optimum frequency remains the same.

Another consideration is the required power-aperture produce. To simplify consideration of this, the radar wavelength is assumed to be $\lambda = .5$ m (600 MHz) which is near the optimum indicated by Figures 13 and 14. Furthermore, it is assumed that a signal-to-noise ratio of 0.1 is required at a range of 100 km with an electron density of 10^5 electrons/cm^3. In this case, it can be shown that the radar must have a power-aperture produce of at least 10^7 watts-m^2, and that a larger one would be preferable.[34] Figure 15 illustrates the tradeoffs between power-aperture, pulse width, and antenna pointing direction.

To achieve such a large power-aperture produce requires both a high pulse power <u>and</u> a large antenna. The largest antenna operating near 600 MHz proposed for the Space Shuttle is 183 m in diameter. This has an effective area of about 1.3×10^4 m^2. Assuming a power aperture product of 10^8 watts-m^2, implies tha the peak pulse power must be 10 kW. This is

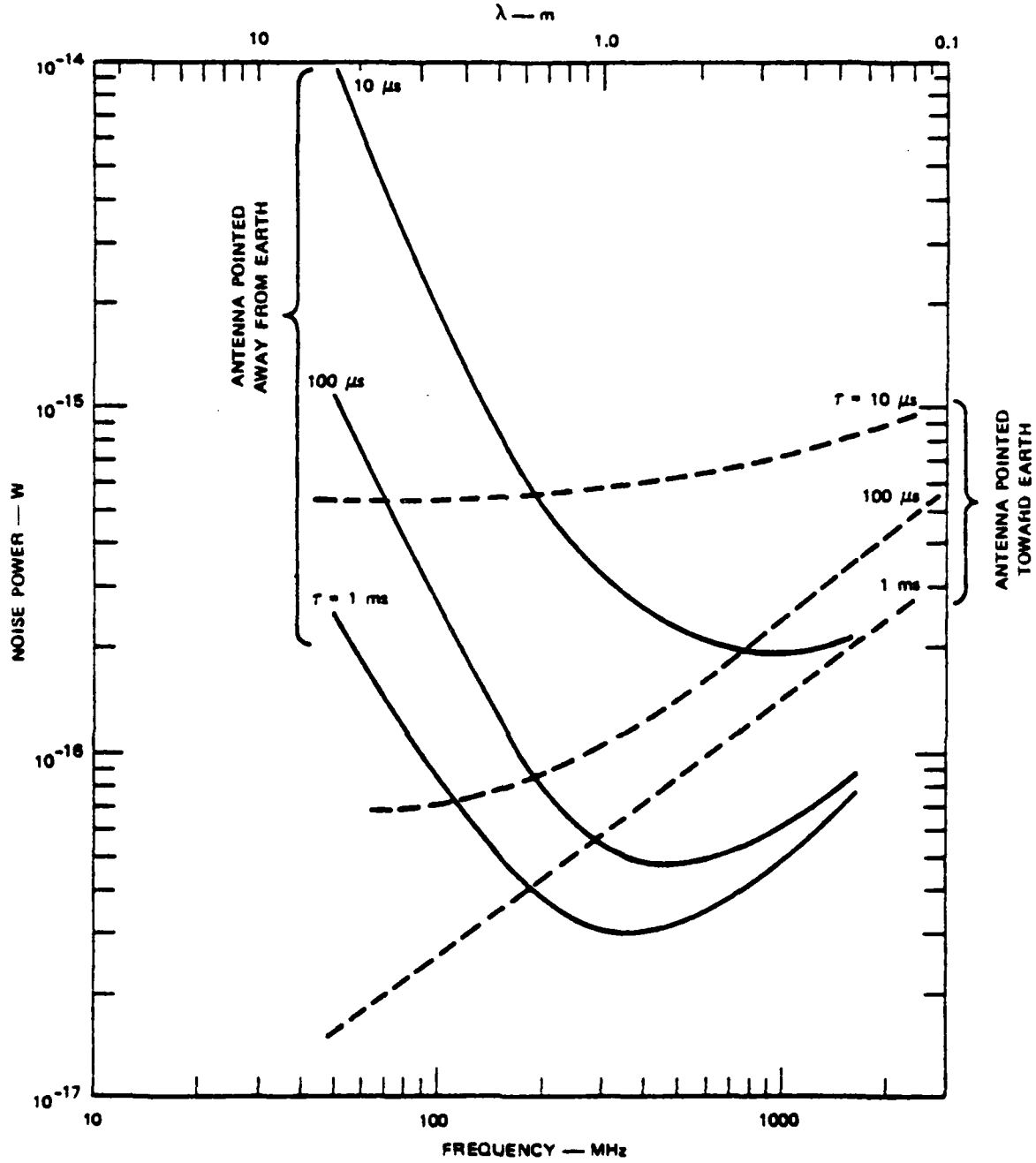

Figure 13. Anticipated noise power versus frequency for a Thomson scatter radar in orbit and pointing either toward or away from the earth. τ is the transmitted pulse width. Shorter pulse widths require a larger receiver bandwidth which in turn admits more noise at a given frequency (from Reference 34).

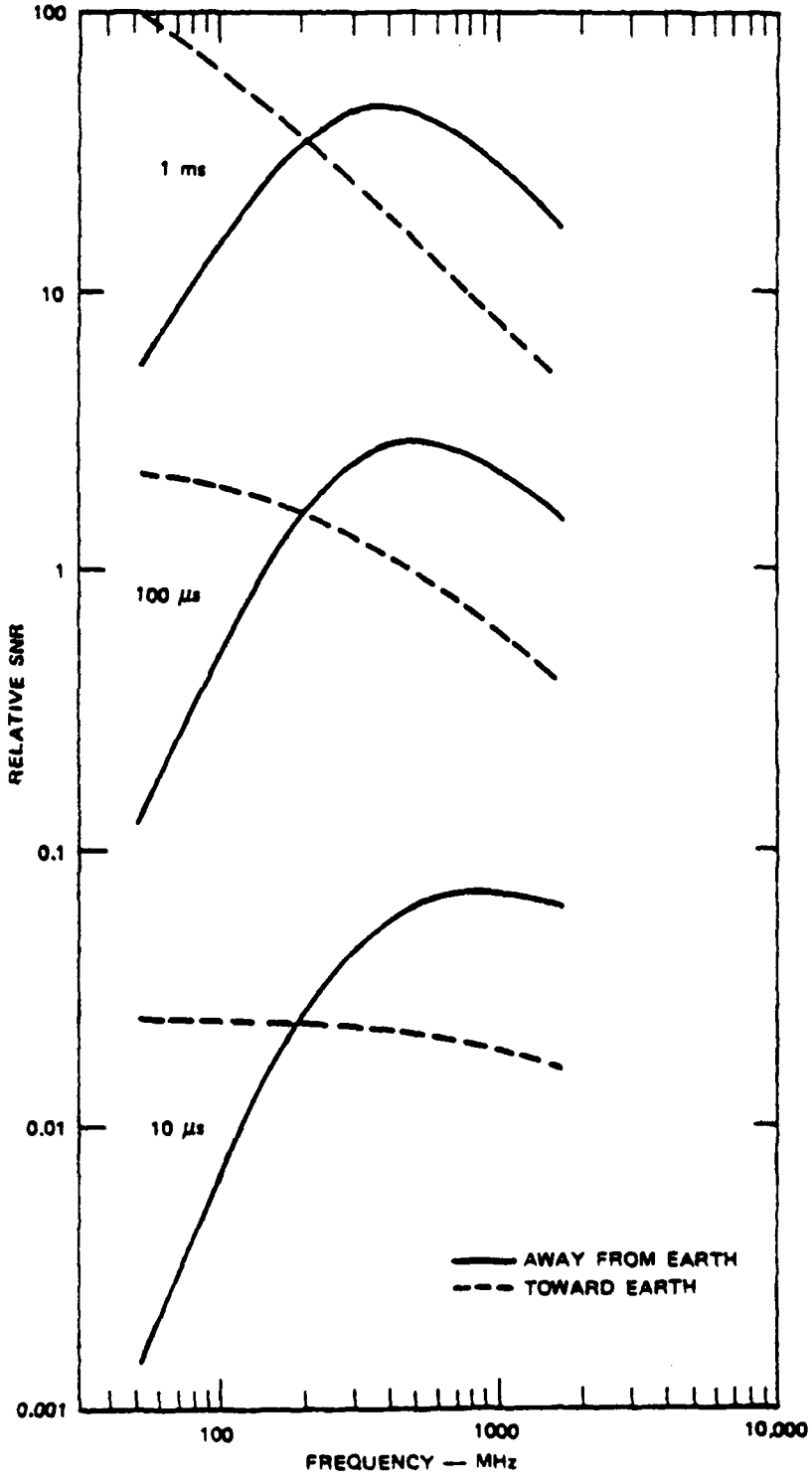

Figure 14. Similar to Figure 13, except showing relative signal-to-noise ratio instead of noise power (from Reference 34).

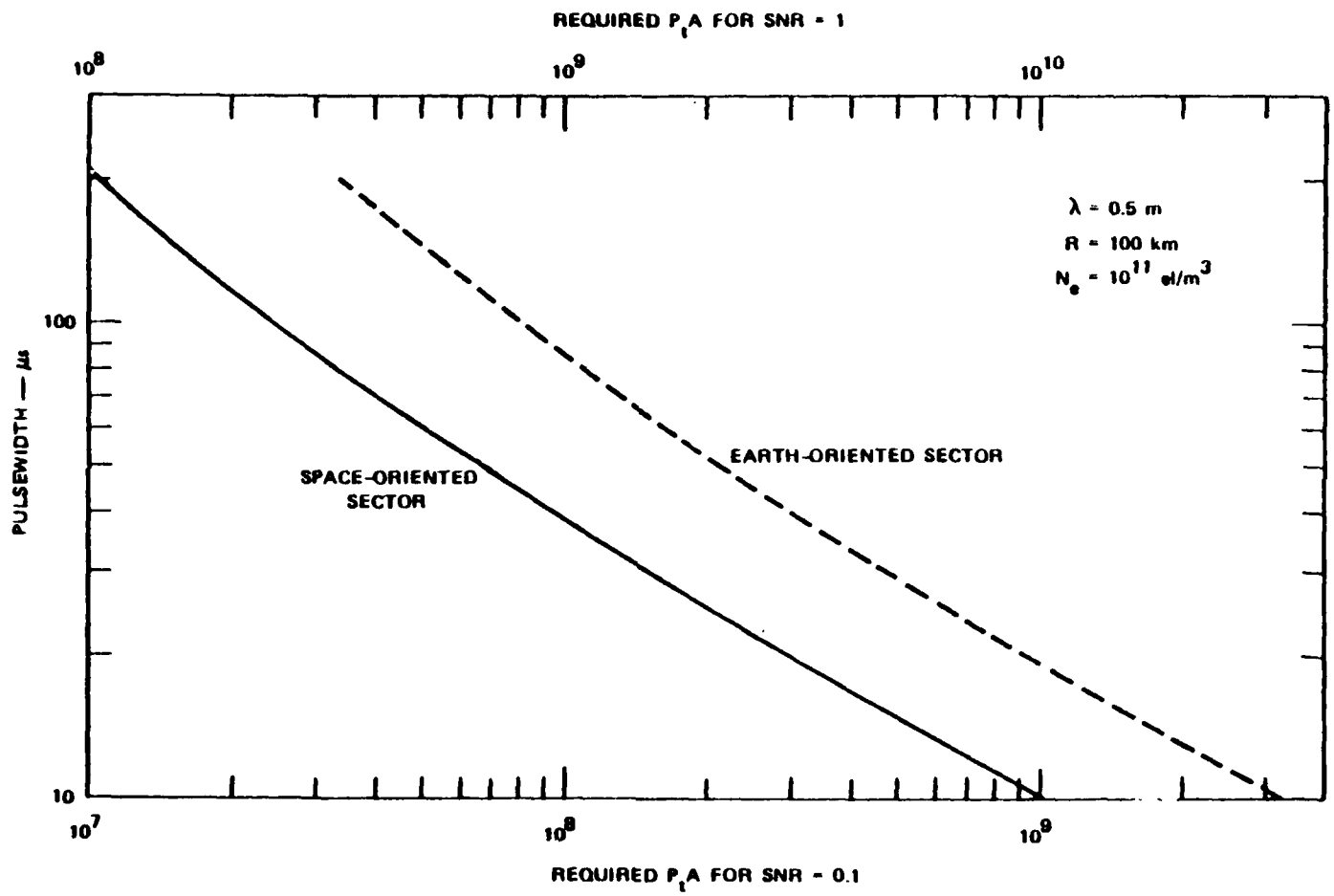

Figure 15. Power-aperture product required in a typical case (from Reference 34).

well within reason if the duty cycle is not too large because the average power requirement would be considerably less. More power may, in fact, be possible. At a peak power of one megawatt, however, antenna breakdown could be a problem.

To illustrate the size of a 183 meter antenna, Figure 16 shows one unfurled from the Space Shuttle. One difficulty with such a large antenna is the drag that it encounters in orbit. Figure 17 shows the expected altitude decrease with time for various size antennas starting at a 300 km altitude. It is clear that a 600 ft ($\approx$183 m) antenna would not remain in a 300 km orbit very long, but would remain much longer in a higher orbit.

Placing the radar in a higher orbit, however, increases the range to the ionosphere and decreases the signal-to-noise ratio. Figure 18 shows this decrease with range. Note that the configurations are for a 10 kW pulse power. A higher pulse power could compensate for this decrease of signal-to-noise ratio with distance.

Although it might seem that higher pulse power is always desirable, this may not be the case for a spacecraft where the average power is limited. In this case, it is necessary to consider the trade-offs between pulse power and duty cycle. Higher pulse power increases the signal-to-noise ratio while a higher duty cycle allows more measurements and a better determination of average ionospheric characteristics. Regardless of the signal-to-noise ratio, it is necessary to do some averaging of the Thomson scatter signal to accurately measure the mean characteristics of the ionosphere.

It can be shown that the standard deviation, σ, of the Thomson scatter measurement varies approximately as [34]

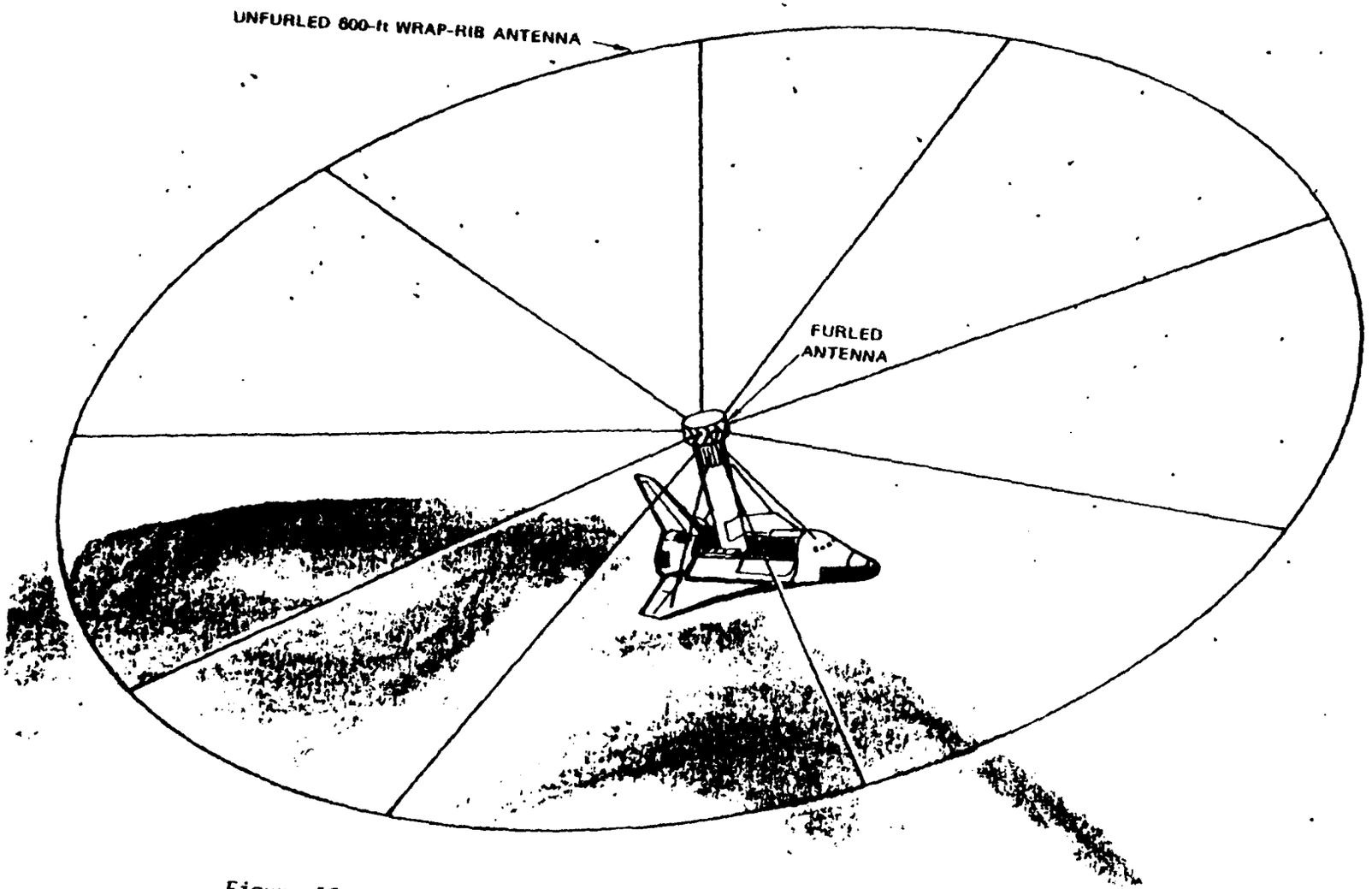

Figure 16. Hypothetical radar antenna unfurled from the Space Shuttle (from Reference 34).

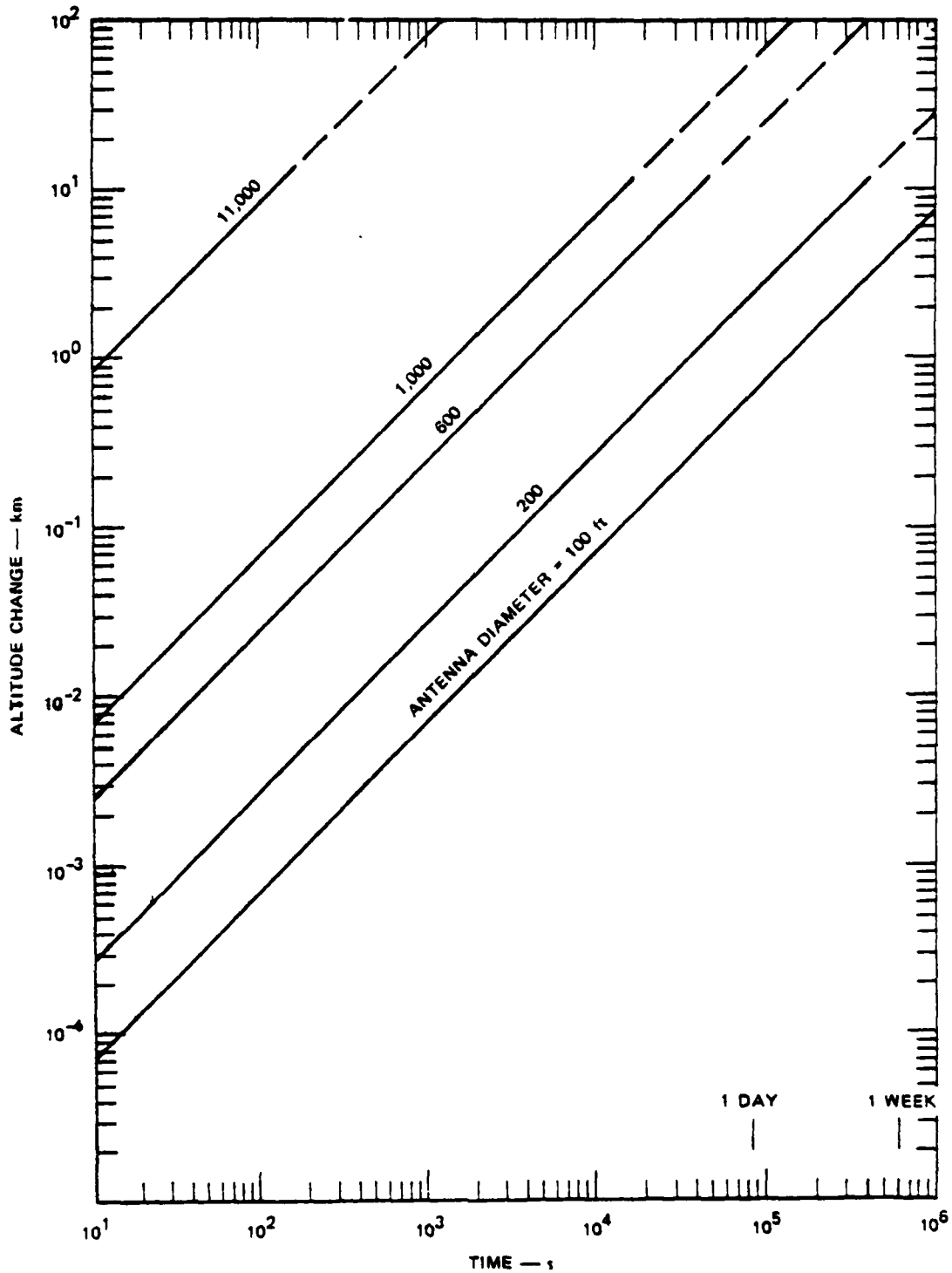

Figure 17. Expected altitude change as a function of antenna diameter and time for an initial altitude of 270 km (from Reference 34).

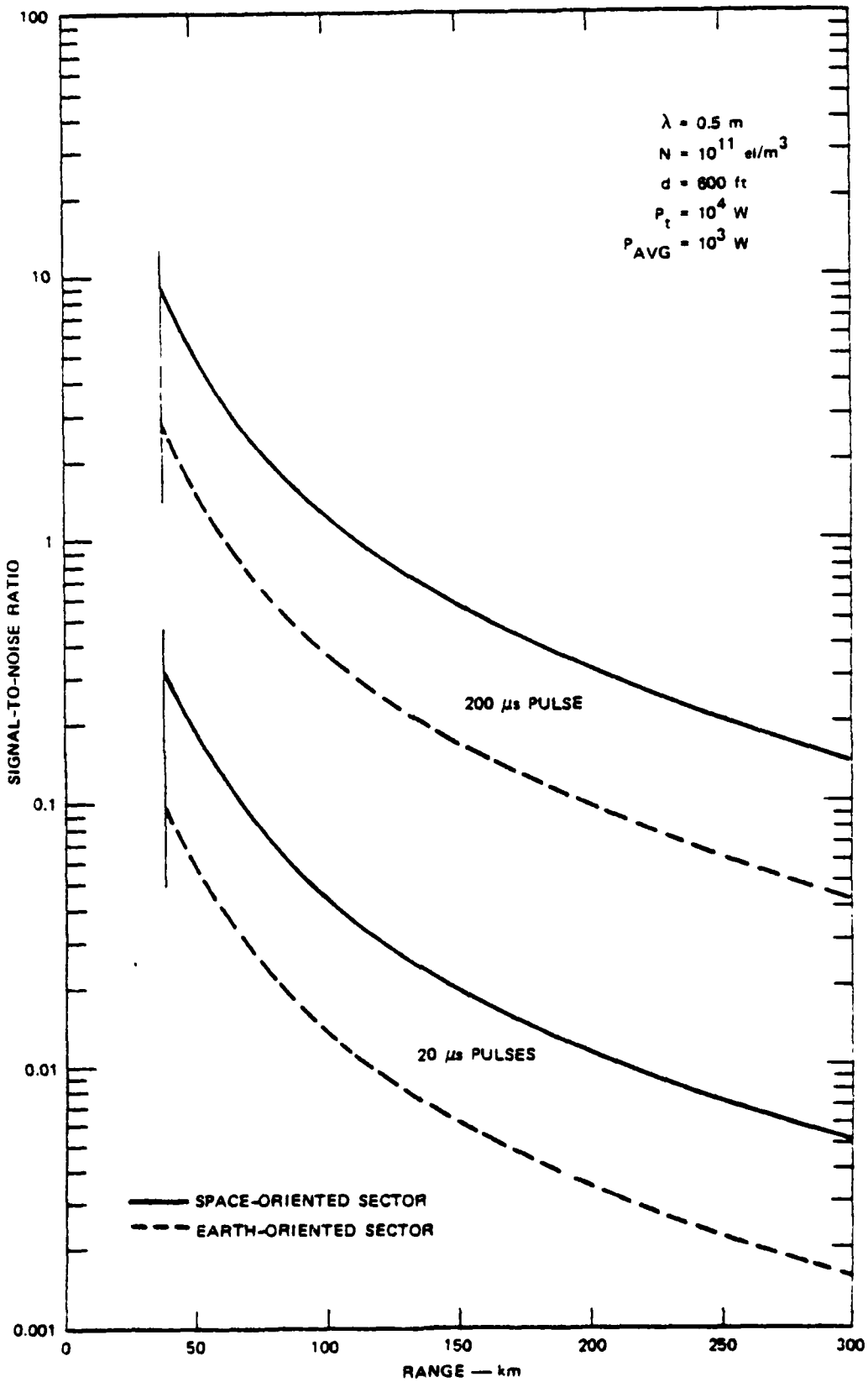

Figure 18. Signal-to-noise ratio as a function of range and pulse width for the radar parameters shown (from Reference 34).

$$\sigma \alpha \left[C + \left(\frac{1}{S/N}\right)\right] \frac{1}{\sqrt{n}}$$

where S/N is the signal-to-noise ratio, C is a constant near 1 and n is the number of samples used in the average. When S/N is small, σ varies in proportion to S/N. As S/N approaches 1, further increases have little effect on σ. In this case, it is better to increase the number of samples, n, in order to improve σ. In practice, it is necessary to add many pulses together to minimize σ. Adding many pulses together leads to a relatively poor horizontal resolution because a downward looking Thomson scatter radar at a Space Shuttle altitude of about 300 km sweeps through a large region of the ionosphere in a short time. Depending on the design of the radar, horizontal resolution could vary from 50 to more than 800 km.

Vertical resolution, in contrast, is a function of pulse length and would vary from 3 km to 30 km for typical radars. This is similar to that of topside sounders while the horizontal resolution is much worse than topside sounders.

Another serious problem is clutter caused by reflections from the earth's surface, the auroral region, or anything other than ionospheric electrons. Figure 19 shows an example of a signal return for a single transmitted pulse. The ionospheric returns are small compared with the ground clutter. The ground clutter can, however, be range-gated out, but doing so limits the pulse repetition frequency. F-region auroral clutter may be similarly strong and not possible to eliminate by range-gating. It is a substantial unknown. Because clutter is often strong, it may be a problem even for a directional antenna by feeding into side lobes.

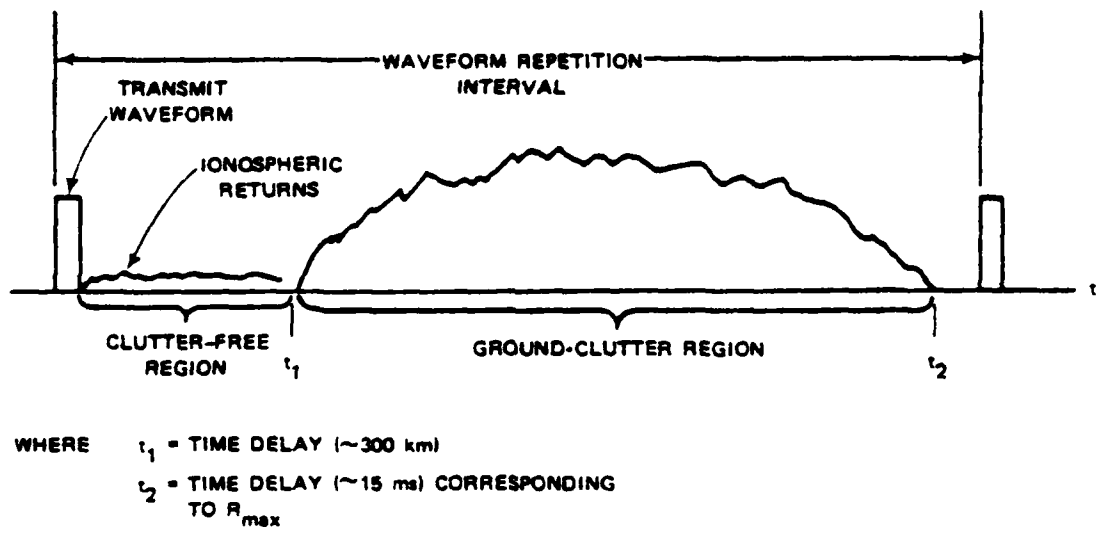

Figure 19. Anticipated signal return for a radar looking toward the earth (from Reference 34).

In summary, Thomson scatter radars in space appear extremely cumbersome although perhaps feasible. They require a large antenna and high pulse power. Vertical resolutions of 3 to 30 km are possible, while horizontal resolutions of 50 to 800 km may be possible. Horizontal resolution depends on the duty cycle and average power available from the radar. Ground clutter limits the pulse repetition frequency. Auroral clutter is potentially a serious problem which would render the radar useless in the auroral region.

SECTION 6
FARADAY AND PHASE METHODS

The phase of radio frequency signals is significantly modified by propagtion through the ionosphere. These phase changes as measured by phase itself, rate of change of phase (Doppler shift) or difference in X- and O- mode phase (Faraday rotation) are directly related to properties of the electron density integrated along the signal path. In this chapter, the potential for using phase measurements in conjuction with other information to find local electron densities along a signal path is reviewed. In Section 6.1, techniques for radio frequencies well above the peak ionospheric plasma frequency are considered. In Section 6.2, techniques applicable when the radio frequencies are near the plasma frequency are explored. Finally, in Section 6.3, the utility of these methods are assessed. It is established that these passive phase methods, which generally operate between a satellite and a ground station, are significantly limited in usefulness. Only the region along the line-of-sight between transmitter and receiver is sampled, and the phase data obtained is directly related to the integrated electron density along the path. This data can be used in conjunction with that gained by other techniques to deduce features of the electron density profile but cannot stand alone for this purpose. Still, phase measurements are relatively easy to take and interpret so that they can profitably be used in conjunction with other monitoring techniques as a routine source of information acting as a constraint on other types of measurements.

PRECEDING PAGE BLANK-NOT FILMED

6.1 FIRST ORDER METHODS

6.1.1 Doppler Shift

If a radio signal in the ionosphere has a transmitted frequency, f, much greater than the plasma frequency

$$f_p = (N_e r_o c^2/\pi)^{1/2} \tag{6-1}$$

(where N_e is electron density, r_o is the classical electron radius (2.82×10^{-13} cm), and c is the speed of light), then the index of refraction of the ionosphere is to first order

$$\mu = 1 - 1/2\ (f_p/f)^2 \quad . \tag{6-2}$$

The phase shift imparted to a signal passing through the ionosphere is thus

$$\Delta\phi = \frac{2\pi f}{c} \int_R^T (1-\mu)\ ds \qquad \text{(radians)} \tag{6-3}$$

where the integration is along the ray path from receiver to transmitter. Therefore, to first order (for which the path is a straight line)

$$\Delta\phi = \frac{r_o c}{f} \int_R^T N_e ds \quad . \tag{6-4}$$

If χ is the zenith angle of the wave vector this can be written as

$$\Delta\phi = \frac{r_o c}{f} \int_{z_R}^{z_T} N_e \sec\ \chi\ dz \tag{6-5}$$

where z_R and z_T are the heights of the receiver and transmitter. Except for the sec χ factor, the integral in Equation 6-5 yields the total electron content (TEC) of the ionosphere along the path. However, unless the path is vertical, χ is not constant, so that the TEC can be found precisely from a measurement of $\Delta\phi$ only if the shape of the electron density profile is known. Direct measurements of $\Delta\phi$ are difficult so often its rate of change is measured. $d\Delta\phi/dt$ is the Doppler shift which is nonzero only if there is some relative motion between the satellite and ground station or if the ionosphere is not stationary. Given Doppler shift data in conjunction with known satellite motion, it is again possible to evaluate the slant TEC as in Equation 6-5. However, any horizontal gradients in N_e will influence the Doppler shift so these gradients introduce uncertainties in the slant TEC. If the ionosphere is stationary and has no horizontal gradients the Doppler shift is

$$f_D = \frac{r_o c}{f} \cdot \frac{d}{dt} (\overline{\sec \chi}) \cdot \int_{z_R}^{z_T} N_e \, dz + \frac{f}{c} \dot{R} \qquad (6\text{-}6)$$

where $\dot{R}$ is the component of the satellite velocity along the path and $\overline{\sec \chi}$ is the mean value of sec χ weighted by N_e. (Note that, at the point of closest approach, f_D will vanish except for the effects of horizontal gradients or nonstationarity.) Again the TEC cannot be obtained without knowledge of the shape of the density profile.

6.1.2 Faraday Rotation

In the absence of collisions, the index of refraction of an electromagnetic wave in a magnetized plasma is[35]

$$\mu = \left[1 - \frac{2X(1-X)}{2(1-X) - Y^2 \sin^2\theta \pm \left[Y^4 \sin^4\theta + 4(1-X)^2 Y^2 \cos^2\theta\right]^{1/2}} \right]^{1/2} \qquad (6\text{-}7)$$

where $X = (f_p/f)^2$

$Y = f_e/f$

$$f_e = \frac{eB}{2\pi m_c} \qquad \text{(electron gyrofrequency)}$$

and θ is the angle of the wave vector with respect to the magnetic field $\vec{B}$. The + is for the "ordinary" wave (O) and - is for the "extraordinary" wave (X). If the frequency is well above the plasma frequency, and the propagation is <u>not</u> close to transverse to $\vec{B}$, then the quasi-longitudinal approximation applies. This gives to first order in X

$$\mu_{\pm} \approx 1 - 1/2\ X \pm 1/2\ X\ Y \cos\theta \tag{6-8}$$

To this same order of approximation, the X and O waves are circularly polarized in opposite senses[36] and, as a result, a plane polarized wave will have its plane of polarization rotate as it propagates if the indices of refraction μ_+ and μ_- differ. From Equation 6-8 it is seen that this Faraday rotation is given by

$$\Omega = \frac{\pi f}{c} \int_R^T (\mu_+ - \mu_-)\, ds \qquad \text{(radians)} \tag{6-9}$$

which to lowest order is

$$\Omega = \frac{e r_o}{2\pi m f^2} \int_R^T N_e\, B \cos\theta\, ds \tag{6-10}$$

If χ is the zenith angle of the wave vector this becomes

$$\Omega = \frac{er_o}{2\pi mf^2} \int_{z_R}^{T} N_e \, B \cos\theta \sec\chi \, dz \quad . \tag{6-11}$$

Hence, measurement of Ω would yield the TEC if B, θ and χ are constant along the path. Since this is generally not true, a Faraday rotation measurement will yield the TEC only if the shape of the electron density is known as is the earth's magnetic field. As with the phase, it is often convenient to measure the rate of change of the Faraday rotation which gives

$$\frac{d\Omega}{dt} = \frac{er_o}{2\pi mf^2} \frac{d}{dt} \left[\int_{z_R}^{z_T} N_e \, B \cos\theta \sec\chi \, dz \right] \tag{6-12}$$

which contains contributions from satellite motion and horizontal gradients in N_e as well as θ and χ.

6.1.3 Application to Properties of Electron Density Profile

6.1.3.1 TEC Evaluation. Many workers have used both Faraday and phase measurements to produce estimates of the TEC using sufficiently high frequencies and proper geometry to allow the first order quasi-longitudinal approximation to apply. Present techniques[37] allow accuracy of a few percent in the raw TEC measurements at ≈150 MHz. However, since Ω and $\Delta\phi$ measurements depend upon the shape of the profile (as well as magnetic field for Ω), this shape is required in order to obtain a unique TEC. Application of a variety of techniques to this question have been considered by Millman[38]. Using a realistic model for the ionosphere, including horizontal gradients, he has found the sensitivity of the TEC estimates to the choice of mean height of the ionosphere. He finds that a variation of ≈50 km in the mean ionospheric height produces changes of ≈10 percent in TEC estimates. This sensitivity is a function of the geometry as well as

the technique used. Still, finding a TEC from measurements of Ω or $\Delta\phi$ requires use of an ionospheric profile, and uncertainties in this profile will result in uncertainties of ± 10 percent in the resulting TEC. Generally, a given measurement serves to scale a presumed shape of density profile.

6.1.3.2 Atmospheric Scale Height Evaluation. Potts[39] has noted that given a measurement of $d\Omega/dt$ <u>and</u> a value of the peak electron density obtained by a separate ionosonde measurement, it is possible to produce some characteristic of the shape of the electron density profile. Since the peak in density contributes most strongly to the Faraday rotation, Potts has attempted to evaluate what is effectively the thickness of the F-region peak by using an α-Chapman profile whose parameters are peak height, h_m, and neutral scale height, H. Potts found that the value of Ω is rather insensitive to variations in h_m so that H can be found from the Faraday rotation measurement when used in conjunction with a knowledge of the peak electron density. Still, this work showed substantial sources of error in horizontal gradients, ionospheric irregularities and deviations from the ideal Chapman profile. When the peak electron density was fixed by an ionosonde 600 km distant, it was found that H had an uncertainty of roughly $\pm$ 25 percent.

6.1.3.3 Profile Parameters by Multiple Measurements. Davies, Fritz and Gray[37] have reported simultaneous measurements of both modulation phase, ϕ_m (similar to group path) and Faraday rotation from 140 MHz transmissions of ATS-6. These measurements are significantly different for a geostationary satellite because the earth's magnetic field is greatly reduced at the orbital radius so that Faraday rotation is largbly unaffected by plasmaspheric electron density (i.e., above 2000 km). In order to translate Ω and ϕ_m measurements into electron content, use was made of monthly median values of peak N_e as obtained by nearby ionosondes in conjunction with an ionospheric model devised earlier by Titheridge[40].

Attempts to use concurrent ionosonde data failed due to substantial and variable horizontal gradients over the several hundred kilometers between the ionosondes and penetration point for the rays. No attempt was made to obtain TEC values from individual measurements. Exclusively monthly median parameters were established. The model electron density profile was parametrized with five quantities: height of maximum N_e, ratio of $[H^+]$ to $[O^+]$ at the peak, ion temperature at the peak, electron temperature at the peak and the electron temperature gradient above the peak. These parameters (only one of which directly relates to the profile) were varied within limits imposed by physical considerations in order to obtain a fit to the measured values of Ω and ϕ_m using a trial and error procedure. It appears that with this many parameters using a mathematical best fit would not be suitable. Using this analysis, Davies[37] finds that uncertainties of ±3 percent in Ω and ϕ_m can produce monthly median ionospheric profiles which are generally consistent with Titheridge's model for physically reasonable parameters. Normally, only a narrow range of any one parameter will allow choices of the other parameters which are reasonable while still fitting the observed median Ω and ϕ_m. However, the authors do not give enough quantatitive details to measure the possible variation in the profile itself.

When these same techniques were applied to ATS-6 measurements in India by Davies, Donnally, Grubb, Rao, Rastogi, Deshpande, Chandra, Vats and Sethia[41], much less satisfactory results were obtained since the propagation path crossed the magnetic equator. As a result, the Faraday rotations were greatly reduced with a corresponding loss in accuracy to ±15 percent. Consequently, fitting the data with choices of ionospheric profiles was not possible in this case even though additional data from 40 MHz was used.

6.2 HIGHER ORDER CORRECTIONS

In Section A, only the high-frequency approximation was considered, that is $f \gg f_p$. Under this assumption the index of refraction of Equation 7 can be expanded to lowest order with adequate accuracy. However, if frequencies, f, comparable with f_p are used for transionospheric propagation, the first order expansion is not generally adequate. The appropriate expression for μ under quasi-longitudinal (QL) conditions is

$$\mu \approx \left[1 - \frac{X}{1 \pm Y\cos\theta} \right]^{1/2} \tag{6-13}$$

which requires (QL condition)

$$1 - X \gg 1/2\ Y \sin\theta \tan\theta \quad . \tag{6-14}$$

As $f \to f_p$ so that $X \to 1$ the QL applies only near $\theta = 0$. The expression for μ can be expanded giving, for $Y \ll 1$,

$$\begin{aligned} \mu_{\pm} &= 1 - 1/2\ X - 1/8\ X^2 + \ldots \\ &\quad \pm Y(1/2\ X + 1/4\ X^2 + \ldots) \\ &\quad + \text{higher order terms in } Y. \end{aligned} \tag{6-15}$$

Thus, for Faraday rotation

$$\begin{aligned} \Omega &= \frac{\pi f}{c} \int_R^T (\mu_+ - \mu_-) ds \\ &= \frac{\pi f}{c} \int_R^T (XY + 1/2\ X^2 Y + \ldots)\ ds \end{aligned} \tag{6-16}$$

$$\approx \frac{\pi}{c} \left[\frac{1}{f^2} \int_R^T ds\ f_e f_p^2 + \frac{1}{f^4} \int_R^T ds\ f_e f_p^4 + \ldots \right] \quad .$$

Apart from constant factors, this can be written to second order as

$$\Omega = \frac{A}{f^2} \int_R^T N_e B \cos\theta\ ds + \frac{A'}{f^4} \int_R^T N_e^2\ B \cos\theta\ ds \qquad (6\text{-}17)$$

This suggests that a measurement of Ω may allow an estimate of $\int N_e^2 ds$ to be made if a high frequency reference value of Ω is obtained to fix $\int N_e ds$. This results from the difference in frequency dependence for $\int N_e^2 ds$. Yeh[42] has detailed the application of this technique to establishing $\int N_e^2 ds$, but it was not applied to any data.

6.2.1 Application to Data

When the high frequency approximation is not adequate, it is necessary to consider both corrections to the index of refraction and to any deviations from a straight line ray path. In early work with 20 MHz and 40 MHz signals, this was regarded as a substantial inconvenience and source of uncertainty. Garriott[43] devised a conversion factor for these refractive effects in order to more accurately find the TEC. He found that if the transmission frequency was only twice the peak plasma frequency a ten percent correction was required in converting Ω to TEC using the first order formulation. Garriott used analytic techniques requiring simple models of the ionospheric profile to estimate second order corrections. This analytic approach has been extended by Ross[44] who established the expansions to higher orders suggesting a general formalism for incorporating corrections. Potts used a different philosophy in accounting for refractive effects at 20 MHz. Instead of expanding μ, he used the full expressions in a ray tracing procedure which required no approximations.

The full effects of X and O path splitting were not included, but Faraday rotation was evaluated along a single curved ray path. Such a procedure excludes the possibility of directly connecting Ω and TEC. Potts found a N_e profile by fitting it to Ω so that the TEC could have been deduced although it was not done.

Davies, et al.[45] have reported on corrections applicable to the 40 MHz phase and Faraday measurements from the ATS-6 satellite. Using typical ionospheric shapes in conjunction with ray tracing, they express an empirical relation between ϕ_m and slant TEC as

$$N_T = A\phi_m(1 + \alpha\phi_m) \tag{6-18}$$

where α typically produces a 3 percent correction at 40 MHz. Similar results were obtained for Ω. This empirical relation is applicable only at this frequency and for the ATS-6 to Boulder geometry. No effort was made to estimate $\int N_e^2 ds$ using this technique, since the estimated uncertainty in ϕ_m is also about 3 percent.

6.3 POTENTIAL VALUE OF FARADAY AND PHASE MEASUREMENTS

Present methods allow measurements of the effects of the ionosphere on HF and VHF signals to be used to find TEC to an accuracy of a few percent. The combination of Faraday rotation and phase measurements can be used with a knowledge of peak N_e to restrict the electron density profile which could produce those measurements. Still, this method has not been applied to find the profile at a specific time.

6.3.1 Use of Frequencies Near the Plasma Frequency.

When transionospheric signals are propagated at frequencies, f, [illegible] ray paths are not straight, and the X and O paths are

different. Both the Faraday rotation and phase effects can be expressed as a series of terms of the general form

$$A \int N_e ds + \frac{A'}{f^2} \int N_e^2 \, ds + \ldots \tag{6-19}$$

so that at lower frequencies there are significant contributions from the integral of higher powers of N_e. These higher powers give their major contributions around the peak so that use of lower frequencies chiefly provides additional information about the peak of the electron density profile.

Two approaches to such a low frequency method might be considered. Either an attempt can be made to better define the profile near the peak or to find $\int N_e^2 ds$ from the measurements. The latter idea may prove difficult, because higher order corrections come not only from integrals of higher powers of N_e but also from the increasingly distorted ray paths when frequencies approach the plasma frequency. As a result, it is difficult to translate changes in Ω or ϕ into the corresponding integrals over the <u>straight</u> path implied by $\int N_e^2 ds$. Furthermore, it will always be necessary to truncate the series leading to substantial uncertainties. For example, if the overall uncertainty of the measured Ω is ±5 percent then $(f_p/f)^2_{max} \approx 0.25$ gives a 10 percent second order correction resulting in a ±50 percent uncertainty in the estimate for $\int N_e^2 ds$.

It appears to be better to avoid trying to measure higher order analogues of the TEC by directly using low frequency measurements to refine the region of the profile near the peak in electron density since this is in fact the quantity of ultimate interest. This will avoid the rather artificial problems associated with the expansion and truncation of the expressions for the path integrals in the presence of complex paths which themselves depend upon the ionospheric profile. Techniques for the

direct fitting of electron density profiles from relatively low frequency measurements of Faraday rotation and phase will now be considered.

6.3.2 Application of Lower Frequency Methods

It has already been demonstrated by Davies[37] that measurements of Ω and ϕ_m to an accuracy of a few percent at 140 MHz can be used, in conjunction with peak density and a physical model of the ionosphere, to severely restrict the range of possible electron density profiles which could have produced those measurements. Our previous discussions suggest that the density profile can be more strongly restricted by use of additional data from similar lower frequency measurements since this data is influenced disproportionately by the peak in the profile.

In order to carry out such a determination of the ionospheric profile, the minimum requirements include a satellite transmitting very stable plane polarized beacon signals at several frequencies such as 400 MHz, 140 MHz and 20 MHz along with other phase related signals at slight offsets from these frequencies for differential measurements. (It might be necessary to have a wider variety of frequencies if measurements at all times are to be useful since the peak density shows substantial variation.) At least one ground receiving station is needed at such a location that the signal path is in a region in which the electron density is desired. If a geostationary satellite is not used the interpretation of the results will be more difficult because horizontal gradients will influence the time rate of change of Ω or ϕ_m. However, if absolute measurements of Ω and ϕ_m can be obtained, as is done for ATS-6, the horizontal gradients may be inferred from the time rate of change.

Once multiple measurements of Ω and ϕ_m are available at several frequencies, and since these values depend differently upon properties of the profile, it is possible to match the experimental values by

variation of the assumed ionospheric profile. This is done by choosing a profile, by ray tracing, and at least for the lower frequencies, by establishing the Ω's and ϕ_m's which would result from this profile. This procedure is then repeated with different profiles until a match with experimental data is achieved. It is very important that the model profiles used be functions of a relatively few parameters which influence different features of the profile in order to avoid ambiguities in best fits. These parameters may be strictly geometrical or, as with Davies[37], a mixture of geometrical and physical parameters.

The works of Potts[39] and Davies[37] demonstrate that the parameter upon which the results depend most strongly is the peak electron density. Both of these efforts used auxiliary data to fix this peak density. This was a key element in their success. Any attempt to fix an electron density profile at a particular time and place will probably be useless unless there is an experimental method to establish, with confidence, the peak density along the ray paths. Note that the ray paths for different frequencies and for the X and O waves are different so that horizontal gradients must be taken into account even if the satellite beacon is geostationary. As a result, some means would be required to estimate these gradients. This could be done by using rate of change data for a nonstationary satellite to find gradients along the satellite track or by using a small array of ground receivers spaced on the same scale of the maximum deviation of the ray paths from straight lines which may be tens of kilometers. This partial redundancy of data would also serve to discriminate against atypical cases and systematic error. Those receivers located along a line perpendicular to the moving satellite track give the potential for mapping out the electron density profile over a large area with a single pass.

Methods which measure phase path deviations such as Faraday rotation or modulated phase are subject to substantial degradation by

scintillations imposed by irregularities in the ionospheric structure[46]. Spread-F and sporadic-E are seen to produce anomalous phase path fluctuations which effectively produce an increased uncertainty in the desired mean value of such quantities as Ω and ϕ_m. As a result, such methods as we have suggested are best applied only during times when the ionosphere is relatively smooth. This is especially true at those frequencies near the peak plasma frequency since scintillation increases strongly with decreasing frequency. In this same vein, it should be noted that the earth's magnetic field is a dynamic quantity[41], and 1 percent variations in Faraday rotation due exclusively to field fluctuations are typical. During magnetic storms greater variations occur. As a result, the application of Faraday rotation data to ionosphere profile parameters will always yield some uncertainty. As indicated by Equation 6-15, the measurement of the path integral of μ or of the modulation phase, ϕ_m, is also subject, to a mild extent, to second order variations in B since $Y \propto B$. However, it is possible to eliminate the first order Y variations by using a phase deviation ϕ_m which is the sum of the left and right circularly polarized phase deviations. This sum includes, to lowest order in Y, a term proportion to Y^2 which should be negligible since $Y < 0.1$ for even the lowest frequencies.

SECTION 7
CHEMILUMINESCENT METHODS

Atmospheric ionic and neutral species can be produced in excited states through a variety of processes including chemical reactions, interaction with precipitating electrons, interaction with solar photons, collisions with photoelectrons, and collisions with thermal electrons in the high energy tail of the distribution. The decay of these excited states produces radiation in the form of photons of energies which are specific to the decaying state. Therefore, the rate of emission of such photons is directly related to the rate at which the excited state decays, that is, the density of atoms or molecules in the state divided by the lifetime. In a steady state, the rate at which the states decay is the same as the rate at which they are populated. Typically observations of this airglow resulting from decay of the excited states are used to relate the intensity to some integrated properties of the radiating region related to the rate of population of the excited state.[47-51]

While airglow methods are potentially applicable to a wide variety of atmospheric regions and conditions, it is our primary interest to look into cases which can yield information about the electron density of the ionosphere.[51-57] Thus, the altitude regime of interest is from 100 km to above 500 km.

In the auroral region, the major source of excited states of the constituents is the precipitation of electrons which have eV or greater energies. These electrons serve to populate excited states by collisions. As a result, airglow techniques in auroral regions chiefly provide information about the distribution of these non-thermal electrons.[48]

Outside the auroral oval, in daytime, solar radiation and the resulting photoelectrons constitute the major mechanisms for population of excited states. Therefore, observations of daytime airglow (which is difficult due to the high background) have the potential for giving information about the character of the solar radiation.

Outside the auroral oval, at nighttime, chemical reactions are the major source of excited states which radiate in the visible and UV so that airglow observations can be related to species densities and reaction rates for those reactions which populate the excited states. Rate constants for the ionic reactions of interest have been studied for some time both in laboratory and aeronomy experiments[58] so that the rates are fairly well known. Furthermore, the neutral species densities are much less variable than the ionic constituents. Models[59] exist which, given suitable parameters, can provide the neutral densities perhaps within a factor of two. As a consequence, it appears possible that observations of the nightglow radiations excited by ionic reactions can be used to provide information on charged species densities. Factors involved in application of this chemiluminescence to evaluation of electron densities will now be considered.

In the following sections, we will discuss those features of atmospheric chemiluminescence which can be applied toward evaluation of ionospheric electron density profiles and practical techniques which will allow this to be done. Sections 7.1, 7.2, and 7.3 give those essential features of nighttime chemistry and resultant emissions which are directly related to the electron density. Atomic oxygen is found to be the most useful emitter. Section 7.4 considers the restrictions on observations which are imposed by actual emission rates while Sections 7.5, 7.6, and 7.7 relate to the capabilities of some practical satellite sensing techniques. Finally, the prospects for application of these methods are given in Section 7.8, and a summary is provided in Section 7.9.

7.1 NIGHTTIME F-REGION IONIC CHEMISTRY

The densities of the prominent neutral species in the F-region, O, N_2 and O_2, are shown in Figure 20. The corresponding charged species are shown in Figure 8 to be O^+, NO^+ and O_2^+. Chemical reactions among these species plus electrons have the potential for providing excited electronic states of any of the six major constituents. The reactions which will be considered[52-53] are given in Table 12. This set of reactions is generally thought to provide the significant features which fix densities of the ionic species.

All of the reaction products can potentially be created in excited states and thus be candidates for sources of emissions which can provide information about the constituent densities. However, the O_2 product is not useful for establishing ionic densities, because it will be swamped by $O+O \rightarrow O_2$. Atomic nitrogen, N, has an excited ^2D state which is produced by the NO^+ dissociative recombination. However, the lifetime of this state is 26 hours which precludes its use. Likewise, the charged species are not promising. O^+ is not a reaction product since it is primarily formed during the sunlit hours or by transport in conjunction with charge exchange with the protonosphere. Reactions producing O^-, O_2^+, and NO^+ all have quite limited energy available for production of excited states so, to the extent to which such states exist, their population by thermal electrons in the high energy tail of the distribution will compete with that by ionic chemistry. There appear to have been no observations of line or band radiation from excited states of these three constituents at night. We are thus left with the most promising source of useful nighttime airglow as atomic oxygen. There are several reactions in Table 12 which lead to O, so that there is potential for populating excited states by a variety of chemical routes. This variety is not desirable, so we will now consider in detail features of the various reactions to find excited states which are populated by a subset of the reactions.

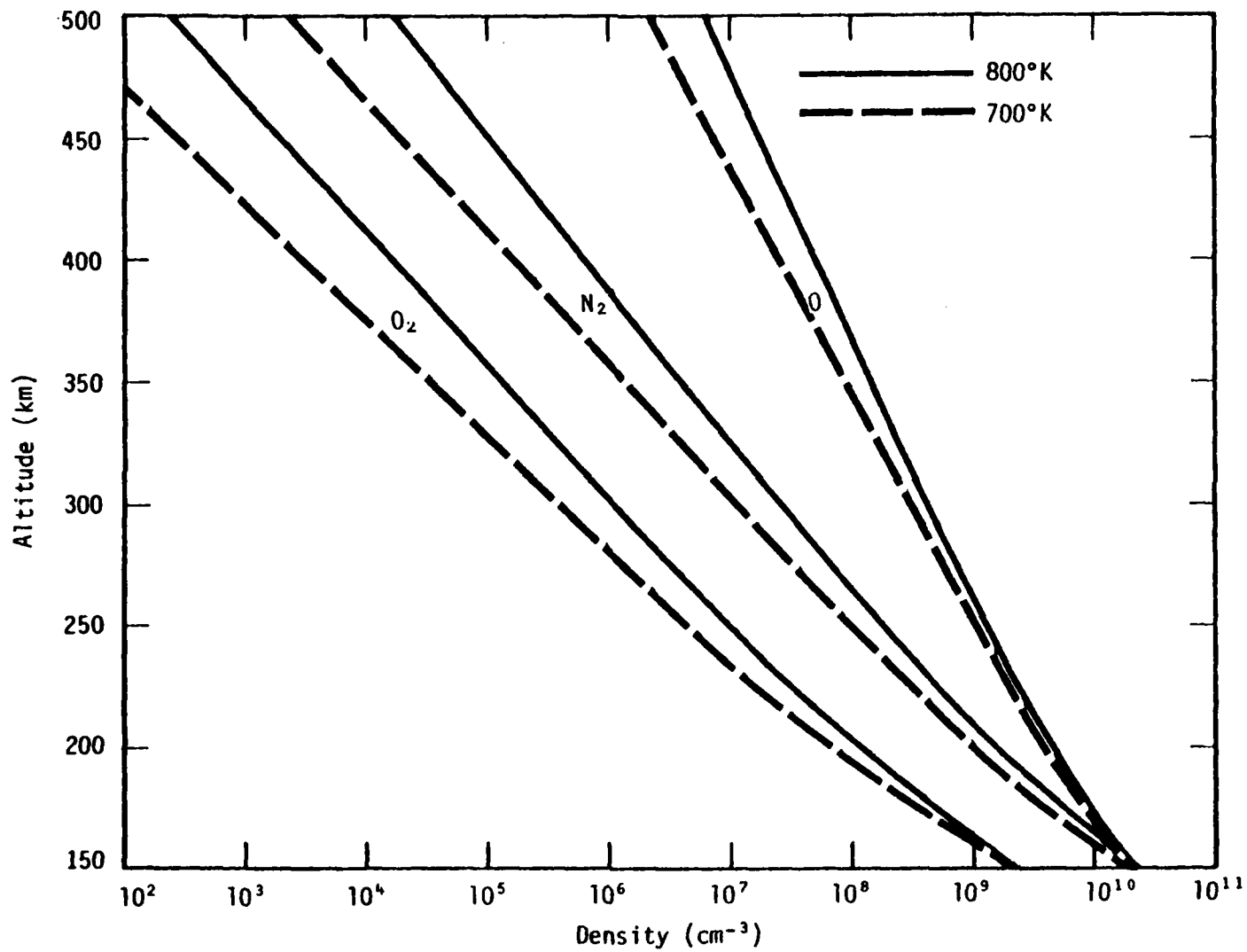

Figure 20. Major neutral species densities at F-region altitudes for exoatmospheric temperatures of 800 and 700°K. (From Reference 54.)

Table 12. Ionic reactions important in nighttime F-region (adapted from Reference 55).

NO.	REACTION		RATE (cm^3/s)
1.	$O_2^+ + e^- \rightarrow O + O + 6.96$ eV	O_2^+ Dissociative Recombination	$2.1\times10^{-7} \left(\frac{T}{300}\right)^{-.63}$
2.	$NO^+ + e^- \rightarrow N + O + 2.76$ eV	NO^+ Dissociative Recombination	$4\times10^{-7} \left(\frac{T}{300}\right)^{-0.4}$
3.	$O^+ + O_2 \rightarrow O_2^+ + O + 1.53$ eV	O_2^+ Formation	$2\times10^{-11} \left(\frac{T}{300}\right)^{-0.4}$
4.	$O^+ + N_2 \rightarrow NO^+ + N + 1.09$ eV	NO^+ Formation	$1.2\times10^{-12} \left(\frac{T}{300}\right)^{-1}$
5.	$O^+ + e^- \rightarrow O + h\nu$ (13.6 eV max)	Radiative Recombination	$3.5\times10^{-12} \left(\frac{T}{300}\right)^{-0.7}$
6.	$O + e^- \rightarrow O^- + h\nu$ (1.46 eV max)	Attachment	1.3×10^{-15}
7.	$O^- + O^+ \rightarrow O + O + 12.1$ eV	Ion-Ion Recombination	$2.7\times10^{-7} \left(\frac{T}{300}\right)^{-0.5}$
8.	$O^- + O \rightarrow O_2 + e^- + 3.7$ eV	O^- Associative Detachment	2×10^{-10}

7.2 POPULATING ATOMIC OXYGEN EXCITED STATES

The states of atomic oxygen, OI, are given in Figure 21 and transitions which have been observed as atmospheric emissions are indicated by darker lines. Excited states populated by reactions are limited by the energy available as well as by selection rules which depend upon the quantum numbers of the states.

NO^+ dissociative recombination[52] has sufficient energy to populate either the $N(^2D)$ or the $O(^1D)$ excited states. However, direct excitation of $O(^1D)$ is forbidden by spin conservation. The reason this dissociative recombination is included is that it appears that the $N(^2D)$ atoms quickly collide with ground state $O(^3P)$ to form $O(^1D)$ so that the net effect is the production of $O(^1D)$. This state has a lifetime of 110 seconds and decays to the ground state by emitting the red 6300A line. (A more complete consideration of NO^+ dissociative recombination will require noting that not all these reactions give $N(^2D)$ and that for a large enough O_2 density $N(^2D)+O_2 \rightarrow NO+O$ serves to compete with $O(^1D)$ production.)

O_2^+ dissociative recombination[52] has an excess energy of nearly 7 eV so it can leave the pair of oxygen atoms in a variety of states: $(^3P,^3P)$, $(^3P,^1D)$, $(^3P,^1S)$, $(^1D,^1D)$, and $(^1D,^1S)$. The distribution of O among the three states is somewhat uncertain. The work of Zipf[56] suggests that this distribution is strongly affected by the vibrational state of the original O_2^+. It appears that if O_2^+ is vibrationally excited to $v \geq 3$ states then the number of $O(^1S)$ states produced per recombination is $k_S \approx 0.1$. This is in agreement with atmospheric experimental results[57]. The number of $O(^1D)$ states produced per recombination, k_D, is also subject to uncertainty. Coggen and Smith[58] give $k_S+k_D = 0.6$ while Chandra et al[59] used $k_D+k_S = 0.4$ and Tinsley[60] used $k_S+k_D = 1$. The sum k_S+k_D is used because of the rapid cascade of the $O(^1S)$ state to $O(^1D)$ with a lifetime of 0.74 sec. It is this transition which gives the 5577A green line. The $O(^1S)$ can also decay to the ground state, but the rate is low so that 94 percent of the ^1S decays lead to the 5577A line.

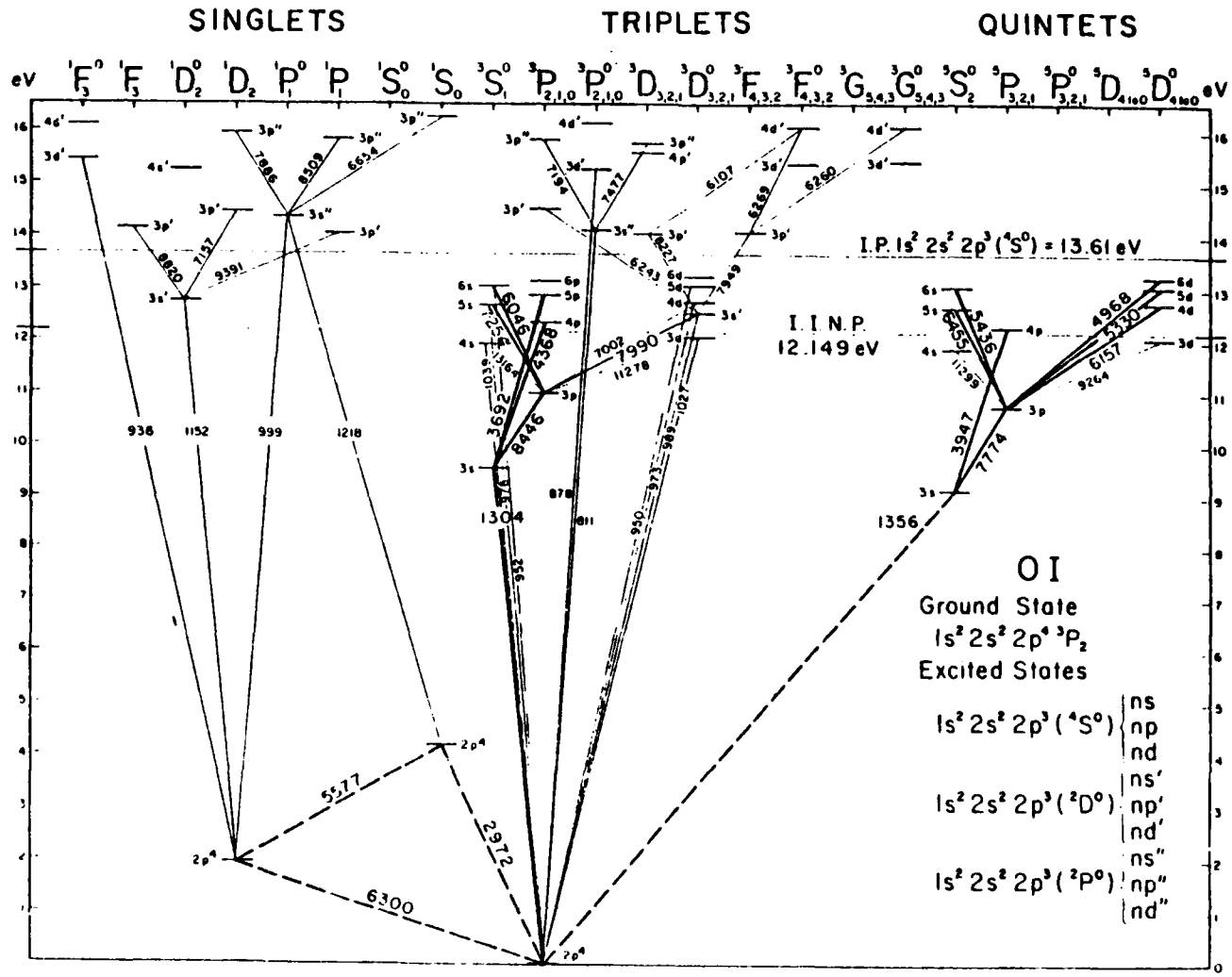

Figure 21. Energy level diagram for atomic oxygen. Transitions which have been identified in the auroral or airglow are shown with thicker lines. (From Reference 53.)

O^+ radiative recombination has an energy excess of 13.6 eV so that, energetically, a large number of excited states may be populated. Tinsley et al.[53] calculated the rate coefficients for the most common excited states; and these are reproduced in Table 13. The authors estimate that the rates have an accuracy of 10 to 20 percent for the larger coefficients although a factor of two would probably be more realistic. The rate for the 905-910Å transition, $\alpha_{905-910}$, is for the continuum to the ground state. Transitions to singlet states are spin forbidden so that the 6300Å and 5577Å lines do not appear. The most promising lines from radiative recombination will be 1356Å and 7774Å.The F-region is optically thick to the 1304Å emission. The 8447Å and 4368Å lines are possible but they are relatively weak.

Table 13. Partial rate coefficients for $O^+(^4S^0)$ radiative recombination yielding emission in transition listed (units are 10^{-13} cm^3 sec^{-1}). (From Reference 53.)

Transition (Å)	700°K	1000°K	2000°K
905-910	4.5	3.8	2.8
1027	1.1	0.9	0.5
1304	5.2	4.0	2.4
1356	10.6	8.1	4.8
4368	0.11	0.08	0.05
7774	7.6	5.8	3.4
8447	3.4	2.6	1.5

Ion-ion recombination gives an excess energy of 12.1 eV to share between the two product oxygen atoms. Olson, Peterson, and Moseley[61] have calculated partial rate coefficients for this reaction. The total rate

coefficient found differs from the experimental value, but it is believed that ratios of the partial rates are reasonable. In Table 14, the fraction of the total rate coefficient is given based on Reference 61. These results are generally thought to be within a factor of two of the correct values. However, these calculations involve approximations in the treatment of complex atomic processes, and the detailed effects of these approximations are unknown. The density of O^- available for ion-ion recombination is influenced by the loss of O^- by associative detachment so that this must be included in the full set of reactions required to establish the rate of production of excited O atoms.

Table 14. Fraction of $O^+ + O^- \rightarrow O + O$ reactions which lead to emissions listed. $[\gamma_7 = 2.7\times10^{-7}\sqrt{300/T}\ (cm^3/sec)]$.

Emission	Fraction, β
1304Å	0.47
1356Å	0.53
7774Å	0.42
6300Å	0.12
8447Å	0.45

7.3 EMISSION RATES OF ATOMIC OXYGEN LINES IN THE F-REGION

In order to get a feel for the magnitude and variation with altitude of the OI emissions, let us consider typical species densities as found in Figures 8 and 20. A set of densities is given in Table 15 for an exospheric temperature of 800°. This temperature fixes the neutral densities. The electron density comes from Figure 8, while the ion densities are adjusted for the steady state in such a way that the total ion density equals the electron density. This means that

AD-A115 398 MISSION RESEARCH CORP SANTA BARBARA CA F/G 4/1
TECHNIQUES FOR REMOTE SENSING OF IONOSPHERIC ELECTRON DENSITY F--ETC(U)
AUG 81 J A BALL, G J FULKS, T E OLD F19628-80-C-0169
UNCLASSIFIED NRC-R-668 AFGL-TR-81-0331 NL

2 of 2

END
DATE
FILMED
7-82
DTIC

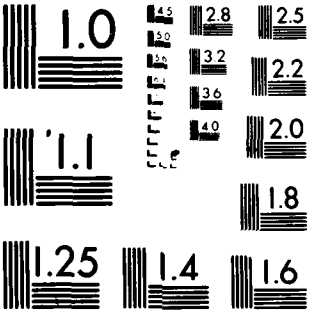

MICROCOPY RESOLUTION TEST CHART

Table 15. Sample nighttime species densities (cm^{-3}).[a(b) indicates $a \times 10^b$] (from Reference 54).

SPECIES	ALTITUDE							
	150	200	250	300	350	400	450	500
O	2.3 (10)	4.6 (9)	1.3 (9)	4.2 (8)	1.4 (8)	4.8 (7)	1.7 (7)	6.1 (6)
N_2	2.3 (10)	1.7 (10)	1.9 (8)	2.7 (7)	3.9 (6)	6.2 (5)	1.0 (5)	1.7 (4)
O_2	2.4 (9)	1.2 (8)	1.1 (7)	1.1 (6)	1.3 (5)	1.5 (4)	1.8 (3)	2.4 (2)
e^-	5. (2)	5. (3)	7. (4)	1. (5)	8. (4)	5. (4)	3. (4)	2. (4)
O^+	7. (-1)	1. (3)	7. (4)	1. (5)	7. (4)	3. (4)	1. (4)	5. (3)
NO^+	1. (2)	1. (3)	3. (2)	5. (1)	6. (0)	6. (-1)	6. (-3)	7. (-3)
O_2^+	4. (2)	3. (3)	1. (3)	1. (2)	1. (1)	1. (0)	8. (-2)	8. (-3)
O^-	3. (-3)	3. (-2)	4. (-1)	5. (-1)	4. (-1)	2. (-1)	1. (-1)	8. (-2)

$$[O_2^+] \simeq 1.2\times10^{-4}\ [O_2] \times [O^+]/[e] \tag{7-1}$$

$$[NO^+] \simeq 1.7\times10^{-6}[N_2] \times [O^+]/[e] \tag{7-2}$$

and

$$[O^-] \simeq \frac{1.3\times10^{-15}\ [O]\ [e]}{2\times10^{-10}\ [O] + 1.7\times10^{-7}\ [O^+]} \quad . \tag{7-3}$$

Above the peak of the F-layer, the steady state condition as well as the assumption of no flow of constituents will probably become increasingly less reliable. Hence, these methods cannot be used to provide information above 500 km, although, in principle, it is possible to include such effects in finding a dynamical relation between the various densities and rate coefficients.

The species densities can now be used to provide volume emission rates if it is assumed that the populations of the various levels are in a steady state. In this case, the rate of emission is equal to the rate of population of the levels. The emission rates in photons/cm^3-sec are thus:

$$E_{1356} = \alpha_{1356} [O^+] [e] + 0.53 \gamma_7 [O^+] [O^-] \tag{7-4}$$

$$E_{7774} = \alpha_{7774} [O^+] [e] + 0.42 \gamma_7 [O^+] [O^-] \tag{7-5}$$

$$E_{6300} = 0.12 \gamma_7 [O^+] [O^-] + (k_S + k_D) \gamma_1 [O_2^+] [e]$$

$$+ 1 \times \gamma_2 [NO^+] [e] \tag{7-6}$$

$$E_{5577} = k_S \times \gamma_1 [O_2^+] [e] . \tag{7-7}$$

(Here the α_x is the coefficient for x Å emission from radiative recombination, and the γ_j are the rate coefficients for reaction j in Table 12.) These are given as functions of altitude in Figure 22.

If the atmospheric and ionospheric densities are changed, the emission rates will change accordingly. At a steady state

$$E_{5577} \propto [O_2] [O^+] \tag{7-8}$$

and

$$E_{6300} \propto [O_2] [O^+] \{ 1 + c [N_2]/[O_2] \} \quad . \tag{7-9}$$

When O^+ is the dominant ion (near the peak of the F-layer), these two emissions are proportional to the electron density. The radiative recombination contributions to 1356Å and 7774Å give

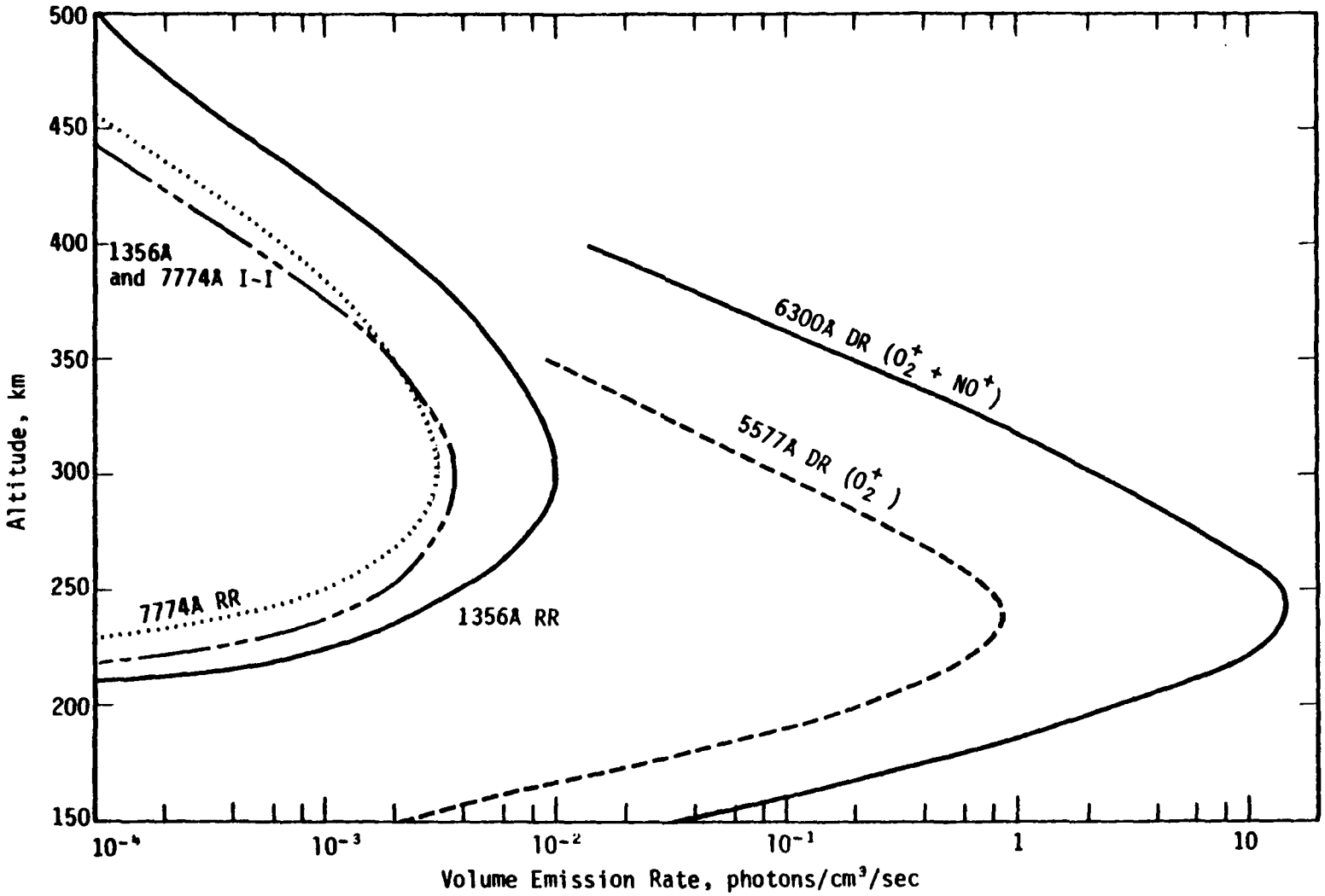

Figure 22. Volume emission rates of several OI lines from dissociative recombination (DR), radiative recombination (RR) and ion-ion recombination (I-I) for typical F-region parameters given in Table 13. (Quenching of 6300A has been ignored and this becomes a serious omission below 200 km.)

$$E_{RR} \propto [e]\,[O^+] \quad . \tag{7-10}$$

This is approximately proportional to the square of the electron density so that emissions are greatly enhanced by a strong F-region. The example given in Figure 8 of a nighttime density of 10^5 cm^{-3} is common and represents a case in which sensing techniques should be able to operate.

7.4 EMISSION INTENSITIES REQUIRED FOR OBSERVATION

In an optically thin volume emitter, the intensity of radiation in photons/cm^2-sec received in a detector of small solid angle $\Delta\Omega$ is

$$I = \frac{\Delta\Omega}{4\pi} \int_0^\infty E(\ell)d\ell \tag{7-11}$$

where E is the volume emission rate and ℓ is the distance from the detector along the axis. This assumes that the source uniformly fills the field of view. The column emission rate

$$J \equiv \int_0^\infty E(\ell)d\ell \tag{7-12}$$

is a frequently used measure of the source strength for atmospheric emissions, and it is given in units of Rayleighs (R), 10^6 photons/cm^2-sec. For the examples in Figure 21, the 6300Å emissions give ≈ 100 R, the 5577Å line gives ≈ 10R while those emissions provided by radiative recombination yield ≈ 0.1 R.

The ultimate restriction on detection of atmospheric emissions is the presence of sufficiently large numbers of photons for adequate statistics. This means for any given source, for a 10 percent level of

statistical uncertainty, at least 100 photons are needed in the sampling interval, Δt. Thus, this confidence level requires

$$100 < J \cdot \frac{\Delta\Omega}{4\pi} \cdot \Delta t \cdot A \qquad (7\text{-}13)$$

where A is the effective area of the detector. This means that there is an inverse relationship between source strength and spatial or temporal resolution. As an example, the Atmosphere Explorer-C had a sensor with a field of view of a 3° half angle cone ($\Delta\Omega = 8.6\times10^{-3}$ sr), a detector of 0.5 cm diameter ($A = 0.2$ cm^2), and a sample time of $\Delta t = 128$ msec.[62] Therefore, $J > 5.7$ Rayleighs would be required for a ± 10 percent level of uncertainty.

In the case of a detector which is mounted on a satellite and continuously viewing earthward, both field of view and sample time might be increased substantially over the above example if the horizontal variation of the source is not too great. Consider a satellite at 1000 km circular orbit (period = 105 min) with a detector field of view of 500×500 km at F-region heights ($\Delta\Omega \approx 0.5$ sr). A sample interval might be such that the subsatellite point moves by less than 500 km, say 100 km. Then, $\Delta t \approx 10$ sec will maintain the spatial resolution. For $A = 0.2$cm^2, the minimum column emission rate which can be detected to a 10 percent level will be $\approx 10^{-3}$ Rayleighs. The two examples given serve to illustrate the intensity required for detection and resolution of atmospheric emissions for a line of sight which is vertical. As we shall see in a later section, the use of a limb mode can increase the intensities substantially.

7.5 USING EMISSIONS TO FIND PEAK ELECTRON DENSITY AND HEIGHT

Chandra et al.[59] as well as Tinsley and Bittencourt[60] have demonstrated that observations of both 1356Å and 6300Å emissions during nighttime at latitudes below the auroral oval can be used to establish the

peak electron density of the F-layer and height of that peak if a shape for the profile is given. Here, we will outline the formalism used in Reference 60 although that in Reference 59 is essentially the same.

For a vertical viewing direction, let us take the electron density profile to be $n_m S(z)$ where n_m is the peak electron density at $z = h_m$. Then $S(h_m) \equiv 1$. The column emission rate of the 1356Å line is then given by

$$J_{1356} = n_m^2 \int \alpha_{1356}\, S(z)dz + n_m^2 \int \frac{\beta_{1356}\, \gamma_7\gamma_6\, [O]\, S^2(z)}{\gamma_8[O] + \gamma_7\, n_m\, S(z)}\, dz \quad (7\text{-}14)$$

for radiative recombination and ion-ion recombination when $n_e \approx [O^+]$ as is true near the F-region peak. The first term is proportional to n_m^2 while the second term is important only when it is proportional to n_m^2. That is, when $\gamma_8[O] \gg \gamma_7\, n_m\, S(z)$, the second integrand is independent of n_m while in the opposite limit the second integral is small compared to the first. As a result J_{1356} is very nearly proportional to n_m^2 and very nearly independent of any other species densities. Therefore, observations of J_{1356} give n_m when the profile $S(z)$ is assumed.

The column emission rate for the 6300Å line is almost exclusively from dissociative recombination of O_2^+ and NO^+. The ^1D state of OI is quenched by collisions in the lower F-region. The quenching rate is taken as

$$q(z) = S_{N_2}\, [N_2] + S_e\, [e] \quad (7\text{-}15)$$

from N_2 and electron collisions where $S_{N_2} = 7\times10^{-11} cm^3/sec$ and $S_e = 1.7\times10^{-9}\ cm^3/sec$. If q is comparable with the inverse of the lifetime of the ^1D state (τ = 110 sec), then deexcitation of these states is important. The density of O^+ can be related to [e] in a steady state giving

$$[O^+] = \frac{[e]}{1 + B(z)} \tag{7-16}$$

where

$$B(z) = \frac{\gamma_3}{\gamma_1}\frac{[O_2]}{[e]} + \frac{\gamma_4}{\gamma_2}\frac{[N_2]}{[e]} \tag{7-17}$$

Therefore, the 6300Å emission rate is

$$J_{6300} = f_1(k_S+k_D)\ n_m \int \frac{\gamma_3\ [O_2]\ S(z)\ [1+ c\ [N_2]/[O_2]]}{[1+B(z)]\ [1+q(z)\cdot\tau]}\, dz \tag{7-18}$$

where

$$c = \frac{\gamma_4}{(k_S+k_D)\gamma_3} \approx 0.03 \quad , \tag{7-19}$$

and $f_1 = 0.76$ is the fraction of ^1D decays which lead to the 6300Å line. J_{6300} is thus nearly proportional to n_m multiplied by a function of the height of the profile peak due to the appearance of $[O_2]$ in the integrand. Therefore, the ratio $J_{6300}/(J_{1356})^{1/2}$ is chiefly a function of h_m while $(J_{1356})^{1/2}$ is chiefly a function of n_m.

Using this method Chandra et al.[59] have made direct comparisons with other data on electron density profiles, and, to a substantial extent, they are in agreement. However, there are several sources of uncertainty in this approach including the choice of atmospheric models, departure from the assumed Chapman profile, and the accuracy of the chemical rate constants involved. In spite of these problems, it should be possible to find useful information on subsatellite electron density profiles at night below the auroral oval, especially if other instruments are used for calibration. Such analyses are not presently carried out on a routine basis.

7.6 SCANNING PHOTOMETERS TO FIX ELECTRON DENSITY PROFILES

Thomas and Donahue[63] have used the vast quantities of data gathered by an orbiting scanning photometer to deduce electron density profiles at night, below the auroral oval, by a deconvolution of many scans of the same region from different positions. Using this method, they were able to find the volume emission rates in the plane of the orbit of the OGO-6 satellite. This was translated into electron densities in the plane of the orbit by methods which will now be detailed.

Emission of the OI 5577Å line at night at latitudes below the auroral oval results almost exclusively from production of the ^1S state of atomic oxygen by dissociative recombination of O_2^+ and electrons. The volume emission rate in a steady state is

$$E_{5577} = f_2 k_S \gamma_3 \, [O_2] \, [O^+] \tag{7-20}$$

so the column emission rate will be

$$J_{5577} = f_2 k_S \int \gamma_3 \, [O_2] \, [O^+] \, d\ell \tag{7-21}$$

where the integral over ℓ is along the line of sight of the detector, and $f_2 = 0.94$ is the fraction of ^1S decays which yield the 5577Å line. Note that no correction for quenching of the ^1S state is needed due to its short lifetime of 0.74 seconds. Figure 22 indicates that 5577Å emissions are small below 150 kilometers. However, at about 100 kilometers another excitation mechanism becomes available to oxygen giving rise to volume emission rates at least comparable to those peak values in Figure 22. This alternate excitation mechanism does not directly relate to electron density, so it is of no interest here. This means that, for a sight path

which goes through 100 km the column emission rate may be swamped by this additional source. This will make it very difficult to deduce information about electron densities at higher altitudes. Therefore, observation of 5577Å emissions will be most useful if the line of sight does not extend down to the E-region of the ionosphere. It should be noted that 5577Å observations, just as for those at 6300Å, give information about $[O^+]$ rather than $[e]$, so one must either assume that $[O^+] \approx [e]$ or provide a relation between the two as was done by Equation 7-16. This result then gives

$$J_{5577} = f_2 k_S \int \frac{\gamma_3 [O_2] [e] \, d\ell}{1 + B(\ell)} \tag{7-22}$$

The OGO-6 satellite used a scanning photometer to view the 5577Å airglow in the plane of its polar orbit (apogee 1100 km, perigee 400 km). The scan ranged from 10° to 25° below the horizontal plane and was carried out in 18.32 seconds. The field of view was 4.2° horizontally but only 7.5 minutes of arc in the vertical direction of the scan. Each 18 second scan consisted of 127 positions separated by 7.5 minutes of arc. Therefore, for a satellite altitude of 500 km, the field of view at 250 km is about 85 km × 2.5 km midway through the scan. (This gives the absolute upper bound on the possible resolution of volume emission rates, although we will shortly see that the practical resolution is less.) This corresponds to a solid angle of $\Delta\Omega = 1.6 \times 10^{-4}$ sr and a sample time of Δt = 0.145 sec. The emitting region is scanned about 25 times from different positions during a single pass across the subauroral zone. Thus, a total of about 3000 data points are taken during a single pass. Thomas and Donahue divided the emitting region into areas 2 km in altitude by 0.5° magnetic latitude (~58 km) horizontally in the orbital plane and attempted to find the volume emission rate in the resulting 14,600 cells. (The region of interest was about 200 to 400 km in altitude and ± 25° in magnetic latitude.) Volume emission rates in the cells were estimated by beginning at the highest altitudes giving detectable emissions to fix the

rates in the upper cells. Lower scans then were used sequentially to establish the rates in lower altitude cells. The resulting emission matrix was smoothed and repeatedly rescaled to obtain agreement with the measured intensities. The resulting matrix is not unique since 3,000 data points are used to define 14,600 volume emission rates. Still, the results were found to agree with measurements to within 10 percent, and it appears that the main features of the emission contours (which are large compared to cell size) do not depend upon the details of the reduction procedure.

This technique was used to find an electron density profile which could be compared with that obtained by ground based radar soundings. The results indicate that while the shapes found by each technique are quite similar, the amplitudes differ by about a factor of two. Thomas and Donahue produced a fit by altering the coefficient of Equation 7-22 and suggesting that the rate coefficient, γ_3, for $O^+ + O_2 \rightarrow O_2^+ + O$ should be reduced by a factor of about two. However, it is not clear whether γ_3, k_S, or $[O_2]$ uncertainties are most important in producing the difference between the two experimental techniques for finding the electron density profile. Nevertheless, it is very encouraging that, given some calibration for the product $\gamma_3 k_S [O_2]$ by separate methods, the electron density profile in the orbital plane can be established to within a factor of two provided that the intensity of the emission, or equivalently the electron density, is sufficiently great. The parameters for the OGO-6 experiment made observations of $[e]$ of less than 10^5 cm^{-3} above 300 km difficult while values as low as 10^4 below 250 km are possible although difficult. As a result, the OGO-6 airglow measurements are best for large electron densities and a low F-region peak. A modification in experimental parameters would be required if the full range of nighttime subauroral ionospheres were to be mapped. Donahue[64] has suggested that a scanning photometer should be a standard part of experimental satellites, but the recommendation has not been carried out. No current or planned and published experiments along these lines now exist.

7.7 AN ALTERNATE SCANNING METHOD

A sensor with a limited field of view on a spinning satellite will scan an angular profile in the course of a revolution. Generally, it is not possible to relate the angular variation of radiance directly to volume emission rates. However, if the emission is from a spherically stratified layer, the inversion is possible.[62] For a column emission rate of

$$J(r_t) = 2\times10^{-6} \int_{r_0 \sin z_0}^{\infty} \frac{r\,E(r)dr}{(r_0^2 - r^2 \sin^2 z_0)^{1/2}}, \qquad (7\text{-}23)$$

where $r_t = r_0 \sin z_0$ is the tangent ray height for the sensor at radius r_0 with viewing zenith angle z_0, the volume emission rate can be solved for as

$$E(r) = \frac{10^6}{\pi} \frac{d}{dr} \int_r^{\infty} \frac{r_t\, J(r_t)\, dr_t}{r(r_t^2 - r^2)^{1/2}} \quad . \qquad (7\text{-}24)$$

Therefore, given spherical stratification in the viewing plane, the volume emission rate can be deduced. This requires use of a set of measurements of the column emission rates, J, with sufficient accuracy and resolution to allow the inversion in Equation 7-24 to be carried out. Generally, any experiment of this nature will have to be designed to take into account required resolution, spin rates, and likely levels of horizontal gradients in order to be useful. The existence of such horizontal gradients will introduce errors into the spin scan method, but, with a sufficiently large number of scans, it may be possible to correct results to provide adequate emission profiles. Of course, once emission profiles are known, it is possible to convert them into electron density profiles using atmospheric chemistry to find the rate of population of those excited states whose emissions are being observed.

7.8 PROSPECTS FOR FINDING ELECTRON DENSITY PROFILES BY CHEMILUMINESCENCE

Past experiments indicate that measurements of nighttime airglow in the subauroral region can be used to find electron density profiles. Presently, no satellites exist which have suitable instrumentation for this purpose but there is nothing particularly unusual or difficult about the required sensors. We will now describe features of instruments which would be suitable for this task.

7.8.1 Inversion Using Limb Scanning Photometers in Orbital Plane

In order to hope to recover an adequately resolved set of volume emission rates from a series of column emission rate measurements, it is necessary to have a sufficiently small field of view to resolve features comparable in size to those of electron density variations. This typically means vertical resolution of ≈ 10 km and horizontal resolution of ≈ 200 km. The sample time must be long enough to provide good statistics (say, better than ± 10%) but short enough that the satellite moves a distance less than the required horizontal resolution. In the case of 5577Å emissions, limb column emission rates of as low as J ≈ 10 Rayleighs are available at times when the electron densities are below 10^5 cm^{-3}. If the orbital radius of the satellite is too great, resolution can be gained only by a small angular field of view so it is best if an orbit near the F-region peak is used. Using a circular orbit at 500 km in conjunction with the indicated field of view and a sensor area of A = 1 cm^2, the available column emission rate will force a minimum sample time of 1/4 second for features 2000 km away. (This distance is approximately that from a 500 km high satellite to a point at 250 km altitude along a line tangent to a spherical shell passing through this point.) Significant emissions are expected from altitudes of 500 to 100 km so that (500-100)/10 = 40 sample intervals will be needed to scan the limb. This will

require ten seconds. In ten seconds, this satellite will move ≈ 80 km which is less than the required horizontal resolution. Furthermore, ionospheric changes generally occur on scales of many minutes. Therefore, 10 seconds is an acceptable interval. Such a scanning photometer will obtain a statistically significant number of counts for limb column emissions from about 150 to 450 km for both the 5577Å and 6300Å lines. Other lines emitted from this region will not be of sufficient intensity to provide useful data.

In order to find electron density profiles, it is first necessary to unfold column emission rates to give volume emission rates. This is most easily done in the orbit plane if all scans occur in this plane. As shown by Thomas and Donahue[63], multiple scans through the same region from different satellite positions can be used to deconvolve the volume rates from column rates and thus give the volume emission rates in the orbital plane. Our example of 10 seconds for each scan of 40 altitudes will give 23,000 data values per orbit. With this data, we could hope to determine up to 23,000 volume emission rates in the plane of the orbit. This corresponds to cells 10 km in altitude by about 80 km in horizontal dimension, which is consistent with the resolution required for many ionospheric structures.

Such an inversion is essentially that used by Thomas and Donahue so that there is no doubt that this is a practical method of analysis. In order to convert volume emission rates to electron densities, it is necessary to apply dissociative recombination chemistry to relate electron density to population rate of those states which decay by emitting the 5577Å and 6300Å radiation. This relation involves partial rate coefficients and the density of O_2. Both of these are subject to systematic uncertainties which could be resolved by constraining the solutions for electron densities by use of additional data from other sources such as radio frequency sounders. Once the normalization is fixed, the conversion

of volume emission rates to electron density could be continued with confidence.

7.8.2 Limb Scanning Outside the Orbital Plane

Column emission rates for limb scans can be found for any azimuth, not just in the orbital plane. However, it is apparent that a very large number of such scans will be required if volume emission rates over the ionospheric regions visible to a satellite are to be found. It would be necessary to have many sight paths through all those regions where the emission rates are desired. This is quite impractical for those distant points at the edge of the visible region perhaps 3000 km away from the orbital plane. However, if scans are made near the plane, the region of deduced volume rates may be expanded due to the continuity of atmospheric parameters. Since the scale for horizontal variation is ≈ 200 km, it is expected that the emission rates in a second plane parallel to and about 200 km from the orbital plane can be found if a second series of scans are carried out at an azimuth near the orbital direction. A suitable azimuth would be $\theta \approx 200$ km/2000 km = 0.1 radians. A sequence of such scans at increasing azimuth angles will allow the addition of one plane removed another 200 km for each azimuth used. Using such an approach would allow the volume emission rate in a swath parallel to the satellite track to be found. Obviously, the data handling and processing would be cumbersome for a large number of azimuths, but it should be straightforward. Since the parameters originally chosen for a scanning photometer were based on continuous operation, it would be necessary to have a number of sensors equal to the number of desired azimuthal positions unless the characteristics were significantly changed.

A second approach to finding volume emission rates outside the orbital plane can be used if horizontal gradients over the sampled region are small. In this case, as shown in Section 7.7, a single series of limb

scans of column emission rates can be easily inverted to give volume emission rates (which are, by assumption, functions of altitude only). The requirements of small horizontal gradients is difficult to satisfy for a satellite in 500 km orbit scanning ionospheric heights. In this case, a typical path has a horizontal extent of ≈ 1000 km along which contributions are significant. However, as indicated earlier, the likely horizontal scale of structure is perhaps 200 km. As a result, routine measurements of this sort are not likely to provide an accurate measure of the distant volume emission rates. Still, an estimate of the average emission rates over the sampled region can be obtained. In conjunction with other measurements, this may be applied to finding an estimate of the electron density profile at points up to 2000 km from the satellite. Of course, the conversion φ volume emission rates to electron density has the same uncertainty associated with chemistry rate coefficients and neutral densities as does the case for measurements in the orbital plane.

7.8.3 Electron Densities Beneath the Satellite

As discussed in Section 7.5, a single observation of 6300Å and 1356Å (or 7774Å) emissions can be used to provide the maximum electron density and its height beneath the satellite if the shape of the profile is known. The column emission rate from the 1356Å line is as low as ≈ 0.1R for observation directly toward the earth. If a horizontal field of view of 50 km × 50 km is used, then a solid angle of $\Delta\Omega \approx (50/250)^2 = 4\times10^{-2}$ sr will provide adequate resolution. An effective sensor area of 1 cm^2 will then prove adequate statistics for a sample time of less than one second. The 6300Å line is sufficiently intense that the detector just suggested will easily be adequate.

The required assumption of profile shape is quite a strong limitation and a source of uncertainty. However, if this method were used in conjunction with a photometer scanning in the orbital plane, the two

methods would provide complementary information. It is expected that the scanning photometer would provide a reasonably accurate shape for the profile while the uncertainties of the method would be largely confined to the overall normalization. This normalization could be supplied by the earthward looking sensor just described through observation of 6300Å and 1356Å radiations.

7.9 SUMMARY

Observations of nighttime subauroral airglow of OI at 5577Å, 6300Å and 1356Å can be used to provide routine estimates of electron density profiles along and near the orbital plane of a satellite. The required instrumentation is quite conventional. A limb scanning photometer, operating at 5577Å and 6300Å, with a narrow field of view gives a series of column emission rates which can be inverted to provide volume emission rates. These volume emission rates can be converted to electron densities by a knowledge of the dissociative recombination rate coefficients which serve to populate the states of atomic oxygen which decay to give the emissions. This conversion to electron density is uncertain to within a factor of ~2 but if additional measurements are available, such as from ionosondes, the conversion could be calibrated.

These limb scans are most useful in the plane of the orbit since multiple samples of all regions are then possible. However, additional scans at angles somewhat off the orbit can provide the electron densities along strips parallel to the orbit once the orbital plane has been filled in. The continuity of electron densities allows the information from these scans outside the plane to be used to continue the density estimates beyond the plane. A strip several hundred kilometers across will be accessible to practical measurement in this manner.

The scanning method can be augmented by a fixed sensor which is pointed earthward and which samples emissions at 6300Å and 1356Å. This data can be used to provide the height and electron density at the F-region peak if the shape of the profile is known. It is expected that the scanning method will provide this shape.

Satellite observation of airglow from atomic oxygen could routinely provide electron densities over a significant portion of the globe. While this is applicable only at night in the subauroral region, the same observations can be used to provide volume emission rates without any geographical restriction. Since the volume emission rates are worthwhile by themselves, such an experiment should be of interest to a wide community of atmospheric research.

SECTION 8
IN SITU METHODS

Instead of positioning a satellite far above most of the ionosphere, it is possible to have the satellite fly through the peak of the F-layer or even somewhat below the peak. Satellites will remain in a 200 km high circular orbit for a significant period before falling to earth and have a many year lifetime at 300 km. This latter height is close to the peak of the F-layer. Flying directly through that portion of the ionosphere of greatest interest permits direct and detailed measurements of many ionospheric parameters. Not only can electron density be measured to substantial accuracy, but also ion density and composition, plasma motion, electron and ion temperatures, and magnetic field variations. Table 4 lists the in situ capabilities of the ISIS satellites. These fly well above the peak of the F-layer but still within sufficient plasma for in situ measurements to be made. The Atmospheric Explorer satellites fly much closer to the peak of the F-layer and have a variety of in situ capabilities. Figure 23 shows a sample of results from one experiment on board Atmospheric Explorer-E. This particular record shows a bite-out in ion density occurring as the satellite passes the dip equator. Such bite-outs provided the first conclusive proof that bubbles exist in the equatorial ionosphere[11].

The major drawback to in situ measurements is that they are only obtained along the satellite orbit. To obtain anything approaching a three-dimensional view requires many satellites. From a cost standpoint alone, this is not feasible. In situ measurements are valuable when remote techniques are inadequate, when high accuracy is required, or when they are part of a larger ionospheric spacecraft such as ISIS.

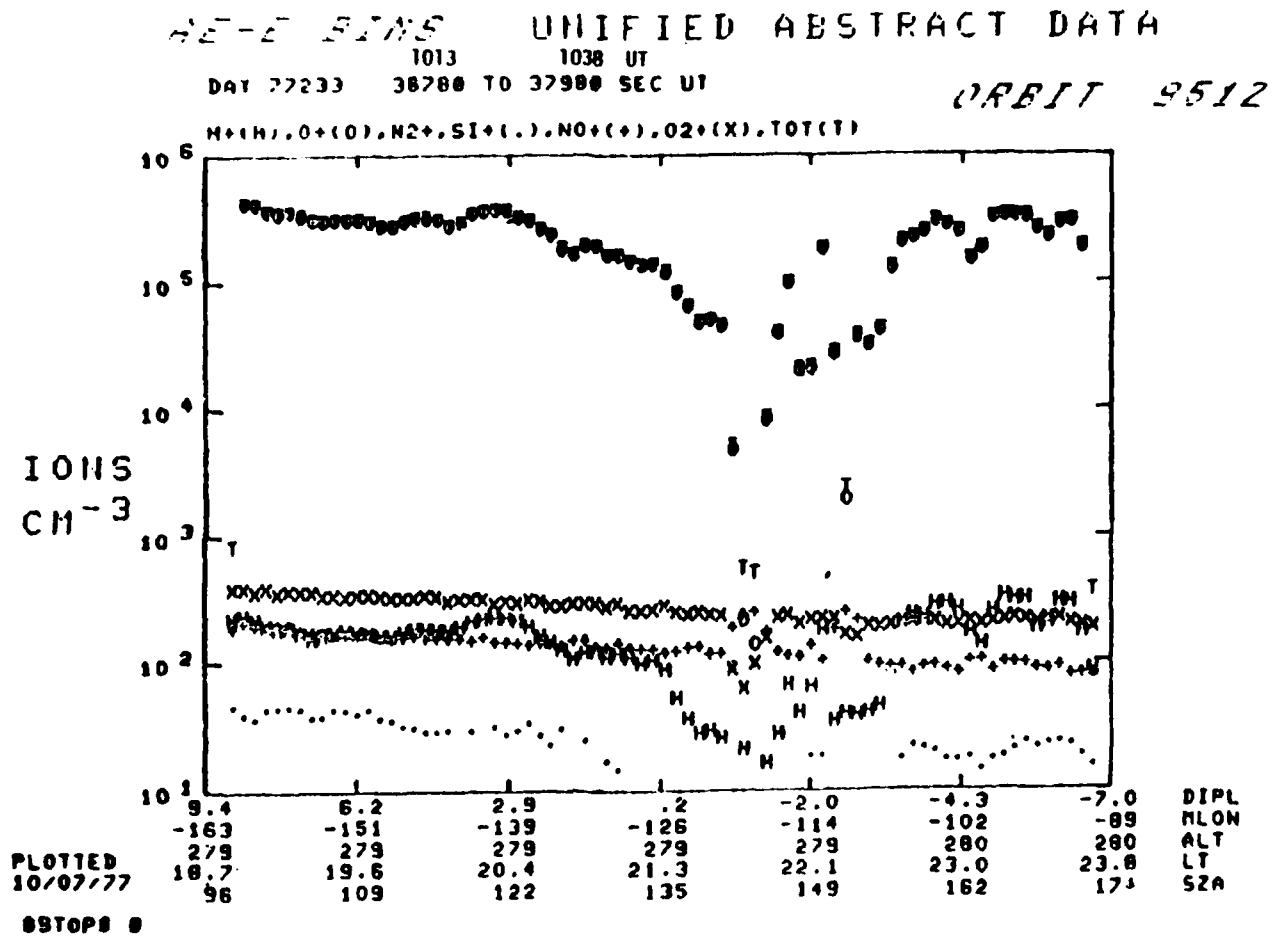

Figure 23. Atmospheric Explorer--E data (from Reference 65).

SECTION 9
BREMSSTRAHLUNG METHODS

In recent years, it has become possible to measure the low energy x-ray flux caused by electrons precipitating into the atmosphere.[65-70] In some cases, it has been possible to relate this "bremsstrahlung" to measurements of the precipitating electron flux, as well as to optical observations of bright auroral arcs.[66,67,69] Such observations are of interest here because the precipitating electron flux is, under some circumstances, a significant source of ionization in the ionosphere. Hence, it is hoped that by measuring the bremsstrahlung in a particular area, it will be possible to compute the precipitating electron flux, which in turn can be used to compute the ionospheric electron density. This chapter addresses the calculation of electron flux and leaves the calculation of electron density to others.[71,72]

Figure 24 shows the observed relationship between bright auroral arcs, bremsstrahlung, and precipitating electron flux. Because of this strong correlation, it is also anticipated that a similar correlation exists between the diffuse aurora, bremsstrahlung, and precipitating electron flux. Diffuse aurora are of greater interest to this study because they cover a much larger area of the high latitude regions than do the bright arcs and, therefore, may be important to a larger region of the ionosphere. Diffuse aurora involve lower electron fluxes and lower electron energies than do the bright arcs.

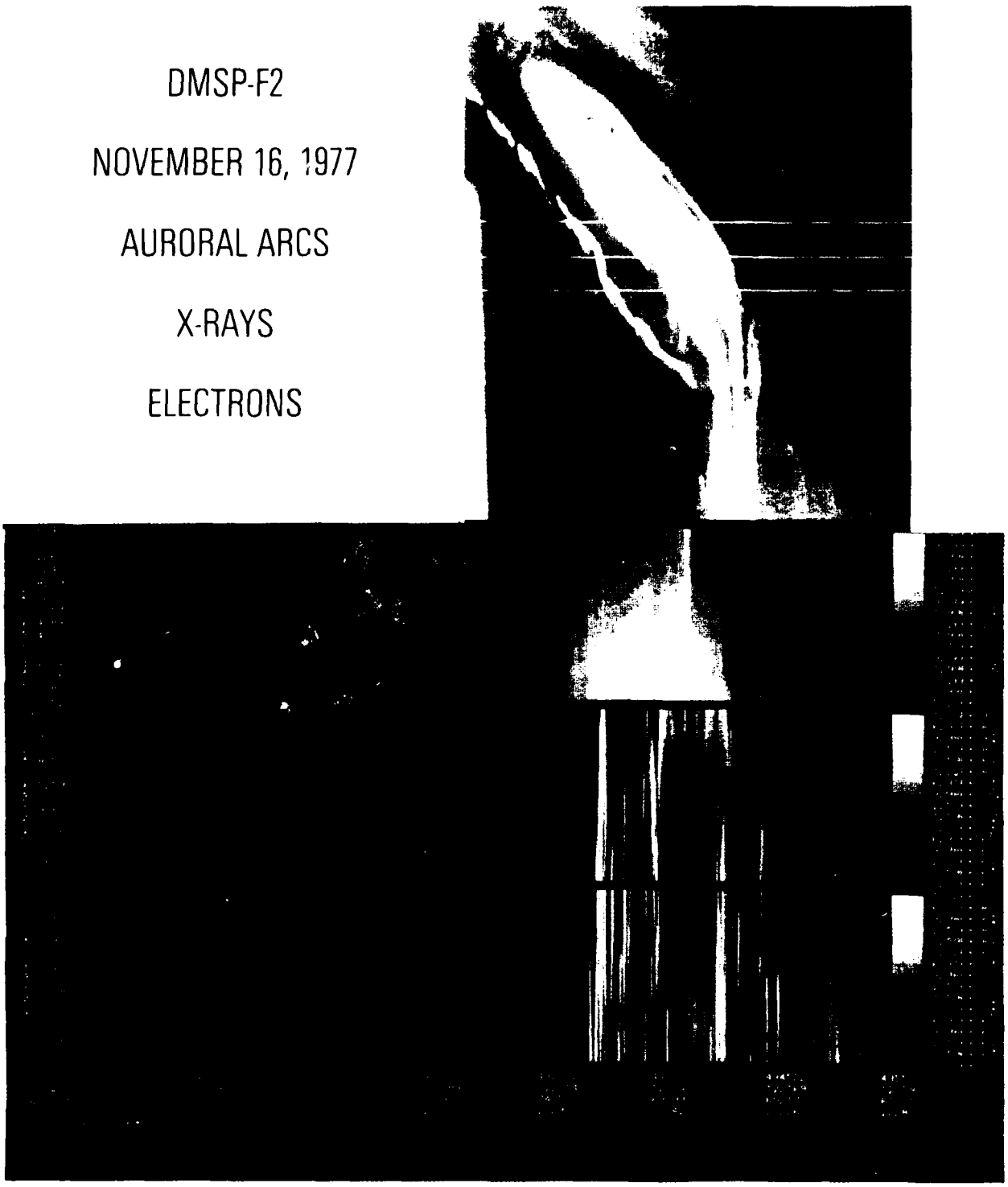

Figure 24. Simultaneous DMSP observations of bremsstrahlung x-rays, auroral arcs, and precipitating electrons. The lower charts show a cross section through the auroral arc at the top (from Reference 3).

9.1 BACKGROUND ASSUMPTIONS

In the following discussion, we consider the problem of determining both the primary flux and spectral energy distribution of precipitating electrons, on the basis of satellite measurements of bremsstrahlung produced by the electrons in the atmosphere.

The problem may be outlined as follows. Electrons precipitating into the atmosphere over a broad area can be characterized by a function s(T), electrons/(m^2 sec keV), the number of electrons per unit area per second per unit energy having the kinetic energy, T, which enter the top "surface" of the atmosphere. This is the spectral flux, assumed isotropic,integrated over all directions in the downward directed hemisphere. This electron flux produces an upward directed photon flux spectrum f(k) photons/(m^2 sec keV) at the top of the atmosphere, where k is the photon energy, and f(k) is the integral over all angles in the upward directed hemisphere. A satellite mounted detector, essentially outside the atmosphere, and sensitive to all photons entering from the lower hemisphere would measure this flux. Broad area precipitation and planar geometry of the atmosphere are assumed.

The relation between the two flux spectra can be expressed as an integral,

$$f(k) = \int_k^\infty \phi(k,T)s(T)dT \quad , \tag{9-1}$$

where all the complex physics of electron scattering, bremsstrahlung production, scattering and absorption of bremsstrahlung photons, etc., is contained in the kernel $\phi(k,T)$.[74] Using a Monte Carlo method, Reference 74 has calculated $\phi(k,T)$ for the conditions assumed above in the energy ranges, 10 keV $\leq$ k $\leq$ 1500 keV, 15 $\leq$ T $\leq$ 2000 keV. The behavior of this

function is shown in Figure 25. Since photons are only of equal or lesser energy than the electron which produces them, $\phi(k,T)$ vanishes when $T<k$. For this reason, the plot uses T-k as an abscissa. Further, the extrapolation of all curves given in Figure 25 must pass through the origin on this plot. The special feature that the photon flux at energy k is produced entirely by the part of the electron flux at energies greater than k has important consequences for the estimation of electron fluxes from photon flux measurements. The curves of Figure 25 do not extend to low enough energies in either k or T to be of maximum utility for diffuse aurora. Also at low energies (0.4 - 3.0 keV), the photon spectrum contains, in addition to bremsstrahlung, the K_α x-rays of nitrogen, oxygen, and argon. Calculations of auroral bremsstrahlung and x-ray emission at photon energies of 0.1 to 10 keV have been performed.[75,76] These papers calculate the photon spectrum resulting from assumed electron spectra, not the more general kernel $\phi(k,T)$ of Reference 74, but the methods described are equally useful to calculate the kernel for low values of k and T. Therefore, in principle, the kernel incorporating the physics of the process is known or computable. Although specification of the kernel at low energies would require new calculations to be made, we assume, for discussion, that the kernel is known. The essential difficulties in the remote sensing problem lie elsewhere.

9.2 THE INVERSION PROBLEM

In common with many problems of remote sensing, the estimation of spectral electron flux from photon measurements can be cast in the form of a Fredholm integral equation of the first kind. This is the form of Equation 9-1 if f, and ϕ are assumed known analytic functions and s is the unknown function to be determined. Except in restrictive and rather special conditions, which fortunately include the conventional integral transforms (Fourier, Laplace, Mellin, etc.,), a unique solution may not exist. Moreover, in the remote sensing problem, the function f(k) is only

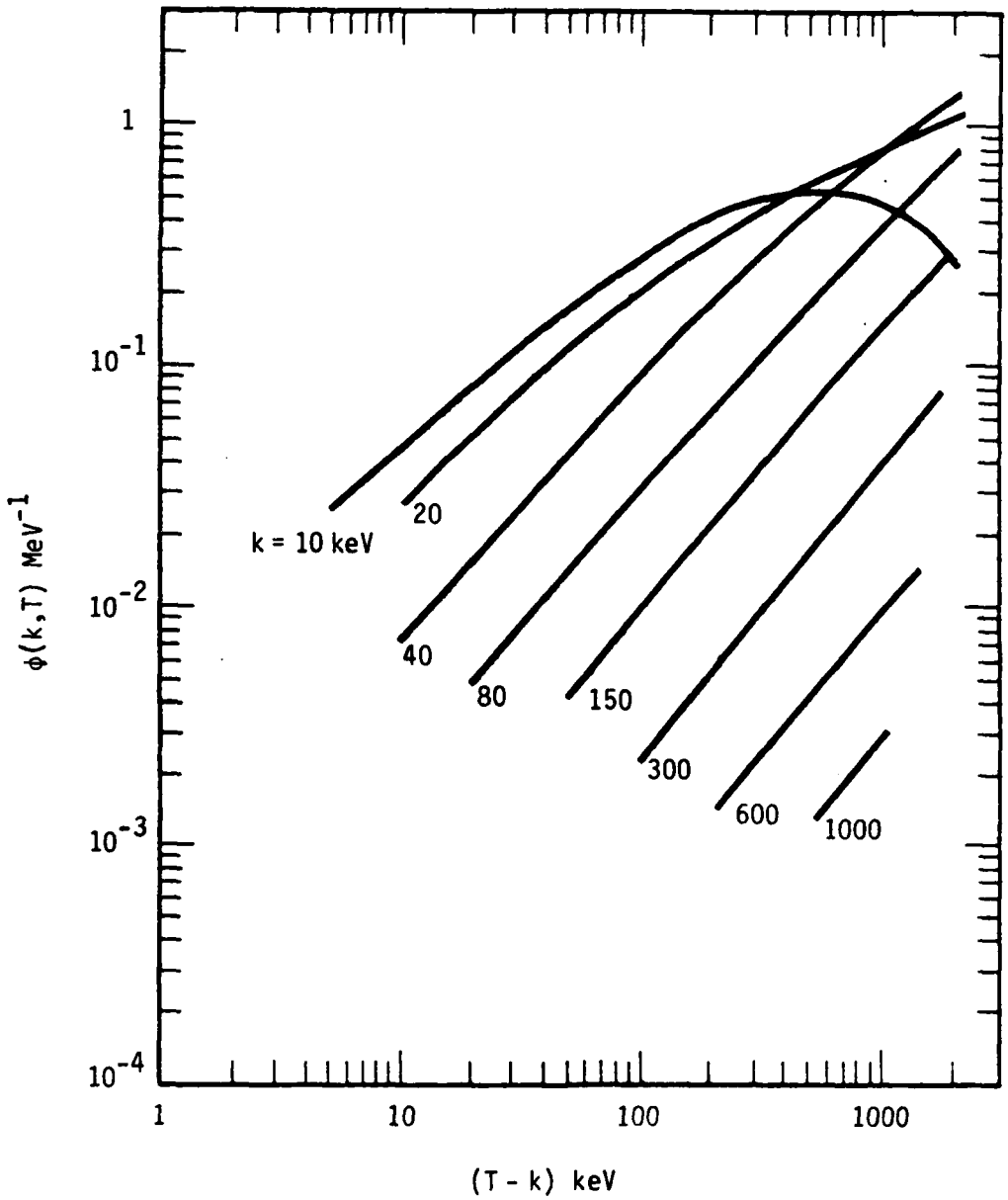

Figure 25. Kernel of bremsstrahlung production.

known at a finite number of energies k, within a certain measurement error. In these circumstances the numerical inversion of the integral of Equation 9-1 is an ill-posed problem. Many functions s(T) containing more and more rapid oscillations and/or discontinuities will satisfy the equation for a given finite set of f's. These features, and several approaches to the general inversion problem, are discussed in Reference 77. Successful inversion methods all impose additional conditions upon s(T) other than its ability to produce agreement with the observations. These additional conditions may be in the form of smoothness and boundedness requirements, membership of the function s(T) in a certain class of functions, or incorporation of theoretical prior knowledge of the form of s(T).

We discuss three inversion procedures. A finite difference or quadrature approximation and a variation of parameters formulation, which are both representative of conventional approaches, are sketched. Finally, a procedure based upon the maximum entropy formalism is examined. This latter procedure is recommended for the problem.

9.2.1 Quadrature Approximation

This method consists of approximating the integral equation (Equation 9-1), by its discrete analog, a matrix multiplication

$$f(k_i) = \sum_{j=1}^{m} \phi(k_i, T_j)\, s(T_j)\, w_j \qquad i=1,\ldots,n \tag{9-2}$$

or,

$$f_i = \sum_{j \geq i}^{m} M_{ij} s_j \tag{9-3}$$

where the measurements are the n values of f_i observed at energies k_i. The quadrature enters in the determination of the weights w_j for the

matrix elements $M_{ij} = \phi(k_i T_j)\, w_j$, and the function $s(T_j)$ will be determined at a finite number of points T_j ; $j=1,\ldots,n$; $m \leq n$. To achieve maximum definition of the unknown function $s(T)$, take $m=n$, its maximum value. Further, let the indices i and j run over the same set of energies, i.e., $k_i = T_j$ when $i=j$. The matrix M_{ij} is then triangular, since elements with $i>j$, or $k_i > T_j$, are zero. Depending upon the quadrature or weight function one wishes to adopt, the diagonal elements of the matrix can be made either zero or non-zero. In the latter case, the matrix can have an inverse and n values of s_j, $j=1,\ldots,n$ can be determined. When the diagonal elements are zero the matrix strictly does not have an inverse, but one may still formally calculate n-1 values of s_j, $j=1,\ldots,n-1$. In either case, the triangular structure of the matrix permits sequential calculation of the s_j, starting at the largest j value. Assume diagonal elements are non-zero; then,

$$s_m = (M_{mm})^{-1} f_m \tag{9-4}$$

$$\vdots$$

$$s_k = (M_{kk})^{-1}\left[f_k - \sum_{l=k+1}^{m} M_{kl} s_l\right] . \tag{9-5}$$

Simple and direct as this approach may be, it suffers from several disadvantages. The unknown electron flux spectrum can only be estimated at a finite number of energies equal to the energies at which bremsstrahlung measurements are made, which may imply only very coarse resolution of the spectrum. An attempt to increase the energy resolution by increasing the number of bremsstrahlung measurements increases the dimensionality of the matrix, which accentuates the effect of measurement errors upon the inversion calculation. It is evident that the sequential calculations required by the inversion algorithm rely upon an increasing number of differences between measured quantities, as the calculation proceeds. Finally, there is a large inaccuracy, and some outright arbitrariness, in the replacement of an integral by a matrix multiplication.

9.2.2 Variation of Parameters

Given a set of photon flux measurements f_i', $i=1,\ldots,n$, the variation of parameters method consists of fitting a function of m parameters, $m<n$, to achieve the best least squares fit to the measurements. For example, assume the electron flux spectrum is an exponential function,

$$s(T) = Ne^{-\alpha T} \tag{9-6}$$

of two parameters, N and α. This function, inserted into Equation 9-1, predicts a measurement at energy k_i of $f_i(N,\alpha)$ which is a function of the two parameters. The minimum of the sum,

$$F = \sum_{i=1}^{n} [f_i' - f_i(N,\alpha)]^2 \tag{9-7}$$

occurs at the parameter values which enable the chosen function to best reproduce (in a least squares sense) the observed data.

Unless the number of parameters m is equal to the number of measurements n, it is impossible in general to fit all measurements. However, there are measurement errors and if the f_i are within the measurement errors of the f_i' the calculated electron flux spectrum cannot be improved upon within the family of functions chosen. This method yields the solution s(T) most compatible with the observed measurements within the family of functions selected. Its success depends upon judicious choice of the functions to be varied, since these must have the flexibility to reflect the actual structure required in s(T). If one accepts this arbitrariness, the goodness of fit to the data can be quantified by conventional statistical measures applicable to least squares problems. However, since there are many solutions s(T) which will reproduce the observed data, goodness of fit <u>alone</u> is no justification for the validity

of the computed electron spectral flux. Unless supplemented by other knowledge (theoretical reasons) for believing the electron spectra to be exponential for example, the solution obtained depends upon the function set chosen and its validity, i.e., how likely it is to be correct, cannot be quantified.

In our judgment, the limitations of both conventional inversion methods, the quadrature approximation, and the variation of parameters, are obviated by the approach based upon the maximum entropy formalism which is described below.

9.2.3 Maximum Entropy Formalism

The important point to recognize is that the inversion problem requires the estimation of a continuous function (the electron spectral energy flux) on the basis of a finite number of measured quantities (photon fluxes at selected energies), which by the form of Equation 9-1 are special types of <u>averages</u> over the desired function. Viewed this way, the problem is identical to estimating the probability distribution of a variable, given only the expectation values of a finite number of functions of the variable. This latter problem in probability theory has a solution which is logical and rational, but not unique. Namely, the distribution with the maximum informational entropy, as defined below, which still satisfies the constraints imposed by the given expectation values, is overwhelmingly the most probable one, and the optimum inference to be made. These ideas have their roots in information theory. They were pioneered by Jaynes[78] and have been developed by him in a series of subsequent papers. Reference 79 is devoted to practical, engineering applications of this approach, and a recent review is provided by the conference report of Reference 80.

Maximum entropy methods are a formalism for the rational use of partial information. They enable problems which are ill-posed in a formal

mathematical sense, in that the given information does not determine a unique solution, to be attacked on the basis of inductive logic. The predictions (or solutions) obtained are not the deductive solution of a physics problem since the available information is insufficient. Rather the predictions are the result of a form of statistical inference, which chooses that answer which has maximum statistical weight compatible with the physics of the problem (in effect, the bremsstrahlung production kernel) and the available information (the measurements of bremsstrahlung flux).

The application of maximum entropy methods to the bremsstrahlung problem and the inversion of Equation 9-1 is a new use of the formalism which requires some special analysis. The general approach, however, is now a conventional procedure which has been applied to problems ranging from estimation of power spectra[81] to optical image reconstruction.[82] Above and in the following assertions of properties of these methods are made without proof. The requisite demonstrations can be found in the references cited.

9.3 THE ESSENTIALS OF THE MAXIMUM ENTROPY FORMALISM

Following Jaynes[78] we explain the basic idea of the method using a discrete probability distribution. Assume that a quantity x can take each of the discrete values x_i $(i=1,\ldots,N)$ with a probability p_i. In addition to the knowledge of the discrete values which x can take, there is known the expectation values of several functions $f_k(x)$, $k=1,\ldots n$, averaged over the probability distribution,

$$\bar{f}_k = \sum_i f_k(x_i)p_i \qquad k=1,\ldots n \tag{9-8}$$

Given this information, the probability distribution which is least biased, in the sense of assuming no more information than actually

given, is the distribution which maximizes the informational entropy, H, of the distribution defined as,

$$H \equiv - \sum p_i \ln p_i \tag{9-9}$$

subject to the constraints of Equation 9-8 and normalization of the probability distribution, $\sum p_i = 1$. The constrained maximization is effected by associating a Lagrange multipler with each constraint (λ_0 for normalization and μ_k for each of the expectation values) and varying the p_i. The maximum entropy probability distribution is

$$p_i = \exp[-\lambda_0 - \sum_k \mu_k f_k(x_i)] \quad . \tag{9-10}$$

The Lagrange multipliers are the parameters of the distribution. They are determined by the corresponding constraint condition. For example, λ_0 is determined by the normalization constraint, $\lambda_0 = \ln Z$, where

$$Z = \sum_i \exp[-\sum_k \mu_k f_k(x_i)] \quad .$$

This expression is recognizable as the analog of the partition function of statistical mechanics.

If an analytic form of Z is known, the additional n equations to determine the parameters μ_k are

$$\overline{f}_k = -(\partial/\partial\mu_k) \ln Z(\mu_1, \ldots, \mu_n) \quad .$$

For purposes of numerical calculation in which analytic functions are lacking, the procedure is to directly find the extremum of H.

Equation 9-10 substituted in Equation 9-9 gives H as a function of the μ_k's,

$$H(\mu_1,\ldots,\mu_n) = \ln Z(\mu_1,\ldots,\mu_n) + \sum \mu_k \bar{f}_k \quad .$$

The values of μ_k which produce an extremum of H are the correct parameters, and may be found numerically. Moreover, the function H can be proved to possess a single, unique extremum in the parameter space.

From its property of maximizing the entropy, the probability distribution obtained is the most likely distribution. It can be achieved in more ways than any other distribution compatible with the same constraints. This is the sense in which maximum entropy methods furnish the most logical inference from the information available. Whether the inferred distribution is or is not correct, is a matter of experimental measurement. The failure of direct measurements to verify a predicted distribution is an indication only that the initial information is inadequate--either the possible values $\{x_i\}$ are incorrectly chosen (essentially ignorance of the possibilities), or the functions whose average values $\bar{f}_k$ are given are not sufficiently sensitive to the distribution. In any event, the maximum entropy prediction is the best estimate possible on the basis of the information available.

Despite the resemblance between Equation 9-8 and the bremsstrahlung production Equation 9-1 there are certain differences. The one is an integral and the other is a sum. The electron flux s(T) is not a probability but, rather, more nearly a frequency (number of electrons of a certain type in the sample). The next section derives the form of maximum entropy inference needed for bremsstrahlung applications. The resemblance of this exposition to standard statistical physics is not accidental, since the same methods of statistical inference are common to both.

9.3.1 Derivation of Maximum Entropy Electron Spectra

To employ the maximum entropy formalism to estimate the spectral flux of precipitating electrons, we need to express this flux in terms of a normalized continuous probability distribution. We define the single electron energy distribution, p(T), as the probability per keV of an electron having an energy in the range, dT, at energy T. Then, the spectral flux of electrons is,

$$s(T) = G\ p(T) \tag{9-11}$$

where G is the total flux of electrons at all energies (electrons/cm^2-sec). Bremsstrahlung flux measurements at n different energies, k(keV), provide n equations, derived from Equation 9-1.

$$f_k = G \int \phi(k,T)p(T)dT \quad \text{(n equations)} \quad . \tag{9-12}$$

In addition, we require the probability to be normalized,

$$1 = \int p(T)dT \quad . \tag{9-13}$$

We maximize the entropy of the single particle distribution, since we assume electrons are independent. The appropriate generalization of Equation 9-9 for continuous distributions is,[83]

$$H_1 = - \int p(T)\ln[p(T)/m(T)]dT \tag{9-14}$$

where m(T) is the density of states in energy for precipitating electrons.

Because of the presence of the total flux, G, an additional unknown, Equation 9-12 provides only n-1 constraints, not n constraints. This unknown can be eliminated by taking the ratio of the successive

equations, indicated by Equation 9-12, ordered by increasing values of observed photon energy, k. In this way, Equation 9-12 is re-cast as n-1 constraint equations,

$$0 = f_k \int \phi(k+1,T)p(T)dT - f_{k+1} \int \phi(k)p(T)dT \qquad (9\text{-}15)$$

where k and k+1 indicate successive energies at which bremsstrahlung fluxes are measured.

We now maximize the entropy given by Equation 9-14 subject to the normalization constraint of Equation 9-13 with Lagrange multiplier $-\alpha$ and the n-1 constraints given by Equation 9-15 each with a Lagrange multiplier $-\beta_k$, $k=1,\ldots,n-1$. There results the maximum entropy probability distribution

$$p(T) = m(T)\ \exp(-\alpha)\ \exp\{-\sum_{k=1}^{n-1} \beta_k[f_k\phi(k+1,T)-f_{k+1}\ \phi(k,T)]\}. \qquad (9\text{-}16)$$

The factor, $\exp(-\alpha)$, normalizes the probability distribution. Substitution of Equation 9-16 into Equation 9-14, with the requirement that Equation 9-15 be satisfied provides an expression for the entropy,

$$H_1 = \ln \int dT\ m(T)\ \exp\{-\sum_{k=1}^{n-1} \beta_k[f_k\phi(k+1,T)-f_{k+1}\ \phi(k,T)]\}\ . \qquad (9\text{-}17)$$

The values of β_k which produce an extremum of H_1 are the correct parameters to use in the distribution. It turns out in this case that H_1 is equal to α. Once the distribution p(T) is known, any one of the original constraints, given by Equation 9-12, can be used to determine the remaining unknown, G.

There remains only the need to calculate the density of states, m(T). The number of single particle electron states in which an electron has a direction within the solid angle, $d\Omega$, and magnitude of momentum within dp of p is,

$$m = 2\pi \sin\theta \, d\theta \, p^2 dp \, \Delta x \Delta y \Delta z / h^3$$

where $\Delta x \Delta y \Delta z$ is the volume of space available to the electron. We need the number of states available to an electron which contributes to the downward electron flux. All electrons within a distance $\Delta z = |V_z| \Delta t$ of the "top of the atmosphere" and with angles $\pi/2 < \theta < \pi$ contribute to the flux. For simplicity, consider non-relativistic electrons, so that $|V_z| = p \cos\theta/m$ and kinetic energy $T = p^2/2m$. The integrated number of single particle electron states which cross area $\Delta x \Delta y$ in time Δt in the kinetic energy interval dT at energy T is,

$$m(T) = (4\pi m/h^3) T \, dT \, \Delta x \Delta y \Delta t$$

where an additional factor of 2 is included for electron spin degeneracy. In fact, one does not need an exact expression of state density. Since both p(T) in Equation 9-16 and the normalizing factor which divides it both contain m(T), all the constants divide out. We need only know that m(T) is proportional to T in order to calculate the maximum entropy estimate of spectral electron flux.

9.3.2 Sample Calculation

To illustrate the foregoing ideas, we present a simple model calculation which may be done analytically, but which preserves the general features of the real situation. We assume a simple analytical form which roughly approximates the true kernel of bremsstrahlung production given in Figure 25,

$$\phi(k,T)[\text{keV}^{-1}] = 3.703 \times 10^{-4}\ (T-k)\ /\ k^{1.7} \qquad T > k$$
$$= 0 \qquad T < k \tag{9-17}$$

where T and k are respectively electron and photon energy in keV. We further assume an electron flux spectrum, s(T) = G p(T), given by the function,

$$p(T)[\text{keV}^{-1}] = N^{-1}\ (T - bT^2 + cT^3)\ \exp(-\gamma T) \tag{9-18}$$

with the normalization,

$$N^{-1} = 2.273 \times 10^{-4} \quad (\text{keV})^{-2}$$

and constants,

$$b = 5.8 \times 10^{-3} \quad (\text{keV})^{-1}$$
$$c = 10^{-5} \quad (\text{keV})^{-2}$$
$$\gamma = 10^{-2} \quad (\text{keV})^{-1}$$
$$G = 1.286 \times 10^{5} \quad \text{elec/cm}^2\text{-sec} \quad .$$

This spectral electron flux is plotted as the solid line in Figure 26, and designated s(T).

This spectral electron flux together with the bremsstrahlung kernel in Equation 9-17 can be used in Equation 9-1 to directly calculate the photon flux which would be produced at various energies. The results for two photon energies are:

Photon Energy, k (keV)	Flux (photons/cm^2-sec-keV)
50	10.0
200	0.49545

We now reverse the logical point of view and imagine that these two photon fluxes are measured quantities from which we infer, by maximum entropy methods, *the electron flux which produced them.* For analytical simplicity, photon flux measurements are considered at just two energies, although the more measurements, the better the electron flux can be determined. With two measurements, as here, only two parameters of the electron distribution can be established. These are the total electron flux, G', and a single Lagrange multiplier, β, of the distribution in Equation 9-16. The electron distribution, obtained by the method of the previous section, consists of three segments because the exponential contains zero, one, or two non-zero terms. (Remember $\phi = 0$, if $T < k$.) The deduced electron flux $s'(T) = G'p'(T)$ is shown as the dashed line in Figure 26, which may be directly compared with the original electron flux spectrum. Analytically, the deduced flux spectrum has the form,

$$s(T') = G'p'(T) = G'A^{-1}\, T \exp\{-\beta[f_{50}\, \phi(200,T) - f_{200}\, \phi(50,T)]\} \tag{9-19}$$

where the normalization is,

$$A^{-1} = 5.18 \times 10^{-6} \quad (\text{keV})^{-2}$$

and,

$$\beta = 3.4235 \times 10^{4} \quad \text{cm}^2\text{-sec-(keV)}^2/\text{photon}$$

$$G' = 7.28 \times 10^{4} \quad (\text{elec/cm}^2\text{-sec}) \quad .$$

The values of ϕ are given by Equation 9-17.

In this example, maximum entropy is used to infer an original electron spectrum from measurements of photon fluxes at only two energies. This is asking quite a bit. But Figure 26 shows that the results are

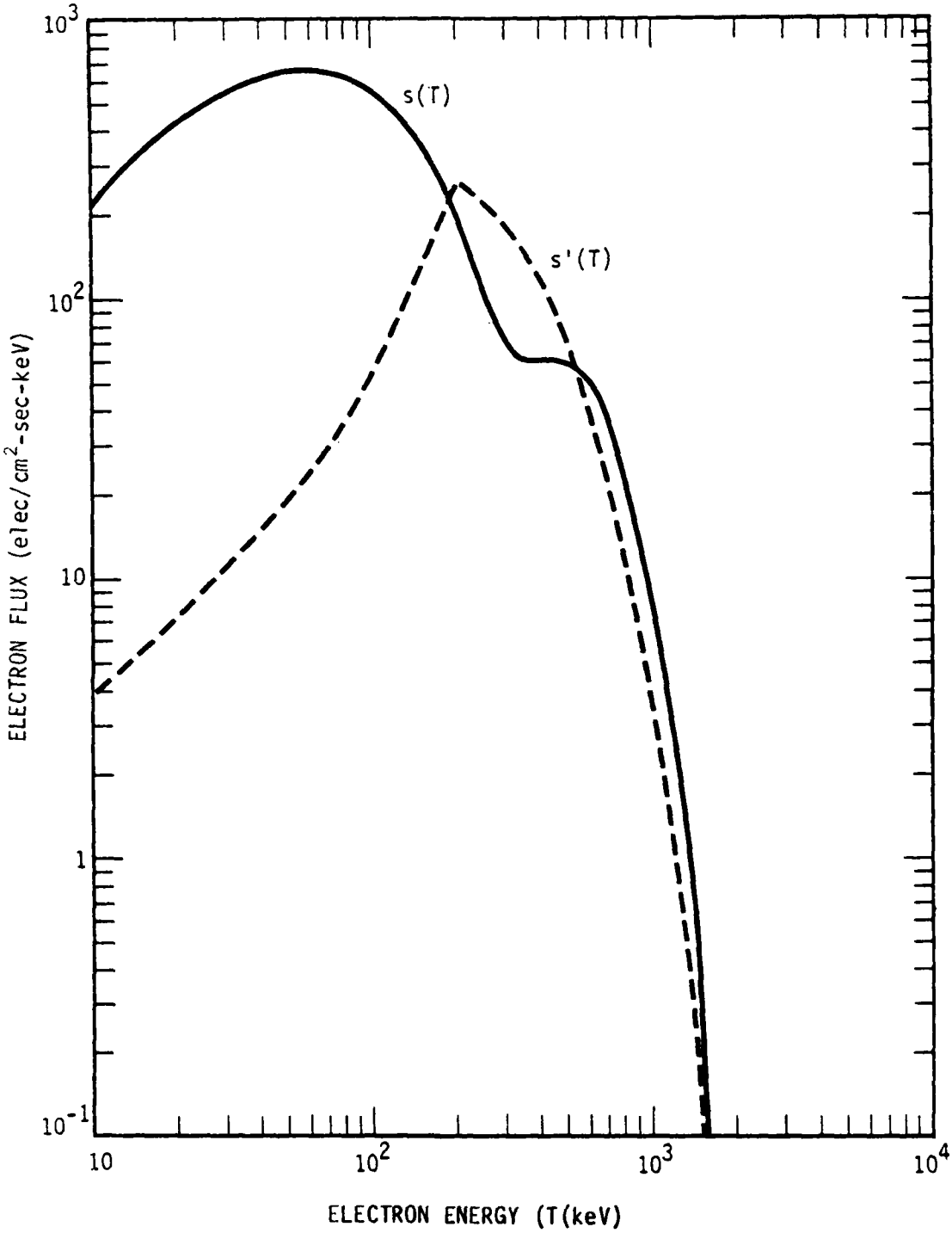

Figure 26. Comparison of test electron flux s(T), with electron flux s'(T) deduced by maximum entropy from two measurements of bremsstrahlung x-ray flux at 50 and 200 keV.

reasonable, especially at higher energies. The fact that the prediction is poorer at low energies is not surprising. Because the bremsstrahlung production kernel is zero when electron energy is less than x-ray energy, the data used in fact supply no information about the electron spectrum below 50 keV, and only one item of information about the electron spectrum between 50 and 200 keV. Only above 200 keV is the electron distribution sampled by both measurements of photon flux. Although this example used only two photon energies for analytical convenience, no difficulties are, in principle, encountered with more measurements, and, with more measurements, the inference becomes more accurate.

To implement the method requires more accurate knowledge of the production kernel, ϕ, especially at low photon energies (10 keV or less) and measurements of x-ray flux at all significant energies, including the very lowest.

A final comment can be made about the effect of errors in the measurement of x-ray fluxes. In terms of the formalism given, the effect of errors can be assessed directly, because the measured fluxes, f_k, enter directly into the probability distribution given by Equation 9-16. Consequently, the uncertainty of the electron spectrum attributable to measurement error can be directly determined by computing the effect of small changes in the f_k.

REFERENCES

1. Schmerling, E. R., and R. C. Langille (eds.). Special Issue on Topside Sounding and the Ionosphere, Proc. IEEE, 57, June 1969.

2. Daniels, F., ISIS II Spacecraft, CRC Report No. 1218, Communications Research Center, Dept. Communications, Canada, 1971.

3. Bibl, K., and B. W. Reinisch, "The Universal Digital Ionosonde," Radio Science, 13, May-June 1978.

4. Bibl, K., and B. W. Reinisch, Digisonde 128P-An Advanced Ionospheric Sounder--System Description and Manual, University of Lowell Center for Atmospheric Research, 1977.

5. Bibl, K., and B. W. Reinisch, Digisonde 128PS-For Ionospheric Dynamics and Three Dimensional Structure Studies--System Description and Manual, University of Lowell Center for Atmospheric Research, 1978.

6. Fulks, G. J., ISIS Topside Sounder Data Gathered on Kwajalein Atoll During the Summers of 1977 and 1978, DNA 5339F, October 1980.

7. Hagg, E. L., E. J. Hewens, and G. L. Nelms, "The Interpretation of Topside Sounder Ionograms," Proc. IEEE, 57, June 1969.

8. Jackson, J. E., "The Reduction of Topside Ionograms to Electron-Density Profiles," Proc. IEEE, June 1969.

9. Muldrew, D. B., "Radio Propagation Along Magnetic Field-Aligned Sheets of Ionization Observed by the Alouette Topside Sounder," J. Geophys. Res., 68, October 1963.

10. Muldrew, D. B., "Nonvertical Propagation and Delayed-Echo Generation Observed by the Topside Sounders," Proc. IEEE, June 1969.

11. McClure, J. P., W. B. Hanson, and J. H. Hoffman, "Plasma Bubbles and Irregularities in the Equatorial Ionosphere," J. Geophys. Res., 81, 1977.

12. Lockwood, G. K., and L. E. Petrie, "Low Latitude Field Aligned Ionization Observed by the Alouette Topside Sounder," Planet. Space Sci., 11, 1963.

13. Clavert, W., and C. W. Schmidt, "Spread-F Observations by the Alouette Topside Sounder Satellite," J. Geophys. Res., 69, 1964.

14. Blamont, J. E., M. L. Chanin, and G. Mégie, "Vertical Distribution and Temperature Profile of the Nighttime Atmospheric Sodium Layer Obtained by Laser Scattering," Ann. Geophys., 28, 1972.

15. Hake, R. D., Jr., D. E. Arnold, D. W. Jackson, W. E. Evans, B. P. Ficklin, and R. A. Long, "Dye-Laser Observations of the Nighttime Atomic Sodium Layer," J. Geophys. Res., 77, December 1972.

16. Kirchoff, V. W. J. H., and B. R. Clemesha, "Atmospheric Sodium Measurements at 23°S," J. Atmos. Terr. Phys., 35, 1973.

17. Mégie, G., F. Bos, J. E. Blamont, and M. L. Chanin, "Simultaneous Nighttime Lidar Measurements of Atmospheric Sodium and Potassium," Planet. and Space Sci., 26, January 1978.

18. Rowlett, J. R., C. S. Gardner, E. S. Richter, and C. F. Sechrist, Jr., "Lidar Observations of Wave-Like Structure in the Atmospheric Sodium Layer," Geophys. Res. Lett., 5, August 1978.

19. Hauchecorne, A., and M. L. Chanin, "Density and Temperature Profiles Obtained by Lidar Between 30 and 80 km," Geophys. Res. Lett., 7, 1980.

20. Jegou, J. P., M. L. Chanin, G. Mégie, and J. E. Blamont, "Lidar Measurements of Atmospheric Lithium," Submitted to Geophy. Res. Lett., 1980.

21. Chanin, M. L., and A. Hauchercorne, "Lidar Observations of Density Waves in the Stratosphere and Mesosphere," Submitted to J. Geophys. Res., 1980.

22. Greco, R. V., Atmospheric Lidar Multi-User Instrument System Definition Study, Executive Summary, NAS 1-15476, General Electric Space Division, 1978.

23. Carrigan, A. L., and R. A. Skrivanek, Aerospace Environment (Chart), Air Force Cambridge Research Laboratories (AFCRL), 1974.

24. Wiese, W. L., M. W. Smith, and B. M. Glennon, Atomic Transition Probabilities, Volume 1 Hydrogen Through Neon, NSRDS-NBS-4, National Bureau of Standards, 1966.

25. Allen, C. W., Astrophysical Quantities, Athlone Press, 1976.

26. Browell, E. V. (ed.), Shuttle Atmospheric Lidar Research Program, Final Report of Atmospheric Lidar Working Group, NASA SP-433, 1979.

27. Evans, J. V., "Theory and Practice of Ionospheric Study by Thomson Scatter Radar," Proc. IEEE, 57, April 1969.

28. Booker, H. G., "A Theory of Scattering by Non-Isotropic Irregularities with Application to Radar Reflections from the Aurora," J. Atmos. Terr. Phys., 8, 1956.

29. Thomson, J. J., Conduction of Electricity Through Gases, Cambridge University Press, 1906.

30. Gordon, W. E., "Incoherent Scattering of Radio Waves by Free Electrons with Appliations to Space Exploration by Radar," Proc. IRE, 46, 1958.

31. Bowles, K. L., "Observations of Vertical Incidence Scatter from the Ionosphere at 41 Mc/sec," Phys. Rev. Lett., 1, 1958.

32. Farley, D. T., J. P. Dougherty, and D. W. Barron, "A Theory of Incoherent Scattering of Radio Waves by a Plasma II Scattering in a Magnetic Field," Proc. Roy. Soc., A263, 1961.

33. Farley, D. T., et al., "Temperature and Composition of the Equatorial Ionosphere," J. Geophys. Res., 72, 1967.

34. Baron, M., R. Tsunoda, J. Petriceks, and H. Kunnes, Feasibility of an Incoherent-Scatter Radar Aboard the Space Shuttle, Stanford Research Institute, March 1976.

35. Davies, K., Ionospheric Radio Propagation, National Bureau of Standards Monograph 80, 1965.

36. Budden, K. G., Lectures on Magnetoionic Theory, Gordon and Breach, 1964.

37. Davies, K., R. B. Fritz and T. B. Gray, "Measurements of the Column Electron Contents of the Ionosphere and Plasmasphere," J. Geophys. Res., 81, 2825 (1976).

38. Millman, G. H., "A Simulator for Evaluating the Accuracy of Various Techniques for Electron Content Determination from Satellite Transmissions," in Effects of the Ionosphere on Space Systems and Communications, J. M. Goodman, editor, Naval Research Laboratory, 1975.

39. Potts, B. C., "Mean Ionospheric Scale Heights Deduced from Faraday Rotation Measurements," J. Geophys. Res., 70, 2651 (1965).

40. Titheridge, J. E., "Determination of Ionospheric Electron Content from the Faraday Rotation of Geostationary Satellite Signals," Planet. Space Sci., 20, 353 (1972).

41. Davies, K., R. F. Donnelly, R. N. Grubb, P.V.S. Rama Rao, R. G. Rastogi, M. R. Deshpande, H. Chandra, H. O. Vats and G. Sethia, "ATS-6 Satellite Radio Beacon Measurements at Ootacamund, India," Radio Sci., 14, 85 (1979).

42. Yeh, K. C., "Second Order Faraday Rotation Formulas," J. Geophys. Res., 65, 2548 (1960).

43. Garriott, O. K., "The Determination of Ionospheric Electron Content and Distribution from Satellite Observations, Part 1, Theory of the Analysis," J. Geophys. Res., 65, 1139 (1960).

44. Ross, W. J., "Second-Order Effects in High-Frequency Transionospheric Propagation," J. Geophys. Res., 70, 597 (1965).

45. Davies, K., R. B. Fritz, R. N. Grubb and J. E. Jones, "Some Early Results from the ATS-6 Radio Beacon Experiment," Radio Sci., 10, 785 (1975).

46. Sinno, K., and M. Kan, "Midlatitude Ionospheric Scintillations of VHF Radio Signals Associated with Peculiar Fluctuations of Faraday Rotation," J. Atmos. Terr. Phys., 40, 503 (1978).

47. Rees, M. H. and D. Luckey, "Auroral Electron Energy Derived from Ratio of Spectroscopic Emissions 1. Model Computations," J. Geophys. Res., 79, 5181 (1974).

48. Van Tassel, R. A., Airglow Calculations for Remote Sensing of Density," AFGL-TR-78-0115, Air Force Geophysics Laboratory, May 1978.

49. Isler, R. C. and W. G. Fastie, "An Observation of the Lyman-Birge-Hopefield System in an Aurora," J. Geophys. Res., 70, 2613 (1965).

50. Cartwright, D. C., W. R. Pendleton, Jr., and L. D. Weaver, "Auroral Emission of the N_2^+ Meinel Bands," J. Geophys. Res., 80, 651 (1975).

51. Hicks, G. T. and T. A. Chubb, "Equational Aurora/Airglow in the Far Ultraviolet," J. Geophys. Res., 75, 6233 (1970).

52. Peterson, V. L., T. E. Van Zandt and R. B. Norton, "F-Region Nightglow Emissions of Atomic Oxygen 1. Theory," J. Geophys. Res., 71, 2255 (1966).

53. Tinsley, B. A., A. B. Christensen, J. Bittencourt, H. Gouveia, P. D. Angreji and H. Takahashi, "Excitation of Oxygen Permitted Line Emissions in the Tropical Nightglow," J. Geophys. Res., 78, 1174 (1973).

54. CIRA 1972, Cospar International Reference Atmosphere 1972, Akademie-Verlag, 1972.

55. Defense Nuclear Agency Reaction Rate Handbook, Revision No. 8, Editors, M. H. Bortner and T. Baurer, DNA 1948H, April 1979.

56. Zipf, E. C., "A Laboratory Study of the Dissociative Recombination of Vibrationally Excited O_2^+ Ions," J. Geophys. Res., 85, 4232 (1980).

57. Kopp, J. P., J. E. Frederic, D. W. Rusch and G. A. Victor," Morning and Evening Behavior of the F Region Green Line Emission: Evidence Concerning Sources of $O(^1S)$," J. Geophys. Res., 82, 4715 (1977).

58. Coggen, L. L. and Smith, "Aeronomical Determination of the Effeciency of $O(^1D)$ Production by Dissociative Recombination of O_2^+", Planet. Space Sci., 25, 155 (1977).

59. Chandra, S., E. I. Reed, R. R. Meier, C. B. Opal and G. T. Hicks, "Remote Sensing of the Ionospheric F Layer by Use of OI 6300Å and OI 1356Å Observations," J. Geophys. Res., 80, 2327 (1975).

60. Tinsley, B. A. and J. A. Bittencourt, "Determination of F-Region Height and Peak Electron Density at Night Using Airglow Emissions from Atomic Oxygen," J. Geophys. Res., 80, 2333 (1975).

61. Olsen, R. E., J. R. Peterson, and J. Moseley, "Oxygen Ion-Ion Neutralization Reaction as Related to Tropical Ultraviolet Nightglow," J. Geophys. Res., 76, 2516 (1971).

62. Hayes, P. B., G. Carignan, B. C. Kennedy, G. G. Shepherd, and J. C. G. Walker, "The Visible-Airglow Experiment on Atmospheric Explorer," Radio Science, 8, 369 (1973).

63. Thomas, R. J. and T. M. Donahue, "Analysis of OGO-6 Observations of the OI 5577Å Tropical Nightglow," J. Geophys. Res., 77, 3557 (1972).

64. Donahue, T. M., "OGO-6 Observations of 5577Å," in Atmospheres of Earth and the Planets, B. M. McCormac, editor, D. Reidel Publishing Co., 1975.

65. Brinton, H., Private Communication, 1977.

66. Mizera, P. F., D. R. Croley, Jr., F. A Morse, and V. L. Vampola, "Electron Fluxes and Correlations with Quiet Time Auroral Arcs," J. Geophys. Res., 80, June 1975.

67. Imhof, W. L., G. H. Nakano, E. E. Gaines, and J. B. Reagan, "A Coordinated Two-Satellite Study of Energetic Electron Precipitation Events," J. Geophys. Res., 80, September 1975.

68. Imhof, W. L., G. H. Nakano, and J. B. Reagan, "Satellite Observations of X-rays Associated with Energetic Electron Precipitation Near the Trapping Boundary," J. Geophys. Res., 80, September 1975.

69. Mizera, P. F., J. G. Luhmann, W. A. Kolasinski, and J. B. Blake, "Correlated Observations of Auroral Arcs, Electrons, and X-rays from a DMSP Satellite," J. Geophys. Res., 83, December 1978.

70. Luhmann, J. G., H. R. Rugge, J. B. Blake, L. A. Christopher, "Low Latitude Atmospheric X-rays Observed by HEAO-1," Geophy. Res. Lett., 6, January 1979.

71. Jasperse, J. R., "Electron Distribution Function and Ion Concentrations in the Earth's Lower Ionosphere From Boltzman-Fokker-Planck Theory," Planet. Space Sci., 1977.

72. Jasperse, J. R., and D. J. Strickland, Approximate Analytic Solutions for the Primary Auroral Electron Flux and Related Quantities, Air Force Geophysics Laboratory, AFGL-TR-81-0069, March 1981.

73. Mizera, P. F., Private Communication, 1981.

74. Seltzer, S. M., and M. J. Berger, "Bremsstrahlung in the Atmosphere at Satellite Altitudes," J. Atmos. Terr. Phys., 36, p 1283, 1974.

75. Luhmann, J. G., and J. B. Blake, "Calculations of Soft Auroral Bremsstrahlung and K_α Line Emission at Satellite Altitude," J. Atmos. Terr. Phys, 39, p 913, 1977.

76. Luhmann, J. G., "Auroral Bremsstrahlung Spectra in the Atmosphere," J. Atmos. Terr. Phys., 39, p 595, 1977.

77. Westwater, E. R., and O. N. Strand, "Chapter 16, Inversion Techniques," in Remote Sensing of the Troposphere, V. E. Derr (ed.), Wave Propagation Laboratory ERL and EE Department, Univ. of Colorado, Boulder, Colorado, U.S. Government Printing Office, 1972.

78. Jaynes, E. T., "Information Theory and Statistical Mechanics," Physical Review, 106, p 620, 1957.

79. Tribus, Myron, Rational Descriptions, Decision, and Designs, Pergamon Press, New York, 1969.

80. Levine, R. D., and M. Tribus (eds), The Maximum Entropy Formalism, Maximum Entropy Formalism Conference, Massachusetts Institute of Technology, MIT Press, 1978.

81. Childers, Donald G., (ed), Modern Spectral Analysis, Institute of Electrical and Electronics Engineers Press, John Wiley & Sons, New York, 1978.

82. Gull, S. F., and G. H. Daniell, Nature, 272, p 686, 1978.

83. Jaynes, E. T., "Information Theory and Statistical Mechanics," Statistical Physics, Vol. 3, K. W. Ford (ed), Brandeis Summer Institute 1962, W. A. Benjamin, Inc., New York, 1963.